9-6-2011

# Evaluation of Cathode Materials for Low Temperature (500-700C) Solid Oxide Fuel Cells

Alexander M. Lassman
*University of Connecticut - Storrs*, alexander.lassman@uconn.edu

# Evaluation of Cathode Materials for Low Temperature (500-700°C) Solid Oxide Fuel Cells

Alex Lassman

B.S. Mechanical Engineering, Lafayette College, 2006

A Thesis

Submitted in Partial Fulfillment of the

Requirements for the Degree of

Master of Science

in Mechanical Engineering

at the

University of Connecticut

2011

APPROVAL PAGE

Master of Science Thesis

# Evaluation of Cathode Materials for Low Temperature (500-700°C) Solid Oxide Fuel Cells

Presented by

Alex Lassman, B.S.

Major Advisor _____
Prabhakar Singh

Associate Advisor _____
Ugur Pasaogullari

Associate Advisor _____
Gary L. McVay

Associate Advisor _____
Atul Verma

Associate Advisor _____
Leon Shaw

University of Connecticut

# Acknowledgements

Thanks to my mom and dad, my sister, and the rest of my family for all of your love and support. Thanks to Dr. Singh, Dr. Verma, and Dr. Smirnova for all that you've taught me. Thanks to Pete, B.J., Trisha, and my lab mates at C2E2 for all your help. Thanks to my friends and gracias to Mare.

# Table of Contents

# Abstract

This thesis presents an investigation into state of the art cathode materials for the operation of low temperature (500-700°C) solid oxide fuel cell cathodes. Our first study involved testing different LSCF-GDC (varying wt.%) compositions in order to determine the optimal loading of the secondary ion conducting phase. The LSCF-GDC 70-30 wt.% mixture was found to have the lowest ASR, almost 2x lower than single phase LSCF at 600°C. From there, BSCF powder was obtained from a commercial supplier and tested against our LSCF baseline. The BSCF was found to have a ~7x lower ASR than LSCF at 600°C (0.4 $\Omega cm^2$ vs. 2.95 $\Omega cm^2$ at 600°C). BSCF was identified as the target for our studies of the cathode reaction mechanism.

We synthesized BSCF using two different synthesis routes: glycine-nitrate combustion, and EDTA-citrate synthesis. The high temperature combustion of the glycine-nitrate process caused the formation of secondary carbonate phases, and so this synthesis route is not recommended for synthesizing BSCF. The lower-temperature EDTA-citrate route ultimately allowed for the synthesis of single phase, A-site deficient [A=0.97], $Ba_{0.5}Sr_{0.5}Co_{0.8}Fe_{0.2}O_3$ and $Ba_{0.45}Sr_{0.45}Sm_{0.10}Co_{0.8}Fe_{0.2}O_3$. The powders were found to develop a secondary surface phase after exposure to ambient air at room temperature for as little as 100h. This phase was attributed to surface A-site carbonate formation due to exposure to atmospheric $CO_2$.

Thermal expansion and thermogravimetric experiments demonstrated a significant change in both the TEC and weight loss in the BSCF powder after ~400°C, and this was attributed to the onset of oxygen vacancy formation. A similar change in

LSCF was observed after ~700°C, suggesting that LSCF experiences minimal vacancy creation in the 500-700°C range investigated here.

AC impedance spectroscopy was carried in a range of 500-700°C, and $PO_2$ of 1.0-0.01 atm, in order to further investigate the electrochemical processes occurring on the cathode. The impedance spectra were modeled using an equivalent circuit model, and three distinct processes were identified, at high, middle, and low frequencies. These processes were ultimately attributed to a charge transfer process, a surface exchange process, and a gas diffusion process. Using the calculated $PO_2$ and temperature dependencies, a model was proposed to explain the mechanism behind the oxygen reduction reaction on the BSCF cathode. It was found that below 600°C, the primary mechanism is partial reduction of the gaseous oxygen, possibly followed by surface diffusion. Above 600°C, the gaseous oxygen is completely reduced and incorporated into the bulk of the cathode, where it undergoes bulk diffusion to the cathode/electrolyte interface.

# List of Figures

## Chapter 1



## Chapter 2

**Chapter 3**

# List of Tables

## Chapter 1



## Chapter 2



## Chapter 3

# Chapter 1

# Literature Review

## 1.1 Background

*Research Objective*

Solid oxide fuel cells have the potential for high efficiency power generation, and are able to utilize hydrogen and/or existing hydrocarbon fuel sources, while producing less $NO_x$ and $SO_x$ pollution than combustion-based power plants[1]. SOFC operate at high temperatures, around 800°C, which presents a host of materials engineering challenges, and leads to high costs and performance tradeoffs. A reduction in operating temperatures, to 600°C or lower, offers the potential for improved stability of cell components, less thermal expansion and sealing mismatch, reduced balance of plant costs, and the potential to replace expensive ceramic interconnects with steel interconnects. The main obstacle to lowering SOFC operational temperatures is the poor performance of commonly used cathode materials at these lower temperatures. The goal of this thesis is to characterize the structure, properties, and electrochemical performance of low temperature (500-700°C) SOFC cathodes.

*Solid Oxide Fuel Cells*

Fuel cells are electrochemical devices which produce electrical power. There are three major components of a fuel cell: electrolyte, cathode, and anode. Figure 1.1 gives a schematic of fuel cell operation, including the various components.

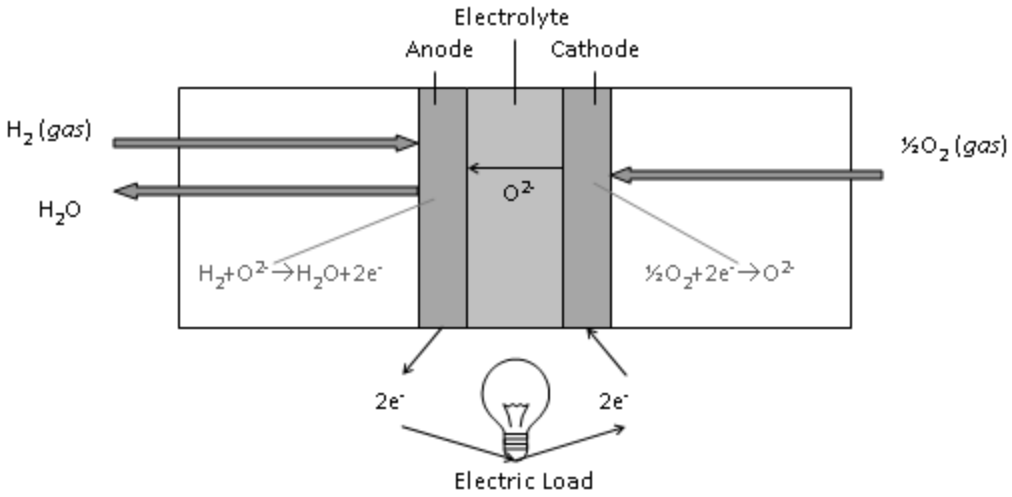


Figure 1.1 Schematic showing the operation of a solid oxide fuel cell with an oxygen ion conducing electrolyte.

The electrolyte is an ionic membrane separating the fuel and oxygen chambers. It must be gas tight to prevent the flow of gases from fuel side to air side, or vice versa. It also must conduct $O^{2-}$ ions, but without conducting electrons. Solid oxide fuel cells use a solid ceramic electrolyte which is capable of conducting negatively charged oxygen ions ($O^{2-}$) through the oxygen lattice of the material. During normal cell operation, oxygen anions are conducted across the electrolyte from the cathode (air side) to the anode (fuel side).

The cathode is the electrode on the oxygen (air) side of the electrolyte. In a solid oxide fuel cell, gaseous oxygen is reduced by the addition of two electrons, and the resultant ion is incorporated into vacancies in the material. The overall cathode reaction takes the following form, in Kroger-Vink notation.

$$(1)\quad ½O_2\,(gas) + 2e^{'} + V_O^{\cdot\cdot} \rightarrow O_O^{x}$$

## 1.2 Cathode Oxygen Reduction Mechanisms

The overall reaction occurring at the cathode of an SOFC involves the absorption of gaseous $O_2$ and ultimate incorporation into oxygen ion vacancies in the electrolyte. This reaction can be further broken down into several different steps, each representing a different step involved in the overall oxygen reduction reaction occurring on the cathode.

For SOFC cathodes with electronic conductivity but little ionic conductivity, such as LSM ($La_{1-x}Sr_xMnO_3$), ionic diffusion will be limited, and the reaction must take place at the triple phase boundary (TPB) between gas, cathode, and electrolyte. If the material has substantial ionic diffusion, however, the reaction can occur further away from the TPB, opening up more potential reaction sites. Materials which have high electronic and high ionic conductivity are called mixed ionic electronic conductors (MIEC). The properties of MIEC materials such as LSCF and BSCF are discussed later in Ch. 1.

The oxygen reduction reaction on a MIEC cathode consists of three general processes: surface oxygen exchange, diffusion through the cathode (bulk or surface), and electrochemical charge transfer at the cathode-electrolyte interface. The overall reaction can be broken down into three sub-reactions representing these three processes. This is shown in Figure 1.2. The component reactions are given below.

Surface Oxygen Exchange:

(2a) $\frac{1}{2}O_2$ (*gas*) + $2e^{'}$ + $V_O^{\cdot\cdot}$(*cathode*) → $O_O^x$ (*cathode*)

Diffusion:

(2b) $O_O^x$ (*cathode surface*)→ $O_O^x$ (*cathode/electrolyte interface*)

Electrochemical Charge Transfer:

(2c) $O_O^x$ (*cathode*) + $V_O^{\cdot\cdot}$(*electrolyte*) → $V_O^{\cdot\cdot}$(*cathode*) + $O_O^x$ (*electrolyte*)

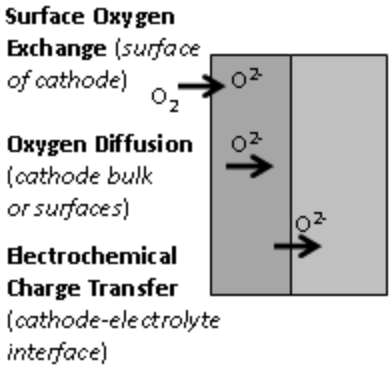


Figure 1.2. Schematic showing various steps in the cathode oxygen reduction reaction.

*Surface oxygen exchange*

At the surface of a MIEC material, gaseous oxygen, $O_2$, reacts with surface vacancies and electrons, and is ultimately incorporated into vacancies in the bulk of the cathode. This overall process can be further broken down into three component charge transfer steps: adsorption of gaseous $O_2$ onto an open surface vacancy, dissociation of $O_2$ by the occupation of a neighboring surface vacancy, and incorporation of the surface oxygen into the bulk

Adsorption:

$$(3a)\quad O_2\,(gas) + e' + V_O^{\cdot\cdot}(surface) \rightarrow (O_2)_O^{\cdot}\,(surface)$$

Dissociation:

$$(3b)\quad (O_2)_O^{x}\,(surface) + e' + V_O^{\cdot\cdot}(surface) \rightarrow 2O_O^{\cdot}\,(cathode)$$

Incorporation:

$$(3c)\quad (O_2)_O^{x}\,(cathode) + e' + V_O^{\cdot}(cathode) \rightarrow 2O_O^{x}\,(cathode)$$

Although this process is complex and not entirely understood, a thermodynamic model by Adler[2] suggests a few relevant parameters involved in improving surface

exchange kinetics. The thermodynamic driving force, $\Lambda$ for the surface exchange step in a metallic conducting MIEC cathode was found to be

$$(4)\quad \Lambda = RT \ln (P_{O2(gas)}\, x_v^2) - \Delta G^0_{rxn} + 24x_v/g_0$$

Where R, $\Delta G^0_{rxn}$, and $g_0$ are constants. This suggests that the reaction driving force increases with temperature, T, partial pressure of gaseous oxygen, $P_{O2(gas)}$, and the bulk vacancy mole fraction, $x_v$.

Generally, the oxygen surface kinetics of a material can be characterized using a lumped coefficient known as the oxygen surface exchange coefficient, k. Values of k have been published for LSM[3], LSC[4] and LSCF[5]. Values of k for some common cathode and electrolyte materials are given in Figure 1.3. From this figure it is evident that the Mn-based LSM has very poor surface exchange properties when compared to Co- and Fe- based LSC and LSCF, with a difference of almost 4 orders of magnitude. LSM cathodes will need to be used at higher temperatures than these other cathodes in order to obtain similar performance.

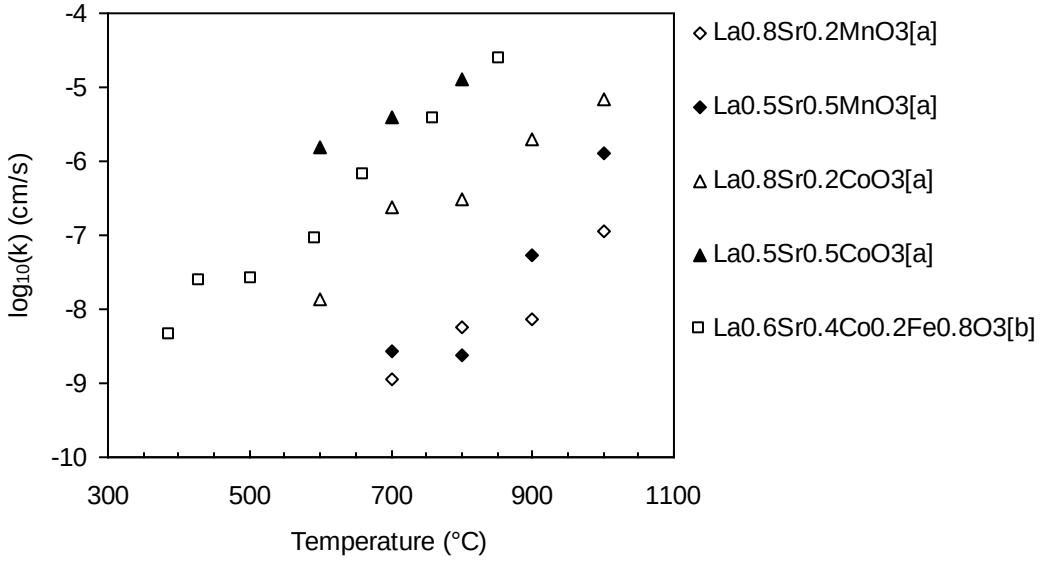

Figure 1.3. Values of oxygen surface exchange coefficient, k, for different cathode materials: $La_{0.8}Sr_{0.2}MnO_3$, $La_{0.8}Sr_{0.2}MnO_3$, $La_{0.8}Sr_{0.2}MnO_3$, $La_{0.8}Sr_{0.2}MnO_3$, and $La_{0.8}Sr_{0.2}Co_{0.2}Fe_{0.8}O_3$. Data taken from [a] Kilner et al.[6], [b] Benson et al.[7].

*Ionic Diffusion*

Diffusion in a MIEC cathode consists of the movement of oxygen ions from one vacant site to the next, by means of a hopping mechanism. The general property is known as ionic conductivity. The general expression for any type of conductivity, σ, in a material is given below[8].

$$(5)\ \sigma = ne_0\mu$$

Where n is the number of charge carriers, $e_0$ is the charge on the carrier, and μ is the mobility of the charge carriers. The charge on each oxygen ion, $e_0$, is constant. Since each vacancy has the potential to host a charge carrier, the number of charge carriers, n, will depend on the overall number of vacancies in the bulk of the material. The mobility of the oxygen ions follows the Arrhenius relationship

$$(6)\ \mu = \mu_0 \cdot \exp(-\frac{E_a}{R \cdot T})$$

Where $\mu_0$ is a constant, $E_a$ is the activation energy of the process, R is the gas constant, and T is the temperature.

The diffusion kinetics of the cathode can be characterized by a lumped coefficient known as the oxygen self-diffusion coefficient, D*. Values of D* for some common cathode and electrolyte materials are given in Figure 1.4. From this figure we can once again see a dramatic difference between LSM and the Co- and Fe- based LSC and LSCF, with a difference of about 6-7 orders of magnitude. This difference is even more than

that observed for the surface exchange coefficient, and it illustrates that LSM will have very limited ionic conductivity in SOFC operating conditions. This will ultimately affect the reaction mechanism, as reaction pathways involving ionic diffusion will not be energetically favorable. The reaction for LSM will be limited to the triple phase boundary, and the number of reaction sites will be related to the length of this boundary. For LSC and LSCF, ionic diffusion will be sufficient to allow the reaction to take place farther from the cathode-electrolyte interface. This will lead to a large number of reaction sites, spread out over the surface area of the cathode. Therefore, the network of reaction sites for LSM can be considered to be linear (1-D), while the network of reaction sites for LSC and LSCF can be considered to be a surface area (2-D).

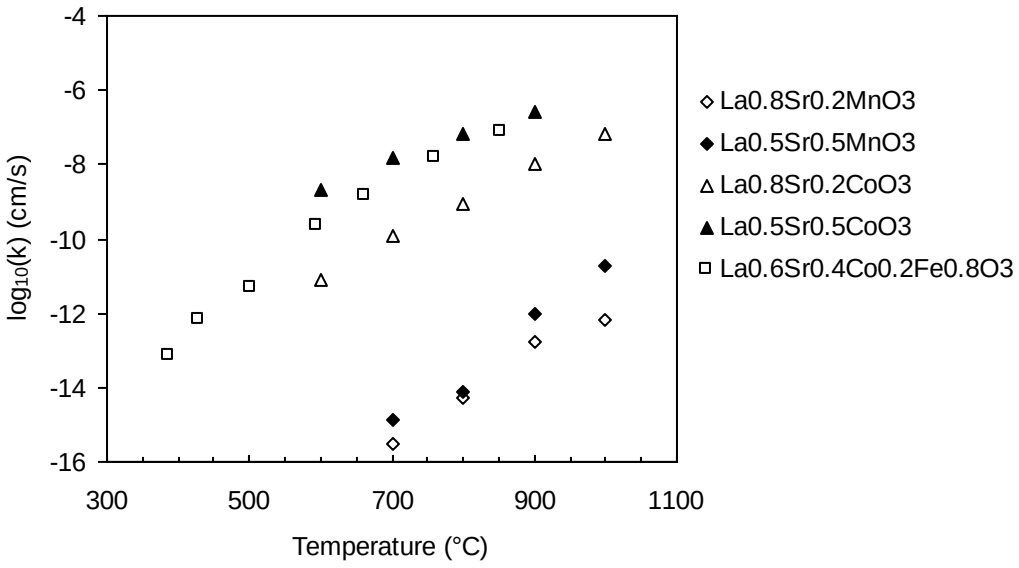


Figure 1.4. Values of oxygen self-diffusion coefficient, D*, for different cathode materials: $La_{0.8}Sr_{0.2}MnO_3$, $La_{0.8}Sr_{0.2}MnO_3$, $La_{0.8}Sr_{0.2}MnO_3$, $La_{0.8}Sr_{0.2}MnO_3$, and $La_{0.8}Sr_{0.2}Co_{0.2}Fe_{0.8}O_3$. Data taken from [a] Kilner et al.[9], [b] Benson et al.[10].

*Electrochemical Charge Transfer*

The electrochemical charge transfer step occurs at the solid-solid interface between the cathode and the electrolyte, and represents the transference of oxygen ions between the different phases. This step is an electrochemical reaction, for which current and potential are related by the Butler-Volmer equation.

$$(7)\ I = A \cdot i_0 \cdot \{\exp\left[\frac{(1-\alpha)\cdot n\cdot F}{R\cdot T}\left(E - E_{eq}\right)\right] - \exp[-\frac{\alpha\cdot n\cdot F}{R\cdot T}(E - E_{eq})]$$

At high overpotential, the Butler-Volmer equation reduces to the Tafel equation.

$$(8)\ I = n \cdot F \cdot k \cdot \exp[\frac{\alpha\cdot F\cdot \Delta V}{R\cdot T}]$$

The Tafel equation predicts a linear relationship between the overpotential, ΔV, and log(i), where the slope is referred to as a Tafel slope and can be calculated experimentally. If a system displays such Tafel behavior, it can be inferred that the rate limiting step may be related to an electrochemical reaction.

In order to understand the behavior of the cathode, a simple model can be developed in which the reaction mechanisms can be easily characterized. The next section explores the real world case of a porous MIEC cathode.

*Implications for Porous MIEC Cathode Systems*

In a porous MIEC cathode, there is the possibility of multiple reaction pathways. Bulk diffusion of oxygen ions will occur if the material is a mixed conductor, but in a porous electrode there may also be surface diffusion of oxygen ions towards the TPB. Oxygen adsorption will occur on the walls of the cathode pores, followed by charge transfer and incorporation of oxygen ions into the cathode bulk, or onto the cathode surface.

As discussed earlier in this chapter, LSM is a very poor ionic conductor, which leads to the reaction being confined to the triple phase boundary between cathode, electrolyte, and gas. For MIEC materials like LSC and LSCF, diffusion is more energetically favorable, and so the reaction can occur across the surface of the material. The location of the reaction site will determine the length of the diffusion pathway, and therefore how energetically favorable that reaction site is.

The length of the diffusion path increases with the distance from the cathode-electrolyte interface, so it is energetically favorable for an oxygen ion to adsorb onto the cathode wall as close to the electrolyte as possible. Of course this also depends upon the kinetics of the surface exchange reaction: if surface exchange kinetics are slow and diffusion is fast, potential reaction sites farther from the electrolyte may become more energetically favorable. A parameter can be derived in order to describe the depth of the cathode at which diffusion paths are still short enough to be energetically favorable, taking into account the surface exchange kinetics. This is called the characteristic diffusion length scale, $\delta$, and it's a direct function of the surface exchange coefficient, k, and the oxygen self-diffusion coefficient, D*.[11]

$$(9)\quad \delta = D^*/k$$

The reaction occurs on the surface inside the pores, so the number of reaction sites available increases with cathode thickness. More reaction sites mean better cathode performance. This suggests a situation contrary to natural intuition: porous cathode resistance will decrease with increasing layer thickness. There is a natural limit to this effect, since reaction sites added at a depth $y>3*\delta$ will have diffusion pathways too long to be energetically favorable, and further increases in thickness will only increase losses

due to electrical resistance. This suggests that an ideal porous cathode thickness should be at least 3*δ thick.

The characteristic diffusion length scale, δ, also has critical implications for the particle size, $d_p$, of the electrode[12]. For the case of a very large particle size, $\delta << d_p$, the reaction to be confined to areas of the particle close to the TPB. In the case of a very small particle size, $\delta >> d_p$, the oxygen ions will be able to diffuse easily throughout the entire bulk of the particle, and so the oxygen reduction reaction can occur across the entire surface of the particle. Particle size is therefore an important parameter in characterizing cathode performance.

### 1.3 Cathode Requirements

A cathode for an intermediate temperature solid oxide fuel cell must meet several basic requirements:

1. Electronic conductivity. A cathode must be able to efficiently conduct electrical charge (electronic conductivity of at least 100 S/cm is desirable). Since the current collector (whether porous metal paste or mesh) will not be physically located at the reaction site, a cathode must be able to transport electronic charge to the reaction site, via electrons or holes. Cathode materials which have high electronic resistance will produce a loss of cell voltage as a current is applied.

2. Ionic conductivity. The trend in IT-SOFC selection has been towards mixed ionic electronic conducting (MIEC) materials. A material with significant ionic conductivity (ionic conductivity of at least 0.01 S/cm is desirable)(put a range of conductivity acceptable) will be able to expand the number of available reaction sites beyond the triple

phase boundary of cathode, electrolyte, and gas. This will allow for better cathode performance.

3. Thermal expansion coefficient similar to the electrolyte. The cathode will be sintered in contact with the electrolyte (typically zirconia- or ceria-based). It therefore must have a similar thermal expansion coefficient (TEC) to the electrolyte used (10.5 ppm/K [13] for YSZ-8, and 11.8 ppm/K [14] for GDC-20) . This is more important as the sintering temperature increases. If the mismatch is too great, the cathode/electrolyte interface will experience large interfacial stresses, and will not be mechanically stable, leading to peeling and/or cracking. If other factors dictate selection of materials with different TEC, the mismatch can be ameliorated by using composites which contain cathode and electrolyte particles, or graded layers of such composites.

4. Chemical stability. The environment of the IT-SOFC cathode will be extremely oxidizing, with high temperatures (500-800°C), and air flowing over the cathode. The cathode material must be able to operate in this environment without phase segregation or severe morphological changes. Furthermore, the fabrication process may involve high temperature sintering of the cathode (1000-1300°C), and it is important that the material is stable during this process. Secondary phase growth, high temperature phase changes, and severe morphological changes may occur, and this may cause a reduction in the performance of the cathode.

5. Chemical Compatibility with other materials. The cathode must also must be resistant to the formation of non-conductive second phases when in contact with the electrolyte and interconnect materials at high temperatures. When metallic interconnects are used, they will form oxide scales at the collector-electrode interface, and these scales should be

nonreactive, and not contaminate the cathode[15]. Also, metal cations, such as chromium, may evaporate from the surface of a metallic interconnect. These metal ions can poison the cathode when the gas contacts the cathode.

### 1.4 Perovskite Structure

Perovskites are oxides with an $ABO_3$ formula, where A and B are cations of different size. A-site cations have a larger ionic radius, with a dodecahedral oxygen framework (coordination number 12). The bond between the A-site cations and the O anions is strongly ionic. The B-site cations are smaller, and are in an octahedral framework of oxygen (coordination number 6), with a bond which is strongly covalent. The ideal perovskite structure is cubic. If the A-site cation is considered to be the corner of a unit cell, the B-site sits in the body center position, and the oxygen ions are arranged in an FCC configuration. The perovskite structure is illustrated in Figure 1.5.

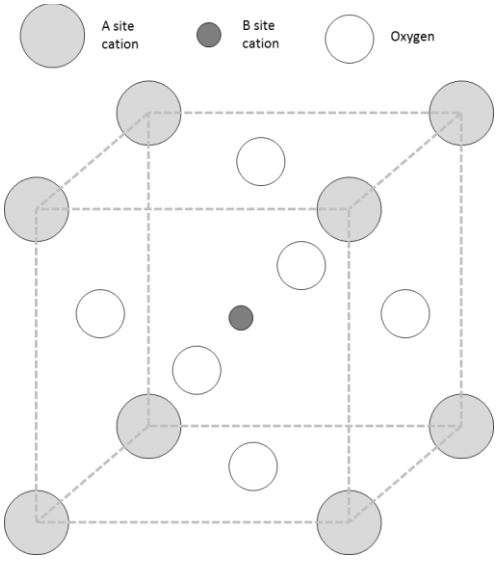


Figure 1.5. Graphical representation of perovskite structure.

The ideal cubic phase of the perovskite structure has tight spatial requirements for ionic radii, with the geometrical arrangement of the atoms in the perovskite structure characterized by the Goldschmidt tolerance factor, t[16].

$$(10)\quad t = \frac{r_A + r_O}{\sqrt{2}(r_B + r_O)}$$

In addition to the ideal cubic, the perovskite structure is known to exhibit orthorhombic or rhombohedral distortions, as well as the less common tetragonal, monoclinic, and triclinic symmetries[17,18,19]. The versatility of the perovskite structure allows different materials in this class to have technically important properties, such as ferroelectricity, piezoelectricity, magnetism, high-temperature superconductivity, electro-optic effects, and electro-catalysis[20].

In a solid oxide fuel cell cathode with a perovskite structure, the A site cation is often a rare earth metal from the lanthanide family (such as La, Sm), with a typical oxidation state of +3. The A-site may be doped with an alkaline earth metal (such as Sr, Ca), with a typical oxidation state of +2[21]. The B-site cation is typically a transition metal, such as cobalt, iron, or manganese (Co, Fe, Mn), which has the ability to easily transition between oxidation states. The following sections will address different perovskite materials in more detail.

## 1.5 Lanthanum Strontium Cobaltite

*Introduction*

Lanthanum cobaltite doped with strontium, $La_{1-x}Sr_xCoO_{3-\delta}$, was one of the first ceramic materials considered for use in solid oxide fuel cells[22]. Tedmon et al. at GE

Research Laboratories documented its use for solid oxide fuel cells in the 1969[23]. They concluded that it provided promising cell test results due to high electronic conductivity, but that the thermal expansion coefficient of $LaCoO_3$, around 28 ppm, was too high when compared with zirconia-based electrolytes (around 10 ppm). They also noted a serious problem of secondary phase formation when in contact with zirconia-based electrolytes.

*Structure*

The perovskite structure of $La_{1-x}Sr_xCoO_3$ consists of the $La^{3+}$ cation on the A-site, doped with $Sr^{2+}$, and $Co^{n+}$ as the B-site cation. Since cobalt is a transition metal, the oxidation state can change, and the cobalt atom may be $Co^{2+}$, $Co^{3+}$, or $Co^{4+}$, where the $Co^{3+}$ state is neutral with the lattice.

An XRD study[24] on $La_{1-x}Sr_xCoO_3$ compositions sintered at 900°C suggests two different phases at room temperature, which depend on the level of $Sr^{2+}$ doping, x. A rhombohedrally distorted perovskite (spacegroup $R\bar{3}c$) is observed when $x \leq 0.5$, and cubic perovskite (spacegroup Pm3m) is observed when $x > 0.5$. At room temperature, undoped $LaCoO_3$ is rhombohedral, with a lattice parameter a=0.3827, and a rhombohedral angle $\alpha = 90.75°$[25]. The unit cell volume increases with temperature, increasing the lattice parameter, and causing the rhombohedral angle to decrease[26,27], until the material changes from rhombohedral to cubic, when $\alpha = 90°$. As the level of $Sr^{2+}$ doping, x, in $La_{1-x}Sr_xCoO_3$ increases, a similar effect occurs, with $\alpha$ decreasing with increasing x. This explains the transition from rhombohedral to cubic perovskite structure around $x \sim 0.5$.

*Oxygen Nonstoichiometry*

$La_{1-x}Sr_xCoO_3$ will be oxygen deficient, and will become more deficient at lower $PO_2$. As $La^{3+}$ sites are doped with $Sr^{2+}$, the valence of a nearby B-site $Co^{3+}$ must change its valence state in order to maintain charge neutrality[28].

$$(11)\quad 2Sr'_{La} + 2Co^{x}_{Co} \rightarrow 2Sr^{x}_{La} + 2Co^{\cdot}_{Co}$$

Oxygen vacancies will then be created as the Co changes back its valence state as the material lattice expands at higher temperatures.

$$(12)\quad 2Co^{\cdot}_{Co} + O^{x}_{O} \rightarrow 2Co^{x}_{Co} + \tfrac{1}{2}O_2(gas) + V^{\cdot\cdot}_{O}$$

Vacancy concentration will increase with temperature, as the cobalt valence change becomes more energetically favorable. Vacancy creation also must come to equilibrium with the surrounding atmosphere. The overall effect is that the material will have more oxygen vacancies at higher temperatures and lower $PO_2$. Oxygen nonstoichiometry for $La_{0.3}Sr_{0.7}CoO_{3-\delta}$ is given as a function of $PO_2$ in Figure 1.6.

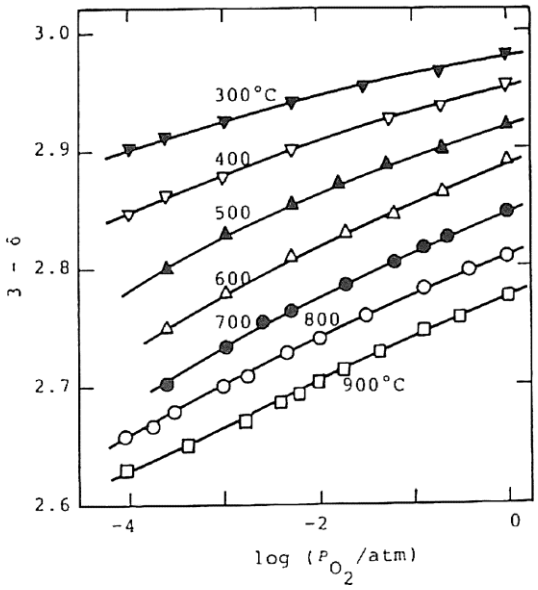


Figure 1.6. Oxygen nonstoichiometry vs. $PO_2$ for $La_{0.3}Sr_{0.7}CoO_3$[29].

*Electrical conductivity*

$La_{1-x}Sr_xCoO_3$, is known to have high electronic conductivity, (>1000 S/cm)[30]. Undoped $LaCoO_3$ is a p-type semiconductor at temperatures below 800°C, at which point it undergoes a semiconducting-metallic transition[31]. It is believed that the transition from metallic to semi-conducting behavior for $LaCoO_3$ is related to the rhombohedral angle, α, in the perovskite structure[32]. As mentioned previously, this angle will decrease with temperature and $Sr^{2+}$ doping, x. The material changes from semiconductor to metallic at $x \geq 0.3$, at which point the material displays metallic conductivity throughout the temperature range.

The metallic behavior has been explained by an itinerant electron model[33], and is believed to be due to the existence of an electron band gap in the Co-O-Co bond[34]. The metallic band gap behavior leads to the reported high electronic conductivity.

*Ionic Conductivity*

Ionic conductivity data for $La_{1-x}Sr_xCoO_{3-\delta}$ at 800°C is given in Table 1.1. LSC has a high ionic conductivity for $O^{2-}$, which allows the reduction reaction to take place in sites further from the cathode/electrolyte interface. This is contrast to LSM, in which the low ionic conductivity means that the reaction occurs at or near the TPB.

| Composition | Ionic Conductivity, $\sigma_O$ (S/cm) |
|---|---|
| $La_{0.6}Sr_{0.4}CoO_{3-\delta}$ | 0.22 |
| $La_{0.5}Sr_{0.5}CoO_{3-\delta}$ | 0.093 |
| $La_{0.3}Sr_{0.7}CoO_{3-\delta}$ | 0.76 |

Table 1.1. Ionic conductivity of $La_{1-x}Sr_xCoO_{3-\delta}$ at 800°C. Data for $La_{0.6}Sr_{0.4}CoO_{3-\delta}$ from Teraoka et al. [35], data for $La_{0.5}Sr_{0.5}CoO_{3-\delta}$, $La_{0.3}Sr_{0.7}CoO_{3-\delta}$ from Ullman et at al. [36]

*Reaction Mechanism*

Due to the high ionic conductivity in LSC, it has been speculated that the $O_2$ reduction reaction pathway consists of surface chemical exchange followed by bulk diffusion[37]. This is in contrast to LSM, where bulk diffusion is negligible, and the reaction must occur at or near the triple phase boundary. As mentioned earlier, an MIEC material will allow the reaction to occur at sites away from the cathode/electrolyte interface, with the distance characterized by the parameter of characteristic length, δ. The characteristic length of the LSC system has been modeled experimentally to be up to 15 μm[38]. Since a normal cathode thickness for an anode-supported SOFC is around 30 μm, this suggests that most of the cathode is electrochemically active.

It has been reported by Wang et al.[39] that the chemical diffusivity of oxygen has an activation energy of 133 kJ/mol, while the surface exchange coefficient has an activation energy of 67 kJ/mol. Figure 1.7 shows the surface exchange coefficient, and oxygen diffusion coefficient for $La_{0.5}Sr_{0.5}CoO_{3-\delta}$.

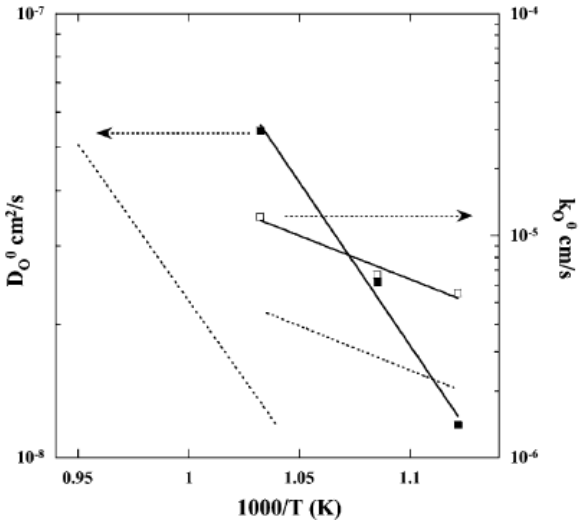


Figure 1.7. Surface exchange coefficient, $k_O^0$, and oxygen diffusion coefficient, $D_O^0$ for $La_{0.5}Sr_{0.5}CoO_{3-\delta}$ in $O_2$. Dotted line from De Souza, Kilner[40]; solid line from Wang et al.[41]

Surface oxygen exchange processes or oxygen diffusion may be rate-limiting, depending on the temperature. Higher reported activation energies for oxygen bulk diffusion suggest that bulk diffusion is less favorable than surface exchange at lower temperatures. Therefore bulk diffusion is more likely to be the rate limiting process under 400-600°C SOFC operation.

*Chemical/Mechanical Compatibility*

The thermal expansion coefficient of undoped $LaCoO_3$ was found to be 22-24 ppm/K[42],[43] and the TEC will generally increase with increasing $Sr^{2+}$ doping, as seen in Table 1.2. This suggests a substantial TEC mismatch with YSZ and GDC (10.5 ppm/K [44] for YSZ-8, and 11.8 ppm/K [45] for GDC-20).

| | TEC (ppm/K) |
|---|---|
| $La_{0.6}Sr_{0.4}CoO_{3-\delta}$ | 20.5 |
| $La_{0.5}Sr_{0.5}CoO_{3-\delta}$ | 22.3 |
| $La_{0.3}Sr_{0.7}CoO_{3-\delta}$ | 25.0 |

Table 1.2. TEC data for $La_{1-x}Sr_xCoO_{3-\delta}$ [46].

Simner et al. investigated a 50-50 mixture of $La_{0.6}Sr_{0.4}CoO_{3-\delta}$ and 8-YSZ, and found that they will react to form $La_2Zr_2O_7$ and $SrZrO_3$ after 2h at 1050°C[47], possibly as a result of the diffusion of cobalt into YSZ causing a change in the A/B ratio of the perovskite. This suggests that the use of LSC on YSZ electrolytes may not be appropriate. When LSC is used, it should be synthesized to be A-site deficient, in order to suppress zirconate formation. No data has been reported on detrimental reactions between LSC and GDC.

## 1.6 Lanthanum Strontium Ferrite

*Introduction*

Lanthanum ferrite doped with strontium, $La_{1-x}Sr_xFeO_{3-\delta}$ (LSF), has also been investigated widely for use as a cathode in SOFC. Similar to $La_{1-x}Sr_xCoO_{3-\delta}$, it demonstrates mixed ionic electronic conductivity at elevated temperatures, and has good electrocatalytic properties for oxygen reduction. While the electronic and ionic conductivity of LSF is not as high as LSCo, the TEC of LSF is more closely matched with commonly used cathode materials, such as YSZ and GDC.

*Structure*

The perovskite structure of $La_{1-x}Sr_xFeO_3$ consists of the $La^{3+}$ cation on the A-site, doped with $Sr^{2+}$, and the B-site cation $Fe^{n+}$. Since iron is a transition metal, the oxidation state can change, and the ion may be $Fe^{2+}$, $Fe^{3+}$, or $Fe^{4+}$, where the $Fe^{3+}$ state is neutral with the lattice. This behavior is responsible for the electronic conductivity in the material. The localized differentiation of iron oxidation state can be expressed as,

$$(13)\quad 2Fe^{x}_{Fe} \rightarrow Fe'_{Fe} + Fe^{\cdot}_{Fe}$$

An XRD study[48] on $La_{1-x}Sr_xFeO_{3-\delta}$ compositions sintered at 1300°C suggest that at room temperature there will be three distinct phases, depending on the level of $Sr^{2+}$ doping, x. An orthorhombic perovskite (spacegroup Pbnm) is observed when $x \leq 0.2$, a rhombohedral perovskite (spacegroup $R\bar{3}c$) is observed when $0.4 \leq x \leq 0.7$, and a cubic perovskite (spacegroup $Pm\bar{3}m$) is observed when $0.8 \leq x \leq 1.0$. At room temperature,

undoped $LaFeO_3$ is orthorhombic, with lattice parameters a=0.5570, b=0.7861, and c=0.5560 (all in nm)[49].

*Oxygen Nonstoichiometry*

$La_{1-x}Sr_xFeO_{3-\delta}$ shows oxygen deficiency, which comes about according to the same mechanisms as LSCo. As $La^{3+}$ sites are doped with $Sr^{2+}$, the valence of $Fe^{3+}$ will change to $Fe^{4+}$ in order to maintain charge neutrality.

$$(14)\quad 2Sr'_{La} + 2Fe^{x}_{Fe} \rightarrow 2Sr^{x}_{La} + 2Fe^{\cdot}_{Fe}$$

Oxygen vacancies will be created as the Fe cations change valence state as the lattice expands at higher temperatures.

$$(15)\quad 2Fe^{\cdot}_{Fe} + O^{x}_{O} \rightarrow 2Fe^{x}_{Fe} + \tfrac{1}{2}O_2(gas) + V^{\cdot\cdot}_{O}$$

The main difference in vacancy creation between LSF and LSCo is the generation of oxygen vacancies due the valence change associated with the generation of the $Fe^{2+}$ state. $Co^{2+}$ will be created at $PO_2<10^{-2}$ atm, whereas the $Fe^{2+}$ ion concentration will be negligible until $PO_2<10^{-5}$ atm[50]. This causes the nonstoichiometry of LSF to demonstrate a clear plateau in the middle $PO_2$ range. There will be three distinct regions of nonstoichiometry: a high $PO_2$ region where vacancies are created by $Fe^{4+}$ (created by $Sr^{2+}$ doping) changes to $Fe^{3+}$, a middle $PO_2$ plateau at $\delta \sim x/2$, where few vacancies are created, and a low $PO_2$ region where vacancies are again created as $Fe^{3+}$ changes to $Fe^{2+}$. Oxygen nonstoichiometry in LSF as a function of $PO_2$ is shown in Figure 1.8.

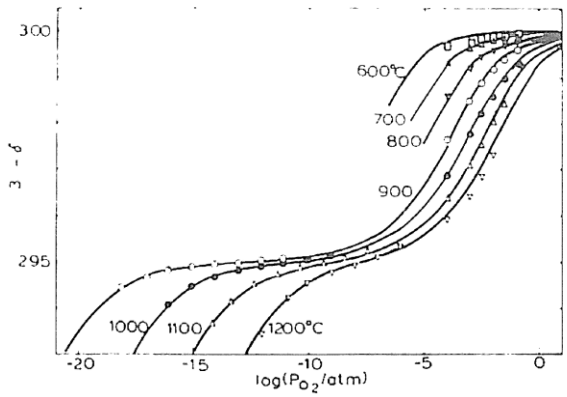


Figure 1.8. Oxygen nonstoichiometry as a function of $PO_2$ for $La_{0.9}Sr_{0.1}FeO_{3-\delta}$ [51].

*Electrical Conductivity*

$La_{1-x}Sr_xFeO_{3-\delta}$ shows high electronic conductivity (can be >100 S/cm), although not as high as LSC[52]. The electronic charge transport mechanism in LSF is the transport of holes or electrons by changes in valence of neighboring Fe ions[5354], and so it can be considered to have semiconducting (p-type) conductivity.

*Ionic Conductivity*

Ionic conductivity for $La_{0.6}Sr_{0.4}FeO_{3-\delta}$ at 800°C was found to be 0.0056 S/cm[55]. The ionic conductivity is higher than LSM, but lower than LSC, which suggest that bulk diffusion in LSF will not be as energetically favorable as for LSC-based cathodes.

*Rate Limiting Mechanism*

Work on $La_{0.5}Sr_{0.5}FeO_3$ has confirmed that the rate limiting step involves an oxygen atom, as opposed to molecular oxygen[56], suggesting that the process is controlled by surface exchange and diffusion. This is similar to the case for LSC. The study also

measured the surface exchange coefficient, $k_{chem}$, and the chemical diffusivity, $D_{chem}$; these results are shown in Figure 1.9. The activation energy for $k_{chem}$ was found to be 90 kJ/mol, and the activation energy for $D_{chem}$ was found to be119 kJ/mol. Similar to LSC, this suggests that diffusion will likely be rate-limiting for lower temperature SOFC operation.

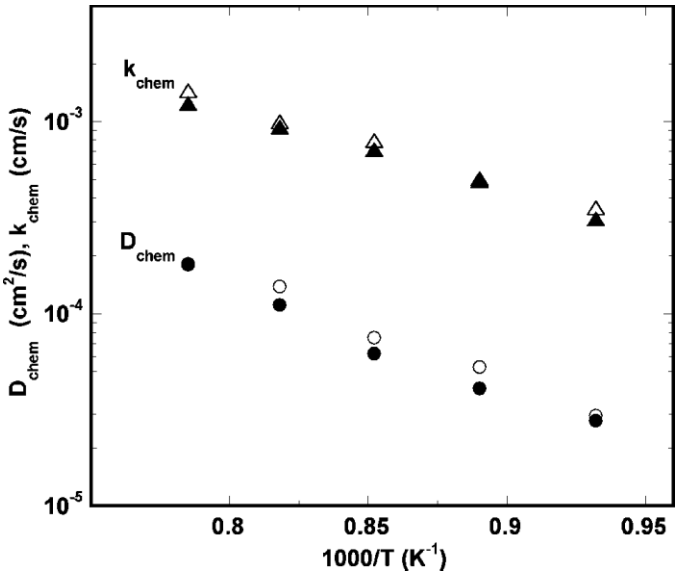


Figure 1.9. Surface exchange coefficient, $k_{chem}$, and chemical diffusivity, $D_{chem}$ for $La_{0.5}Sr_{0.5}FeO_3$[57].

*Chemical/Mechanical Compatibility*

Thermal expansion coefficient data for $La_{1-x}Sr_xFeO_{3-\delta}$ are shown in Table 1.3.

| | TEC (ppm/K) |
|---|---|
| $La_{0.7}Sr_{0.3}FeO_{3-\delta}$ | 14.0 ± 0.2 (room-600°C) |
| $La_{0.6}Sr_{0.4}FeO_{3-\delta}$ | 13.4 ± 0.4 (room-600°C) |
| $La_{0.5}Sr_{0.5}FeO_{3-\delta}$ | 14.0 ± 0.4 (room-500°C) |

Table 1.3. TEC data for $La_{1-x}Sr_xFeO_{3-\delta}$[58].

The TEC for LSF is closely matched to that of YSZ and GDC. Further, under sintering conditions, LSF and YSZ will not react as easily as LSC and YSZ to form to form $La_2Zr_2O_7$ and $SrZrO_3$. Simner et al. found no additional phase formation in a 50-50 mixture of $La_{0.6}Sr_{0.4}FeO_{3-\delta}$ and 8-YSZ after 2h at temperatures up to 1400°C[59]. This suggests that LSF is more stable in contact with YSZ than LSC. No data has been reported on detrimental reactions between LSF and GDC.

## 1.7 Barium Strontium Cobalt Ferrite

*Introduction*

LSC and LSF are both perovskites with mixed ionic and electronic conductivity, and utilize the same reaction pathways. The ionic and electronic conductivity of LSC is higher than LSF, but LSF is more chemically/mechanically compatible with electrolyte materials such as YSZ and GDC. In order to take advantage of both properties, researchers began to use both Co and Fe on the B-site, to produce $La_{1-x}Sr_xCo_{1-y}Fe_yO_{3-\delta}$ (LSCF). The double doping of LSCF (A- and B-site) allows researchers to optimize the composition, by achieving a compromise of certain desirable properties. LSCF has become one of the most studied cathodes for use in IT-SOFC, but ultimately it is a combination of LSC and LSF, and therefore its performance will not be able to exceed the limits of these materials. This is a problem at lower temperatures. Area specific resistance of LSCF at 600°C has been reported to be 1.2-4.0 $\Omega cm^2$ [60,61,62]. This falls far short of the generally accepted target of ~0.15 $\Omega cm^2$ set by Steele[63], leading to a push to modify the LSCF structure in order to obtain better performance at lower temperatures.

Based on the previous discussion of LSM, LSC, and LSF, two important conclusions can be drawn: (1) cathode performance is closely related to oxygen vacancy concentration, and (2) there is a positive correlation between aliovalent doping ($Sr^{2+}$ content) and oxygen vacancy concentration. This suggests that the electrochemical performance of LSCF could be improved by minimizing the amount of the stoichiometric cation ($La^{+3}$), and maximizing the amount of the aliovalent cation ($Sr^{+2}$). In fact, a study of the oxygen permeation characteristics of the $La_{1-x}Sr_xCo_{1-y}Fe_yO_{3-\delta}$ series[64] revealed that $SrCo_{0.8}Fe_{0.2}O_{3-\delta}$ displays the highest oxygen permeation rate.

While the results for the $SrCo_{0.8}Fe_{0.2}O_{3-\delta}$ composition were promising, subsequent studies suggested that the mechanical and phase stability of this composition was poor, which was attributed to the $Sr^{2+}$ cation being too small to allow for the cubic perovskite phase [65],[66],[67]. In order to stabilize the cubic phase, Shao et al. proposed partial substitution of the $Sr^{2+}$ cation with the larger $Ba^{2+}$ cation, and investigated oxygen permeation and phase stability of the $Ba_{1-x}Sr_xCo_{0.8}Fe_{0.2}O_{3-\delta}$ series[68],[69],[70],[71]. It was concluded that the $Ba_{0.5}Sr_{0.5}Co_{0.8}Fe_{0.2}O_{3-\delta}$ compound was the most promising, with high oxygen vacancy concentration, and better stability than $SrCo_{0.8}Fe_{0.2}O_{3-\delta}$.

Initially the work on BSCF was focused on its use as an oxygen permeation membrane, but it was soon tested for use as an IT-SOFC cathode. In a landmark paper[72], BSCF was shown to have low area specific resistance (0.055-0.071 Ωcm2 at 600 °C, and 0.51-0.60 Ωcm2 at 500 °C). A cell was prepared using a 700 μm thick Ni-SDC anode, 20 μm thick SDC cathode, and a 10-20 μm thick BSCF cathode, which demonstrated excellent performance characteristics (1010 mW/cm$^2$ at 600 °C, and 402 mW/cm$^2$ at 500

°C). This has sparked great interest in the use of BSCF as an IT-SOFC cathode. A recent review by Zhou[73] outlines some of this research.

*Structure*

A comparison of $Ba_{0.5}Sr_{0.5}Co_{0.8}Fe_{0.2}O_{3-\delta}$ and $SrCo_{0.8}Fe_{0.2}O_{3-\delta}$ structure and its implications on properties was completed by McIntosh et al[74]. As mentioned in the previous sections, both LSC and LSF will become cubic at higher $Sr^{2+}$ doping. BSCF and SCF will also display cubic behavior in air. In low $PO_2$, SCF will undergo a phase transition. At temperatures below 800°C under low $PO_2$, the oxygen vacancies will become ordered, and the structure will display an orthorhombic symmetry associated with the brownmillerite structure $Sr_2Co_{1.6}Fe_{1.4}O_5$. Above 800°C a cubic phase is again formed, with disordered vacancies. This phase change may cause problems with mechanical stability of the material, and additionally, the ordered oxygen vacancy structure of the brownmillerite is not as desirable for facilitation of oxygen mobility, which depends on randomly distributed vacancies. Adding $Ba^{2+}$ ions of a different size disrupts the periodicity of the SCF structure, and so the ordered brownmillerite structures can no longer form. This effect leads to the increased stability of cubic BSCF.

Chen et al. conducted an XRD study on the series $Ba_{0.5}Sr_{0.5}Co_{1-y}Fe_yO_{3-\delta}$[75]. It was found that for $0.2 \leq y \leq 1.0$, a vacancy-disordered cubic perovskite of space group Pm3m was formed. For $Ba_{0.5}Sr_{0.5}CoO_{3-\delta}$ (y=0), a vacancy-ordered 2-H type hexagonal perovskite was formed. This suggests that the addition of 20mol% Fe on the B-site is necessary to maintain the desired cubic structure.

*Oxygen Nonstoichiometry*

As mentioned previously, the B site metal will undergo a valence state change ($B^{3+}$ to $B^{4+}$) to compensate for the $Sr^{2+}$ cation sitting on a lattice site normally occupied by an $A^{3+}$ cation. This reaction is represented by the following

$$(16)\quad 2Sr'_A + 2B^x_B \rightarrow 2Sr^x_A + 2B^{\cdot}_B$$

Oxygen vacancies will be created as the B site cations change valence state as the lattice expands at higher temperatures.

$$(17)\quad 2B^{\cdot}_B + O^x_O \rightarrow 2B^x_B + \tfrac{1}{2}O_2(gas) + V^{\cdot\cdot}_O$$

The addition of the larger $Ba^{2+}$ ions will expand the lattice, essentially allowing more space for the larger $B^{3+}$ ion, even at room temperature. Therefore the BSCF will have very high oxygen vacancy concentration at low temperatures, as seen in Figure 1.10.

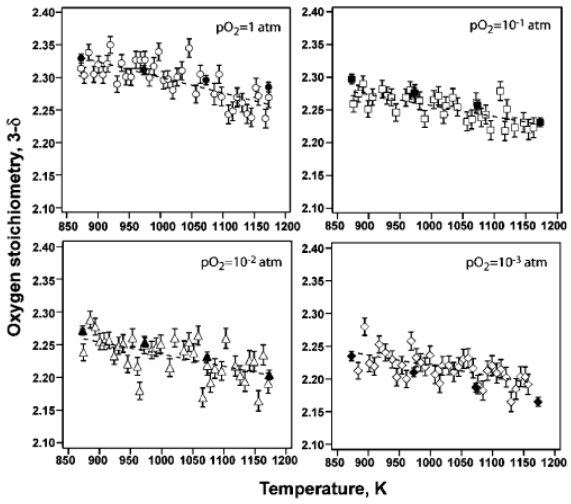


Figure 1.10. Oxygen stoichiometry vs. temperature for $Ba_{0.5}Sr_{0.5}Co_{0.8}Fe_{0.2}O_{3-\delta}$ [76].

*Electrical Conductivity*

The maximum electrical conductivity for $Ba_{0.5}Sr_{0.5}Co_{0.8}Fe_{0.2}O_{3-\delta}$ was found to be ~40 S/cm at 450°C[77], lower than LSC and similar to LSF.

*Ionic Conductivity*

The ionic conductivity of $Ba_{0.5}Sr_{0.5}Co_{0.8}Fe_{0.2}O_{3-\delta}$ was estimated to be 0.006 S/cm at 600°C, and 0.018 S/cm at 700°C[78]. It should be noted that the conductivity for LSF at 800°C (0.0056 S/cm) is similar to that reported for BSCF at only 600°C, suggesting that this material is extremely well suited for use as a cathode for lower temperature SOFC.

*Reaction Mechanism*

The high ionic conductivity of BSCF suggests that the reaction proceeds via the surface exchange and bulk diffusion pathway., with high D and k values reported, as seen in Figure 1.11 An activation energy of 86 kJ/mol was reported for diffusion, and an activation energy of 64 kJ/mol was reported for the surface exchange coefficient[79].. Much like LSC and LSF, this suggests that the rate limiting mechanism at lower temperatures will be the surface exchange process.

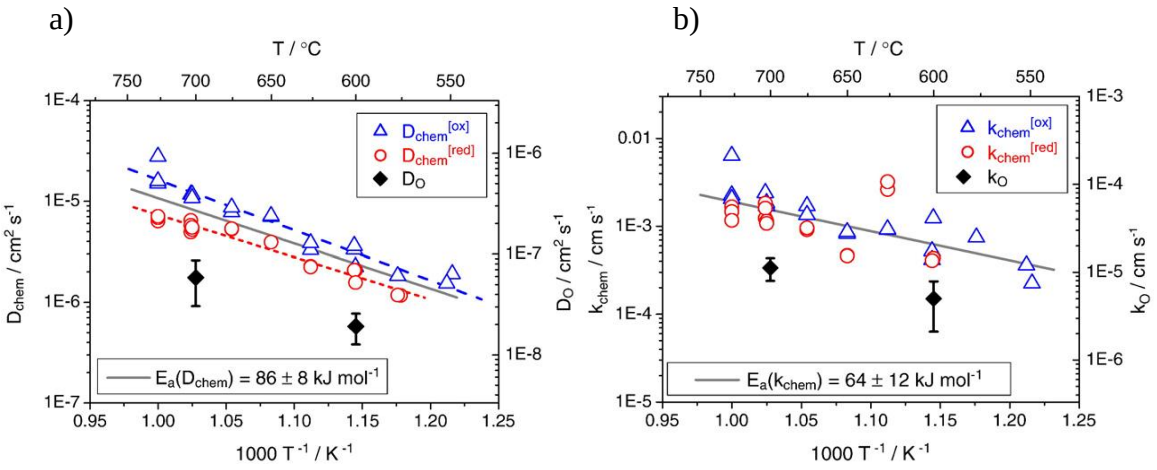


Figure 1.11. a) Oxygen diffusion coefficient and b) surface exchange coefficient for $Ba_{0.5}Sr_{0.5}Co_{0.8}Fe_{0.2}O_{3-\delta}$[80].

*Mechanical/Chemical Compatibility*

The thermal expansion behavior of BSCF shows two regimes, one below ~400°C and one above ~400°C. Thermal expansion coefficients for $Ba_{0.5}Sr_{0.5}Co_{0.8}Fe_{0.2}O_{3-\delta}$ are shown in Table 1.6. The thermal expansion coefficient of BSCF matches that of YSZ and GDC in the lower temperature range, but begins to deviate substantially at higher temperatures, suggesting that TEC problems will be encountered during high temperature sintering processes.

| Reference | Temp Range (°C) | TEC |
|---|---|---|
| McIntosh et al.[81] | 600-900 | 23.19-24.03 |
| Zhou et al.[82] | 50-400 | 14.4 |
| Zhou et al. | 450-700 | 27.5 |
| Wei et al.[83] | 500-700 | 25.0 |
| Lim et al.[84] | 400-1000 | 31.3 |
| Wei et al. [85] | 50-300 | 11.7 |
| Wei et al. | 400-900 | 24.9 |

Table 1.4. TEC of $Ba_{0.5}Sr_{0.5}Co_{0.8}Fe_{0.2}O_{3-\delta}$.

BSCF is known to experience A-site carbonate formation under atmospheres containing carbon dioxide, resulting in the formation of $BaCO_3$, $SrCO_3$, and $Ba_{1-x}Sr_xCO_3$[86][87][88]. The carbonate phase is nonreactive and blocks available reaction sites, which leads to a decrease in cell performance[89]. A mechanism for this process has been developed by Ge et al.[90] It involves carbon dioxide reacting with surface barium and/or strontium, which leads to a localized A-site deficiency. This causes A-site cations to migrate from the bulk of the particle, leading to a bulk A-site deficiency, under which the perovskite BSCF structure may begin to convert to native cobalt and iron oxides.

### 1.8 AC Impedance Modeling

The ratio of the voltage and current in an AC system is the impedance, Z.

$$(18)\ Z = \frac{V}{i}$$

In the case of EIS, voltage is applied to the system is in the form of a fixed amplitude AC wave, with a changing angular frequency, ω.

$$(19)\ V(t) = V_{peak}\sin(\omega t)$$

A current will flow in response to this applied voltage, with an angular frequency identical to the input wave, but which may be shifted by some phase angle, $\phi$.

$$(20)\ i(t) = i_{peak}\sin(\omega t + \phi)$$

Plugging this back into (18) gives the value of the complex impedance, Z.

$$(21)\ \ Z(t) = \frac{V_{peak}sin(\omega t)}{i_{peak}\sin(\omega t+\phi)}$$

The magnitude of the impedance, |Z|, is the ratio of the peak voltage and peak current.

$$(22)\ \ |Z| = \frac{V_{peak}}{i_{peak}}$$

Both |Z| and $\phi$ may change depending on the input frequency. A plot of |Z| vs. frequency and $\phi$ vs. frequency is known as a Bode Plot. The impedance of the system can also be plotted by splitting Z into its real component, Z' (dependent primarily on |Z|), and its imaginary component, Z'' (dependent primarily on $\phi$). This is called a Nyquist plot.

The importance of AC impedance spectroscopy lies in the fact that multiple processes are occurring on the cathode, and that these processes may occur on different time scales. As the frequency of the AC wave changes from fast to slow, the different processes can be separately identified and modeled.

Equivalent circuits are used to model the response of the system. The various processes are modeled using resistors and capacitors. It is important to note that the elements in the equivalent circuit model do not represent actual resistors and capacitors. In dynamic systems modeling, elements of different types of systems (electrical, mechanical, fluids, etc.) tend to display similar types of behavior, and often share the same mathematical underpinnings. Complex systems can be broken down into a series of simple, interchangeable elements, and modeled using equivalent circuits, regardless of the type of system involved. In an equivalent circuit model, a resistor may represent any process which dissipates energy instantaneously, in an amount proportional to some type of flow variable (current, force, fluid flow) going through it. A capacitor represents any reversible process which stores energy, and where the flow going into the storage element is proportional to the rate of change in some type of potential variable (voltage, velocity, pressure).

Possible models for different processes can be developed by taking into account the relevant time scales of the processes[91], and the partial pressure dependence of the resistance of the process[92]. Broadly speaking these can be divided into three general processes: charge transfer, surface exchange, and gas diffusion. The following sections outline the dependence of the resistance on $PO_2^n$.

*Gas Diffusion (n=-1.0)*

The measured impedance of a resistor, $Z_R$, is similar to the resistance, and defined as the current to voltage ratio. Since the applied voltage is a constant amplitude sine

wave, the impedance is therefore inversely proportional to the amount of current flowing through the "resistor", $i_R$.

$$(23)\ Z_R = \frac{V}{i_R} \rightarrow Z_R \propto \frac{1}{i_R}$$

Under the condition of a gas diffusion-limitation, we assume that the available current is limited only by the amount of $O_2$ getting to the reaction sites on the cathode surface. In this case the current, i, is directly proportional to the gas flux, J ($i \propto J_{O_2}$), and so by Eqn (23) the impedance is inversely proportional to the $O_2$ gas flux.

$$(24)\ Z_{R_{gas}} \propto \frac{1}{J_{O_2}}$$

Gas diffusion for ideal gases in one dimension is described by Fick's law of diffusion,

$$(25)\ J = -D\frac{\partial C}{\partial x}$$

where D is the diffusion constant for the gas. If we assume D is constant under the $PO_2$ range measured (1.0-0.01atm), and concentration gradients are linear, we can estimate the gas flux if we know the gas concentration near the surface of the cathode, $C_{surface}$, and the concentration in the bulk of the gas, $C^*$, over some distance, $\Delta x$.

$$(26)\ J \approx -D\frac{C_{surface} - C^*}{\Delta x}$$

By assuming a low surface concentration ($C^* << C_{surface}$), and constant diffusion distance, the equation simplifies to a simple proportional relationship between flux and bulk gas concentration ($J \propto C^*$). Additionally, since all fitted $PO_2$ measurements are taken at a constant temperature, by the ideal gas law, the bulk gas concentration will be proportional to the bulk gas pressure ($C^* \propto PO_2(bulk)$), so that for the oxygen flux,

$$(27)\ J_{O_2} \propto PO_2(bulk)$$

Plugging this relationship back into Eqn (24) allows us to see the impedance of the resistor as a function of $PO_2$.

$$(28)\ Z_R \propto \frac{1}{PO_2} \rightarrow Z_R \propto (PO_2)^{-1}$$

This implies a $PO_2^n$ dependence of n=-1.0 for gas diffusion limitation.

*Charge Transfer of $O^{2-}$ (n=0.25)*

A charge transfer reaction may occur from the cathode to the electrolyte. On the cathode side, this involves the transfer of an $O^{2-}$ ion across the cathode-electrolyte interface, creating a positively charged vacancy. On the electrolyte side, under equilibrium, the $O^{2-}$ will continue moving through the electrolyte as part of an ionic flow, $j_{O^{2-}}$.

$$(29)\ O_O^{\times}(cathode) \rightarrow V_O^{\cdot\cdot}(cathode) + O^{2-}\ (electrolyte)$$

When this process is the rate-limiting step, we assume a steady flow of $O^{2-}$ ions are coming to the cathode-electrolyte interface. The $O^{2-}$ ions are formed by some other process, elsewhere in the system. Although the exact nature of this other process may not be known, we will assume that the overall reaction will result in an oxygen atom combining with two electrons to produce the $O^{2-}$ ions.

$$(30)\ O_O^{\times} \rightarrow V_O^{\cdot\cdot} + \frac{1}{2}O_2 + 2e^-$$

The expression for the equilibrium constant gives the vacancy concentration under these conditions in terms of the other constituents.

$$(31)\ K = \frac{[O_O^{\times}]}{[V_{\ddot{O}}]*(PO_2)^{\frac{1}{2}}*[e]^2} \rightarrow [e] = \frac{1}{K}\frac{[O_O^{\times}]^{\frac{1}{2}}}{[V_O^{\cdot\cdot}]^{1/2}*(PO_2)^{\frac{1}{4}}}$$

If we assume that the measured current is proportional to the number of electrons generated ($i_{R_{ct}} \propto [e]$), we get the overall pressure-current relationship.

$$(32)\ i_{R_{ct}} \propto (PO_2)^{1/4}$$

And using the definition for the impedance of a resistor (6) gives us the final relationship.

$$(33)\ Z_{R_{ct}} \propto \frac{1}{i_{R_{ct}}} \rightarrow Z_{R_{ct}} \propto \frac{1}{(PO_2)^{1/4}}$$

Overall this will result in a $PO_2^n$ dependence of n~-0.25 if there is a charge transfer limitation.

*Surface Exchange involving complete $O^{2-}$ reduction (n=0.25)*

A partial pressure dependency of n~-0.25 can be explained by a surface adsorption process. The reaction involves the transfer of gaseous oxygen into a vacancy site.

$$V_O^{\cdot\cdot} + \frac{1}{2}O_2 + 2e^- \rightarrow O_O^{\times}$$

The equilibrium rate constant can be found for this reaction.

$$(34)\ K = \frac{[O_O^{\times}]}{[V_O^{\cdot\cdot}]*(PO_2)^{\frac{1}{2}}*[e]^2} \rightarrow [e] = \frac{1}{K}\frac{[O_O^{\times}]^{\frac{1}{2}}}{[V_O^{\cdot\cdot}]^{1/2}*(PO_2)^{\frac{1}{4}}}$$

If surface processes are the rate-limiting step, the absorbed $O^{2-}$ ions will migrate towards the electrolyte after this step, where they undergo charge transfer to the electrolyte, creating an oxygen vacancy. We assume that the high frequency charge transfer process is in equilibrium, and so any vacancies filled by $O_2$ at the cathode surface will be balanced out by vacancies created by $O^{2-}$ charge transfer to the electrolyte. Practically

speaking, this means that the overall ratio of vacancies to lattice oxygen in the cathode becomes fixed ($\frac{[V_O^{\cdot\cdot}]}{[O_O^{\times}]} = k$), and (34) can be simplified.

$$(35)\ [e] \propto \frac{1}{(PO_2)^{\frac{1}{4}}}$$

Electrons are being consumed by the process. The measured current is actually a response to the lack of electrons, and so for this case we assume that the measured current will be inversely proportional to the concentration of electrons ($i \propto \frac{1}{[e]}$). The current can then be related to $PO_2$.

$$(36)\ i_{R_{surf}} \propto (PO_2)^{1/4}$$

Using the definition for impedance of a resistor (6).

$$(37)\ Z_{R_{surf}} \propto \frac{1}{i_{R_{surf}}} \rightarrow Z_{R_{surf}} \propto \frac{1}{(PO_2)^{1/4}}$$

This ultimately gives the relationship between Z and $PO_2$ as n=0.25, for the case of a surface exchange process involving the complete reduction of oxygen (transfer of 2 $e^-$).

*Surface Exchange involving partial $O^{2-}$ reduction (n=0.50)*

For the case of a partial reduction of oxygen (transfer of 1 e-), the reaction is given below.

$$(38)\ V_O^{\cdot\cdot} + \frac{1}{2}O_2 + e^- \rightarrow O_O^{\cdot}$$

The equilibrium rate constant can be found for this reaction.

$$(39)\ K = \frac{[O_O^{\cdot}]}{[V_O^{\cdot\cdot}]*(PO_2)^{\frac{1}{2}}*[e]} \rightarrow [e] = \frac{1}{K}\frac{[O_O^{\cdot}]}{[V_O^{\cdot\cdot}]*(PO_2)^{\frac{1}{2}}}$$

Again making the same assumptions as were made for the case of complete oxygen reduction, we can obtain the overall dependency.

$$(40) \quad Z_{R_{surf}} \propto \frac{1}{(PO_2)^{1/2}}$$

Therefore if the process involves only a partial reduction of the oxygen ion at the surface, the $PO_2^n$ dependency will be n=0.5.

The determination of the partial pressure dependence for the surface exchange process is a powerful tool, as it allows us to use the partial pressure dependence to determine how the surface exchange reaction is proceeding. A transition from a dependence of 0.25 and to a dependence of 0.50 suggests a transition of the dominant reaction pathway from partial reduction of the oxygen atoms and surface diffusion, to complete reduction of the oxygen atoms, followed by bulk diffusion.

# Chapter 2

# Experimental

## 2.1 Powder Synthesis

Synthesis of A-site deficient [A=0.97] $Ba_{0.5}Sr_{0.5}Co_{0.8}Fe_{0.2}O_3$ (BSCF) and $Ba_{0.45}Sr_{0.45}Sm_{0.10}Co_{0.8}Fe_{0.2}O_3$ (BSSCF) were attempted by two different synthesis routes: glycine nitrate combustion and EDTA-citrate. Commercially available $La_{0.58}Sr_{0.4}Co_{0.2}Fe_{0.8}O_3$ (NexTech, particle size 0.3-0.6μm) and $Ba_{0.5}Sr_{0.5}Co_{0.8}Fe_{0.2}O_3$ (Praxair, particle size 1.5-4μm) were also obtained, in order to serve as baselines.

*Determination of Cation Concentrations*

Metal nitrates were used as the source of the cations, as nitrate will easily burn off during high temperature calcination, leaving no residue in the synthesized powder. All of the relevant cations can be obtained in the form of nitrate salts, which are cheap and readily available. First the metal-nitrates were dissolved in deionized water, each in a different 1L container: $Ba(NO_3)_2$, $Sr(NO_3)_2$, $Co(NO_3)_2*6H_2O$, and $Fe(NO_3)_3*9H_2O$. The cation concentration of each solution was then characterized, in order to account for any hydration of the metal nitrate salts that may lead to an incorrect stoichiometry in the synthesized powder. To this end, three techniques were attempted. Inductively coupled plasma testing was the first attempted, using a Perkin Elmer/DRC-e Inductively Coupled Plasma Mass Spectrometer (UConn, CESE). This technique proved ineffective. The detection ceilings for the metals tested is low (on the order of several ppm), and the solution had to be serially diluted, leading to high uncertainty in the final numbers.

Next the cation concentration was characterized by chemical titration. Ethylenediaminetetraacetic acid (EDTA) was used as a complexing agent, with Eriochrome Black T (EB) as the complexometric indicator. Several drops of an indicator

solution containing EB, water, and a small amount of MgCl2 was added to the metal-nitrate solution to be tested. EDTA was mixed with ammonia hydroxide to obtain a pH of 9. This solution was added to the metal-nitrate solution through a burette, and stopped when the color change reaction occurred. The EDTA bonds to the cations in a 1:1 molar ratio, and since the amount of EDTA added before the color change is known, the cation concentration of the solution can be calculated. This method worked for both the $Ba(NO_3)_2$ and $Sr(NO_3)_2$ solutions, but the high pH level involved caused formation of hydroxides in the $Co(NO_3)_2$ and $Fe(NO_3)_3$ solutions.

In order to characterize the cation content of the $Co(NO_3)_2$ and $Fe(NO_3)_3$ solutions, the solutions were placed in alumina crucibles, and heated to 800°C to form metal oxides. After confirmation of single phase metal oxide structures, the cation content of the initial sample could be calculated from the weight of the oxides formed. This method worked for $Sr(NO_3)_2$, $Co(NO_3)_2$, and $Fe(NO_3)_3$, but reaction between Ba and the alumina crucible was observed in the case of $Ba(NO_3)_2$.

*Glycine Nitrate Combustion Synthesis*

Once the cation concentrations were known, synthesis was attempted by the glycine nitrate process[93]. Metal-nitrate salts were used as a source of cations: $Ba(NO_3)_2$, $Sr(NO_3)_2$, $Co(NO_3)_2*6H_2O$, and $Fe(NO_3)_3*9H_2O$ were weighed in the appropriate stoichiometric ratio, using the cation concentrations found previously. Glycine was added in a glycine:nitrate molar ratio of 0.6:1. The water was evaporated under stirring and low heat for several days until a gel formed. The temperature was increased until

combustion of the gel took place. The reaction product was calcined for 2h at 850-1000°C. The overall process is shown in the form of a flow chart in Figure 2.1

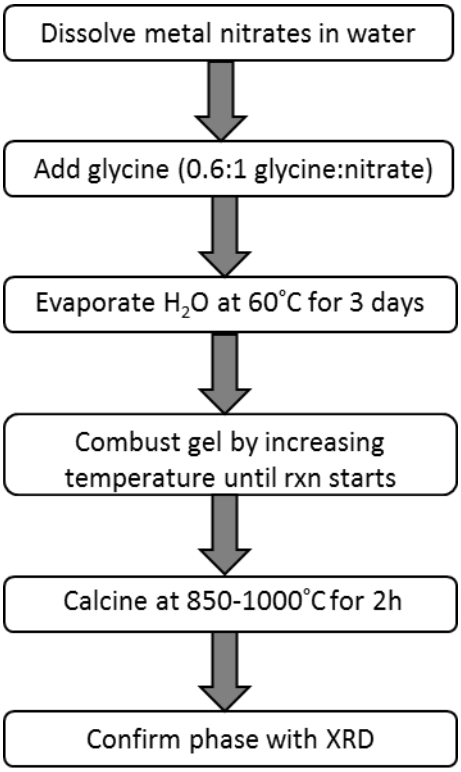


Figure 2.1. Flow chart showing the steps of the glycine-nitrate combustion process.

This process involves high temperature combustion of the glycine and nitrate. We found that this resulted in the formation of carbonates when synthesizing BSCF (although we have previously synthesized LSCF and other perovskites using this technique). In response to this challenge, we decided to explore alternative synthesis routes.

*EDTA-Citrate Synthesis*

The EDTA-citrate technique was used to synthesize BSCF and BSSCF. Metal-nitrates were dissolved in water and added in the appropriate stoichiometric ratios, as

determined by the previously described cation characterization experiments. EDTA was added to the solution in a cation:EDTA molar ratio of 1:1. Citrate was added in a cation:citrate molar ratio of 1:2. The pH of the solution was kept around 9, through the addition of ammonium hydroxide. The water was then evaporated from the solution, by placing it under low heat and constant stirring for several days. The mixture was then placed in a low temperature oven for 12h at 180°C, after which a lightweight powdery foam was produced. This foam was crushed and ground using a mortar and pestle, and then calcined for 2h at 850-1000°C. XRD was used to confirm single phase structure. In the case of BSSCF, subsequent regrinding and recalcination steps were required to obtain single phase chemistry. A flow chart representing this process is given in Figure 2.2.

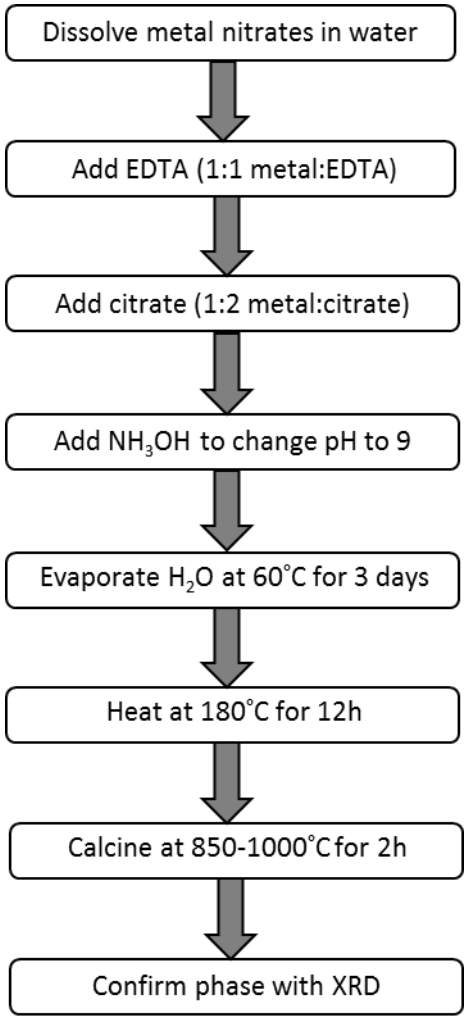


Figure 2.2. Flow chart showing the steps of the EDTA-citrate process.

## 2.2 Powder Characterization

*XRD, SEM and BET Analysis*

X-Ray Diffraction (XRD) was used to determine the phase structure of the powders. A Bruker D8 Advance Diffractometer system was used, with Cu Kα radiation (λ=1.54Å), and scans from 10 to 90°. XRD analysis was performed on the powder immediately after synthesis to confirm the synthesized phase structure. To check for the stability of the phase, XRD analysis was also performed after 500h in ambient air, to test

for secondary bulk phase formation after storage in stagnant air. In order to characterize the formation of the secondary phase under extended time at expected operating temperatures (~600°C) and under $CO_2$, samples of BSCF powder were placed under flowing dry air, humidified air, or $CO_2$ for 150h, and examined afterwards using XRD.

In order to characterize the morphology of the powders, samples were examined using secondary electron microscopy (SEM). A FEI Quanta 250 FEG field emission scanning electron microscope was used. The powders were examined immediately after synthesis. In order to test the formation of secondary surface phases, the powder was also examined after 24, 100, and 500h after synthesis.

BET analysis was performed using a Micromeretics ASAP 2020 Automatic Chemisorption Analyzer. The surface area of the powders was found to be 0.37 $m^2/g$ for BSCF, 0.46 $m^2/g$ for BSSCF, 6.5 $m^2/g$ for commercially produced LSCF.

*Thermogravimetric and Thermal Expansion Measurements*

Thermogravimetric analysis was carried using a Netzsch STA 449 F3 Jupiter Simultaneous Thermal Analyzer. Samples were ~20mg, and were placed in an alumina crucible, for testing in flowing air, in a temperature range of 50-800°C (5°C/min).

Pellets of BSCF powder were pressed uniaxially at 225 MPa. As we experienced difficulty getting dense, crack-free pellets using traditional heating/cooling cycles, we adapted a sintering profile developed by Reid et al.[94] The sintering profile is shown in Table 2.1. The sintered BSCF pellets were subsequently cut and ground using 320 grit SiC carbide paper to form bars 1.7x3.9x10.2 mm.

| | |
|---|---|
| Step 1 | Ramp 25-850 (5C/min) |
| Step 2 | Ramp 850-1050 (2C/min) |
| Step 3 | Dwell 1050 (30min) |
| Step 4 | Ramp 1050-1150 (1C/min) |
| Step 5 | Ramp 1150-1130 (1C/min) |
| Step 6 | Dwell 1130 (240min) |
| Step 7 | Ramp 1130-850 (2C/min) |
| Step 8 | Ramp 850-25 (5C/min) |

Table 2.1. Sintering profile of the BSCF pellet used for TEC testing.

Bars were also pressed out of LSCF, GDC, and the LSCF-GDC composite powders, under 120MPa, and sintered for 5h at 1300°C. After sintering, the rectangular bars were 4.0x2.4x17mm. TEC was measured using a Netzsch DIL 402 PC dilatometer, in a range of 25-1000°C, with a heating rate of 3°C/min.

The bars were tested in a Netzsch DIL 402 PC dilatometer, in stagnant air, in a temperature range of 25-800°C, with a heating rate of 3°C/min.

## 2.3 Symmetric Cell Fabrication

*Ink preparation*

Inks were prepared using the powders and ink vehicle (NexTech). Ink vehicle and powder were mixed together by hand using a mortar and pestle, in a powder:vehicle wt. ratio of 0.7:0.3. In order to improve the consistency of the ink, a three-roll mill was used to mechanically grind together the powder and ink vehicle after being ground by hand. The powder:vehicle slurry was passed through the mill repeatedly, breaking agglomerates and resulting in a thicker, more homogenous ink mixture.

*Fabrication of Electrolyte Support*

The electrolyte used in all the studies in this thesis was $Ce_{0.8}Gd_{0.2}O_2$ (GDC). Electrolyte pellets were pressed from GDC powder (Rhodia) under an uniaxial load of 225 MPa, and sintered for 5h at 1300°C. Sintered pellets were ~11mm dia., and 0.8mm thickness. The surface of the pellets was roughed using 320 grit SiC sandpaper, followed by ultrasonic washing in water.

*Electrode Deposition*

To improve the repeatability of the cathode layer deposition process, a screen printer was used. The screen was 105 mesh, with 0.7 mil wire. The screen pattern was an open 10 mm dia. circle. A squeegee pressure of 30 psi was used, at an angle of 35°. Cathode ink was screen printed onto both sides of the pellet, and the pellets were sintered for 2h at 1000°C. For the BSCF and LSCF symmetric cells, a current collecting layer was applied using Ag ink (Alfa Aesar), and bonded by heating to 800°C for 2h.

## 2.4 AC Impedance Spectroscopy

*Impedance Testing Parameters*

AC impedance testing was performed in a flowing gas atmosphere, with $PO_2$ varying from 1.0 to $10^{-4}$ atm, controlled by the mixing of $N_2$ and $O_2$ gases. The temperature range was 500-700°C, in 50°C intervals. Silver mesh current collectors were pressed against the cell by the quartz test rig, with pressure supplied by springs in the cold zone. Impedance spectroscopy was carried out using a Solartron 1260 Impedance/Gain-Phase Analyzer, and a Solartron 1287 Electrochemical Interface, as well

as a Princeton Applied Research Potentiostat. A 20mV amplitude voltage wave was applied, in a frequency range of 1MHz to 10mHz. A schematic of the test set up is shown in Figure 2.3.

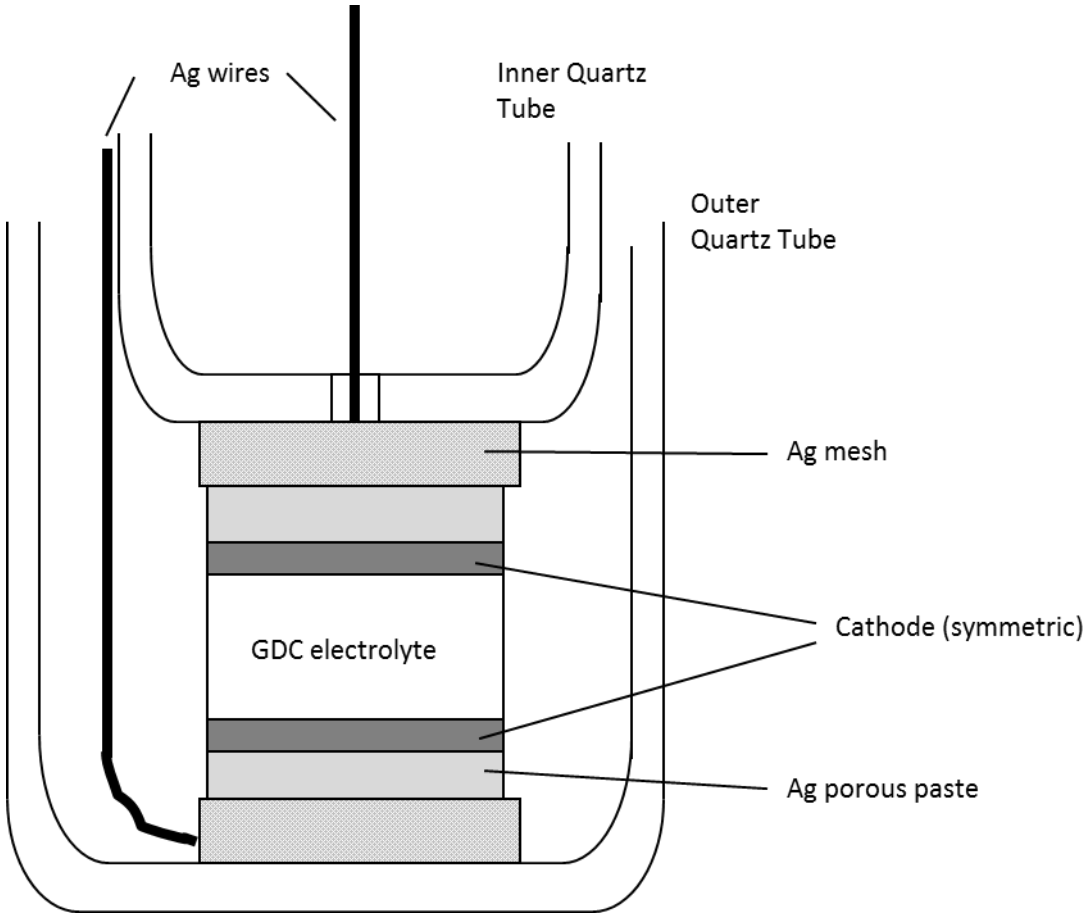


Figure 2.3: Schematic showing the arrangement of the symmetric cell and quartz test rig.

*Equivalent Circuit Modeling*

Each process was modeled as an RC circuit, with a resistor and a capacitor in parallel. Constant phase elements (CPE) were used instead of ideal capacitors. An ideal capacitor will intersect the Z' axis as a perfectly vertical line, but in a CPE, this angle has been shifted from 90°. The overall effect of this, as seen in the Nyquist plot, is that the

processes appear as depressed semicircles, with the extent of the depression depending on a constant, n (when n=1, the CPE acts a pure capacitor, but n<1 results in CPE behavior).

An ideal resistor ($R_{ohmic}$) was used to model ohmic resistance in the system, coming from the electrolyte and current collecting wires. A fixed impedance value of $9x10^{-7}H$ was used to model the impedance ($L_1$) in the current collecting wires.

The equivalent circuit model used is shown in Figure 2.4. An example of the model fit for an LSCF symmetric cell at 650°C and 0.04 atm $PO_2$ is shown in Figure 2.5, with both Nyquist and Bode plots.

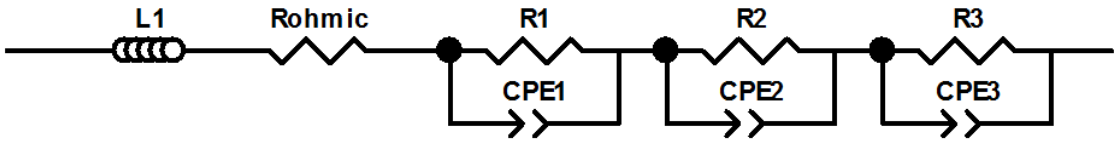


Figure 2.4. Equivalent circuit model used for LSCF and BSCF symmetric cells.

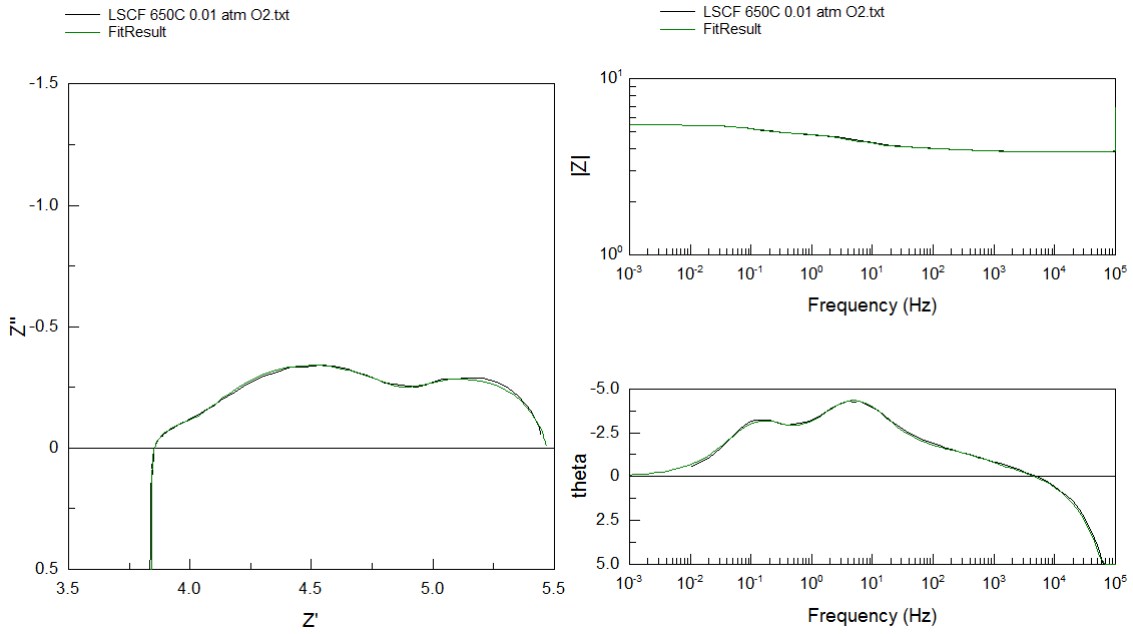


Figure 2.5. Impedance spectra and Bode plot for a LSCF symmetric cell at 650°C in 0.01 atm $O_2$, showing the measured data (*black*) and the fitted model (*green*).

# Chapter 3

# Results and Discussion

### 3.1 Electrochemical Analysis of LSCF-GDC (varying wt.%) composites

The normalized impedance spectra for the different compositions at 600ºC are shown in Figure 3.1. The overall area specific resistance (ASR) of the cell is considered to be the horizontal length of the semicircles, the distance between the two x-axis intercepts. The ASR values for the different compositions at different temperatures are given in Table 3.1.

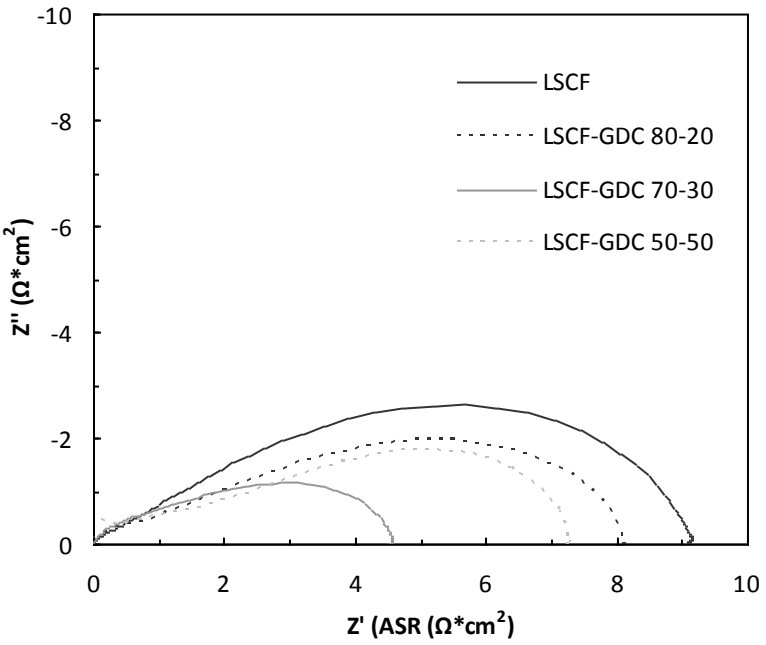


Figure 3.1. AC impedance spectra for LSCF-GDC composites at 600ºC.

| ASR (Ω*cm$^2$) | 400°C | 500°C | 600°C | 700°C | 800°C |
|---|---|---|---|---|---|
| LSCF | 50 | 40.7 | 9.1 | 1.80 | 0.49 |
| LSCF-GDC 80-20 | 111 | 35.9 | 8.1 | 2.92 | 1.55 |
| LSCF-GDC 70-30 | 168 | 21.1 | 4.6 | 1.61 | 0.61 |
| LSCF-GDC 65-35 | 324 | 33.5 | 7.7 | 2.14 | 0.79 |
| LSCF-GDC 60-40 | 57 | 33.0 | 15.8 | 4.77 | 1.59 |
| LSCF-GDC 50-50 | 218 | 24.0 | 6.7 | 2.16 | 1.29 |

Table 3.1. Table showing ASR for different LSCF-GDC composites at 400-800°C.

The overall resistance changes with the relative proportion of LSCF and GDC in the composite. The effect of the GDC loading can be seen in Figure 3.2.

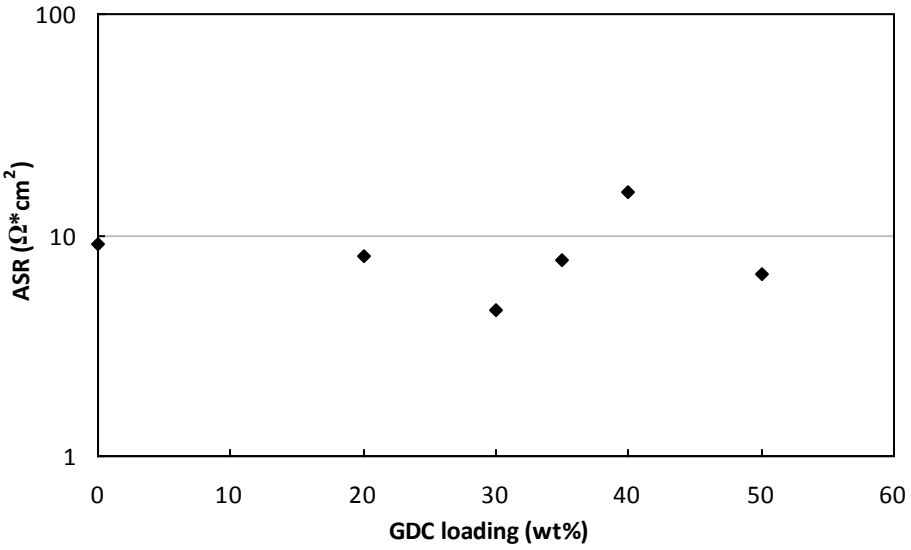


Figure 3.2. Plot of GDC loading vs. ASR at 600ºC

The lowest measured ASR at 600ºC was for the LSCF 70-30 wt.% composition, which is at a low compared to the other points. This result is consistent with Dusastre, Kilner[95], who explain this phenomenon by use of a percolation model. At a certain loading, both phases are present in sufficient amounts to provide a contiguous network of each phase, resulting in an increase in performance, and a decrease in ASR.

The effect of temperature on the compositions is shown in Figure 3.3.

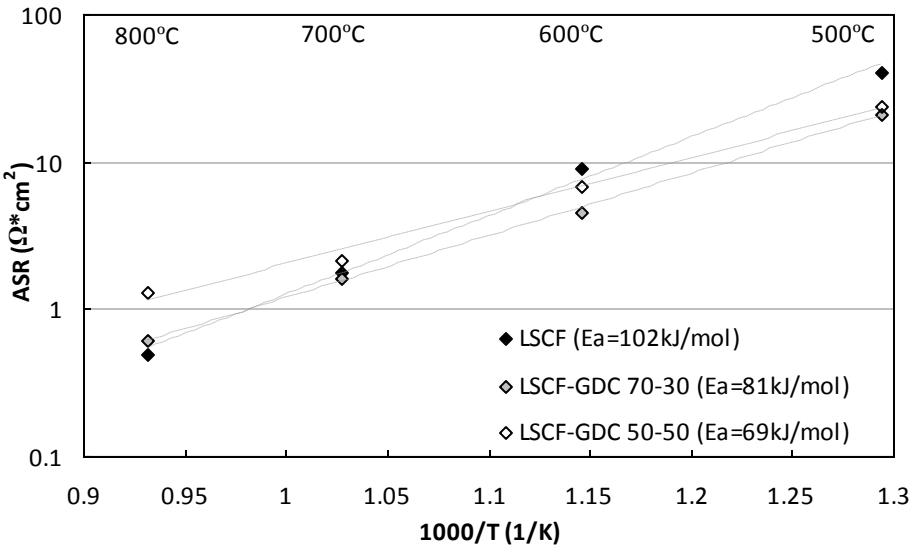


Figure 3.3. Plot of 1000/T vs. ASR for selected compositions.

A change in activation energy is observed with a change in composition, with higher activation energy for pure LSCF than the composites. As discussed in Chapter 1, diffusion limited processes tend to have higher activation energies than processes limited by surface exchange. This could explain the differences in activation energies observed between the single phase LSCF and the composites. In single phase LSCF, the high activation energy suggests a diffusion limitation. Addition of the ionic conducting electrolyte phase (GDC) would improve the diffusion of $O^{2-}$ ions in the cathode, making composites more likely to be limited by surface exchange processes instead of diffusion.

The results from the dilatometer measurements are shown in Figure 3.4. The measured thermal expansion coefficient (TEC) of our GDC sample was found to be 12.6 ppm/K, which matches reported literature[96]. LSCF was found to have a TEC of 16.7 ppm/K, also in line with reported literature[97]. The TEC of the composites was found to be in the middle, with higher GDC loading resulting in lower TEC. Since GDC is the

electrolyte used in our studies, this suggests that the composites will have less TEC mismatch than single phase LSCF.

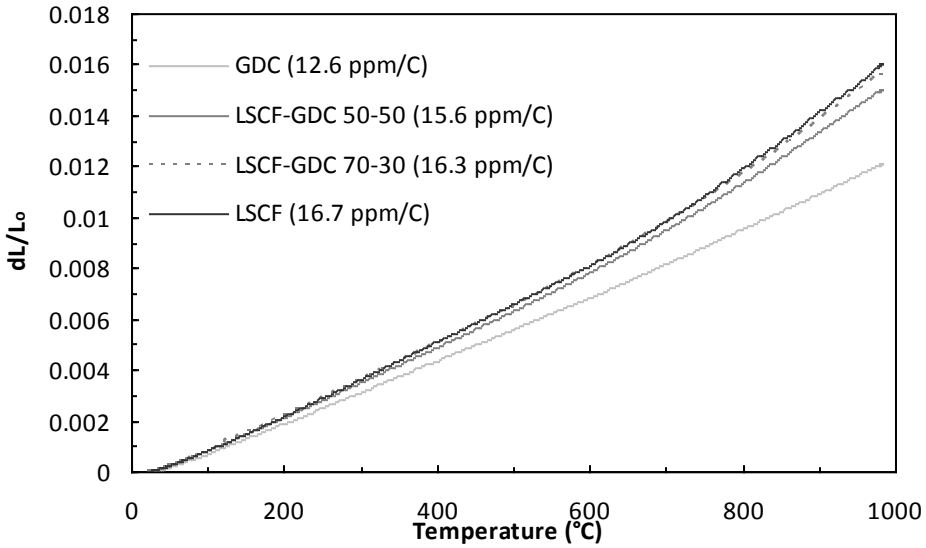


Figure 3.4. Thermal expansion curves for LSCF, GDC, and LSCF-GDC composites.

### 3.2 Comparison of electrochemistry of commercially available LSCF and BSCF

In order to explore alternative materials families, a study was undertaken to test $Ba_{0.5}Sr_{0.5}Co_{0.8}Fe_{0.2}O_{3-\delta}$ (BSCF). A small amount of commercially produced BSCF powder was obtained as a starting point for this study. SEM images of a cross section of the BSCF cathode layer after sintering are shown in Figure 3.5. The BSCF layer was ~16μm thick, with an average particle size of 1-4 μm, and a visible network of interconnected pores. The thickness of the layer was very uniform, due to the use of screen printing for our electrode deposition.

a) Porous BSCF cathode layer on GDC electrolyte (2000x)

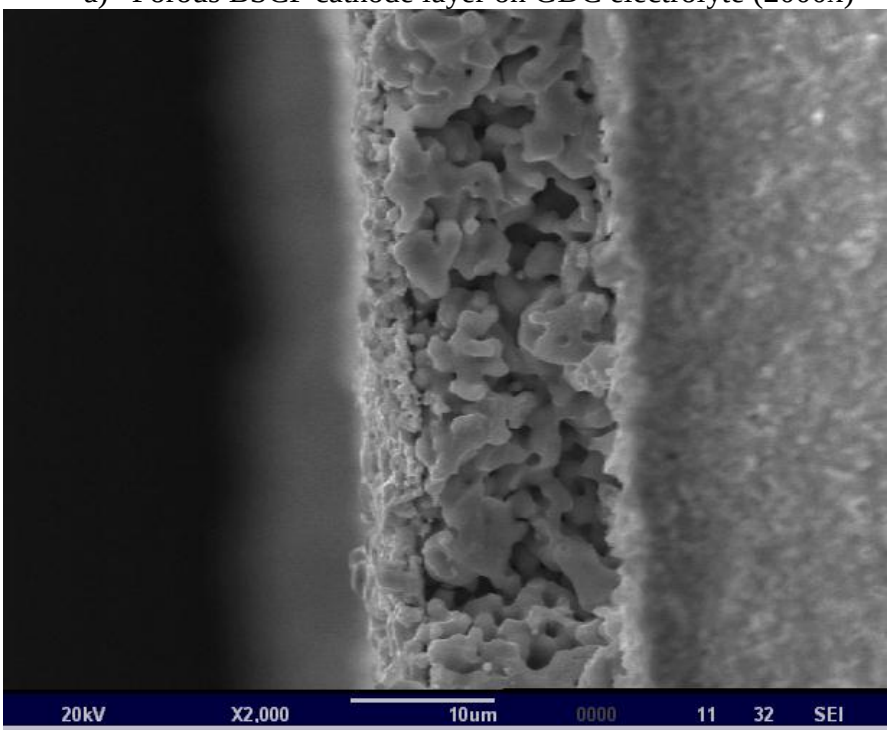


b) Higher mag image of BSCF cathode layer (4000x)

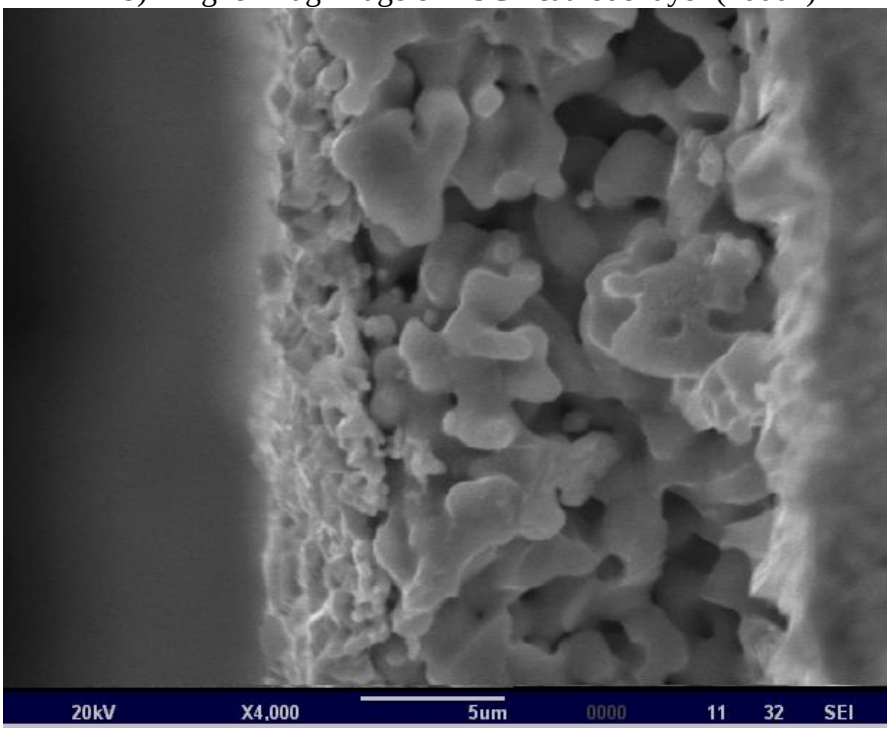


Figure 3.5. SEM images of a BSCF cathode layer on GDC, sintered 2h at 1000°C, at a)2000x magnification, and b) 4000x magnification.

AC impedance testing of four different BSCF cells showed remarkable agreement in their measured ASR, as seen in Table 3.2. The good reproducibility of the results may be due to the application of an Ag current collecting layer on top of the cathode, allowing more reliable and consistent connection with the Ag mesh electrical contacts. Plots of ASR as a function of temperature, along with a comparison with LSCF, are shown in Figure 3.6.

| **ASR ($\Omega$*cm$^2$)** | 500°C | 550°C | 600°C | 650°C | 700°C | 750°C |
|---|---|---|---|---|---|---|
| BSCF (cell 1) | 5.3 | 1.44 | 0.45 | 0.17 | 0.10 | 0.075 |
| BSCF (cell 2) | 4.5 | 1.23 | 0.41 | 0.17 | 0.09 | 0.066 |
| BSCF (cell 3) | 4.1 | 1.49 | 0.55 | 0.23 | 0.12 | 0.079 |
| BSCF (cell 4) | 4.5 | 1.56 | 0.39 | 0.14 | 0.09 | 0.066 |

Table 3.2. ASR values of BSCF symmetric cells tested in stagnant air.

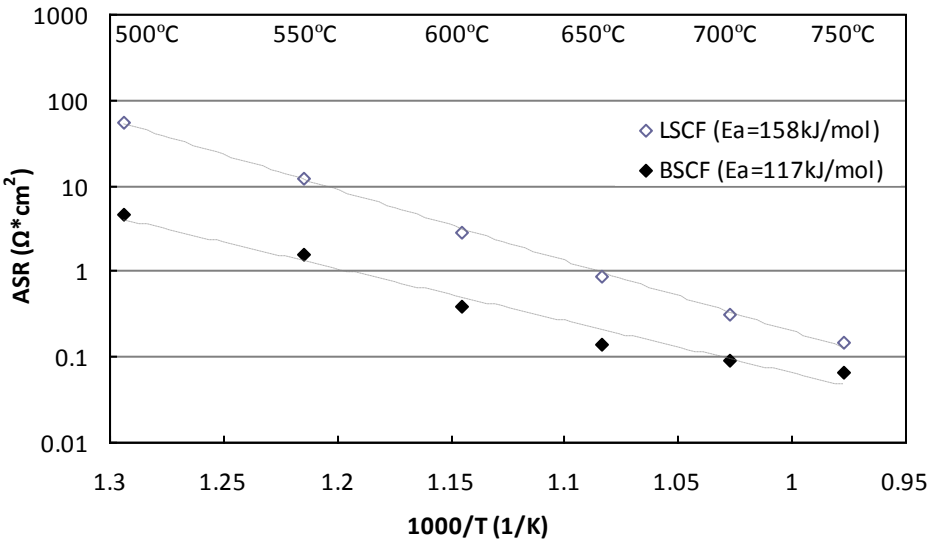


Figure 3.6. ASR values vs. 1000/T for BSCF and LSCF symmetric cells.

The ASR for BSCF was found to be substantially lower than LSCF in this temperature range. The LSCF cell demonstrated an ASR of 2.9 $\Omega$cm$^2$ at 600°C,

compared to 0.39 $\Omega cm^2$ for the highest performing BSCF cell. Cells operating at intermediate temperatures will have less cathode resistance (and therefore produce more power) if they use BSCF as a cathode. In the context of this study, it suggested that further study of BSCF was warranted. Unfortunately, our supply of commercially produced powder was small (<100g), and we were unable to identify any active commercial suppliers of BSCF. In order to proceed with additional studies, BSCF would have to be synthesized in the lab.

### 3.3 Synthesis and Characterization of BSCF and BSSCF Powders

*Powder Synthesis and Characterization*

In order to synthesize A-site deficient $(Ba_{0.5}Sr_{0.5})_{0.97}Co_{0.8}Fe_{0.2}O_{3-\delta}$ (BSCF), we first had to accurately characterize the cation content of our source chemicals. Nitrate salts were used as a source of cations for the synthesis process: $Ba(NO_3)_2$, $Sr(NO_3)_2$, $Co(NO_3)_2*6H_2O$, and $Fe(NO_3)_3*9H_2O$. Nitrate salts can hydrate over time, and taking into account batch-to-batch variation, the bottle-listed level of hydration is of questionable accuracy. To ensure correct stoichiometry of the synthesized compound, the cation content of the nitrate salts was measured prior to synthesis.

Our first attempt involved the use of inductively coupled plasma mass spectrometry (ICP-MS) performed on aqueous solutions of the nitrate salts. The samples needed to be diluted to be within acceptable detection limits of the equipment, and this dilution leads to high margins of error for this technique. The next technique attempted was a simple heating experiment, where nitrate salts were heated to 800°C, in order to

decompose and form their native oxides. This technique did not work for the barium nitrate sample, because of a vigorous reaction between the $Ba(NO_3)_2$ and the alumina crucible. Barium and strontium nitrate cation content was measured using a standard water hardness technique, EDTA titration. This method required high pH, which lead to formation of hydroxides in the cobalt and iron nitrates, precluding the use of this technique for the iron and cobalt samples. The measured molar content of the nitrate salts found by the two methods are shown in Table 3.3, as well as a comparison with the nominal (bottle-listed) cation concentration. From this table, it can be seen that the measured concentrations match well with the bottle-listed concentrations. Furthermore, the case of $Sr(NO_3)_2$ offers a direct comparison of the two methods. The experimentally observed values of the cation concentration were very similar for the two methods (less than 1% difference), further confirming the validity of the two approaches.

| **Cation Conc. (mol/L)** | $Ba(NO_3)_2$ | $Sr(NO_3)_2$ | $Co(NO_3)_2*6H_2O$ | $Fe(NO_3)_3*9H_2O$ |
|---|---|---|---|---|
| EDTA titration | 0.1903 | 0.708 | $Co(OH)_2$ formation | $Fe(OH)_3$ formation |
| Oxide formation | Rxn w/ crucible | 0.700 | 1.183 | 0.285 |
| ICP-MS | 0.23 | 1.08 | 0.98 | 0.22 |
| Nominal (calculated from bottle) | 0.1907 | 0.714 | 1.143 | 0.286 |

Table 3.3. Cation concentrations of $Ba(NO_3)_2$, $Sr(NO_3)_2$, $Co(NO_3)_2*6H_2O$, and $Fe(NO_3)_3*9H_2O$, as measured by EDTA titration, oxide formation, and ICP-MS.

In the past, our lab has used the glycine-nitrate combustion process to synthesize LSCF and other perovskites. We initially attempted to synthesize BSCF by the same

route. The XRD spectra of the resulting powder can be seen in Figure 3.7, along with the XRD spectra of the BSCF powder provided by Praxair.

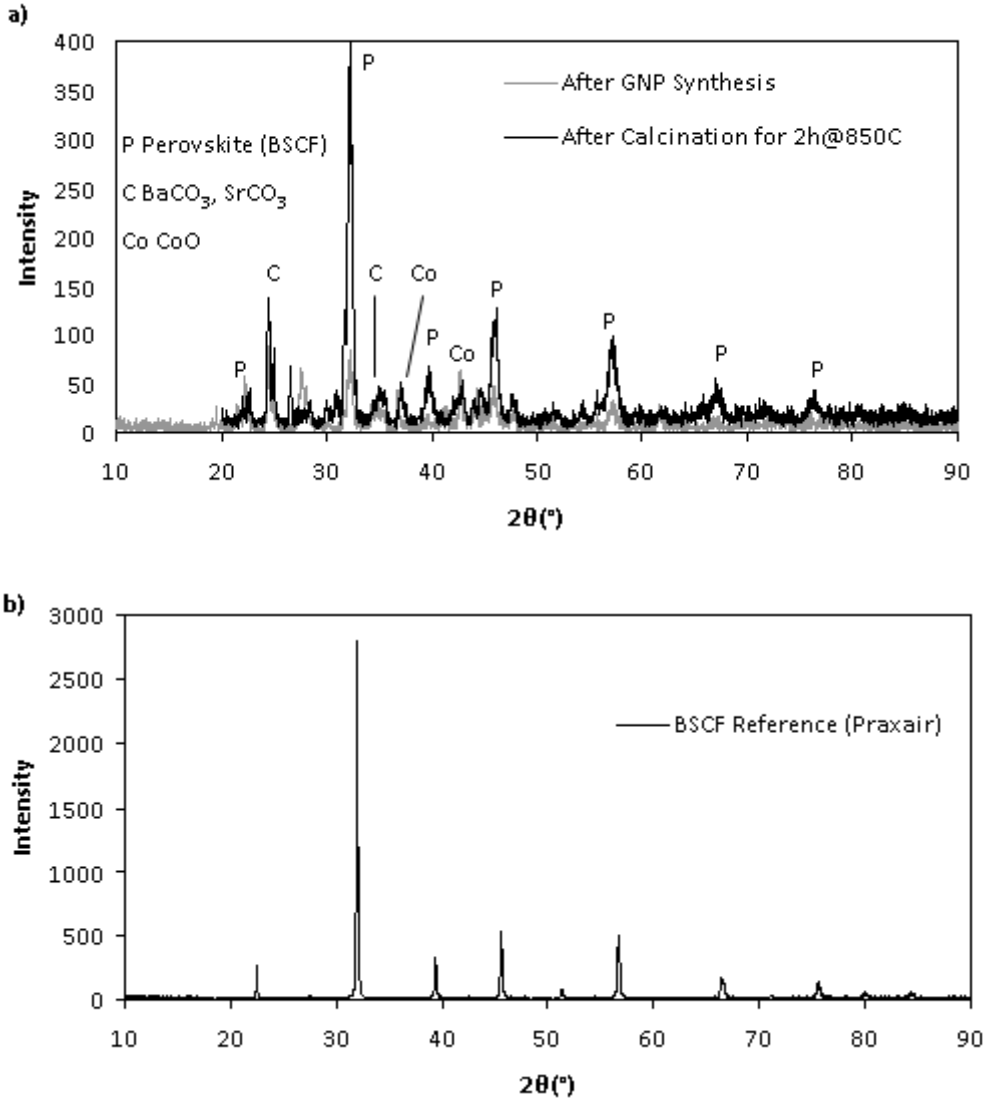


Figure 3.7. XRD spectra of a) $(Ba_{0.5}Sr_{0.5})_{0.97}Co_{0.8}Fe_{0.2}O_{3-\delta}$ synthesized in our lab by the glycine nitrate process, before and after calcination for 2h at 850°C; and b) $Ba_{0.5}Sr_{0.5}Co_{0.8}Fe_{0.2}O_{3-\delta}$, powder produced by Praxair

The powder produced by the GNP synthesis had peaks common to the BSCF reference sample, but had secondary phases present as well. Some of the significant

peaks corresponded to carbonates and cobalt oxide. Formation of carbonates occurs during the high temperature combustion step, leading to A-site deficiency, and subsequent formation of cobalt oxide as a result of the excess of B-site cations.

The EDTA citrate method was tested as an alternative synthesis route. Unlike the glycine nitrate process, it does not require a high temperature combustion step. After synthesis, the powder was calcined at various temperatures to determine optimal calcination temperature. The XRD spectra are shown in Figure 3.8. The BSCF peaks can be indexed to standard perovskite peaks[98], confirming perovskite phase formation. The sample calcined at 850°C showed a secondary phase, with a peak at 2θ=27.4° (inset on Figure 3.8), and an additional peak around 42.5°. Increased temperature suppressed the formation of the secondary phase, and no secondary phase peaks were detectable when the powder was calcined at 900°C or above.

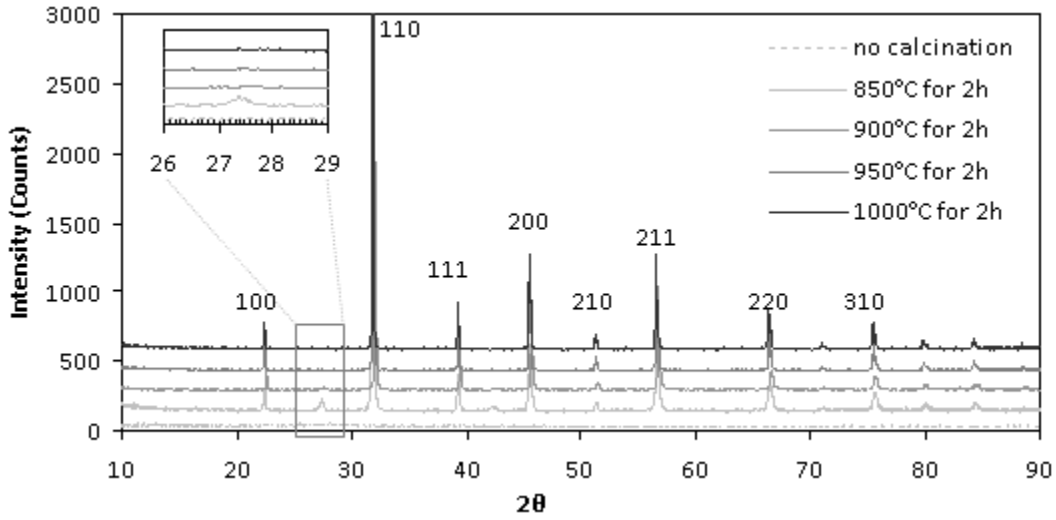


Figure 3.8. XRD spectra for $(Ba_{0.5}Sr_{0.5})_{0.97}Co_{0.8}Fe_{0.2}O_{3-\delta}$ powder synthesized by the EDTA-citrate method, and calcined at 850-1000°C.

We were also able to synthesize Sm-doped BSCF, $(Ba_{0.5}Sr_{0.5})_{0.92}Sm_{0.05}Co_{0.8}Fe_{0.2}O_{3-\delta}$ (BSSCF) using the EDTA-citrate method. The results can be seen in the XRD spectra in Figure 3.9a. Despite raising the sintering temperature up to 1000°C, a secondary SmO phase persisted, suggesting the difficulty of getting uniform and complete diffusion of the $Sm^{3+}$ cation into the perovskite lattice structure. The powder was ground in a mortar and pestle and recalcined until the secondary phase was below the detection limits of the XRD spectrometer. The results of this process can be seen in Figure 3.9b.

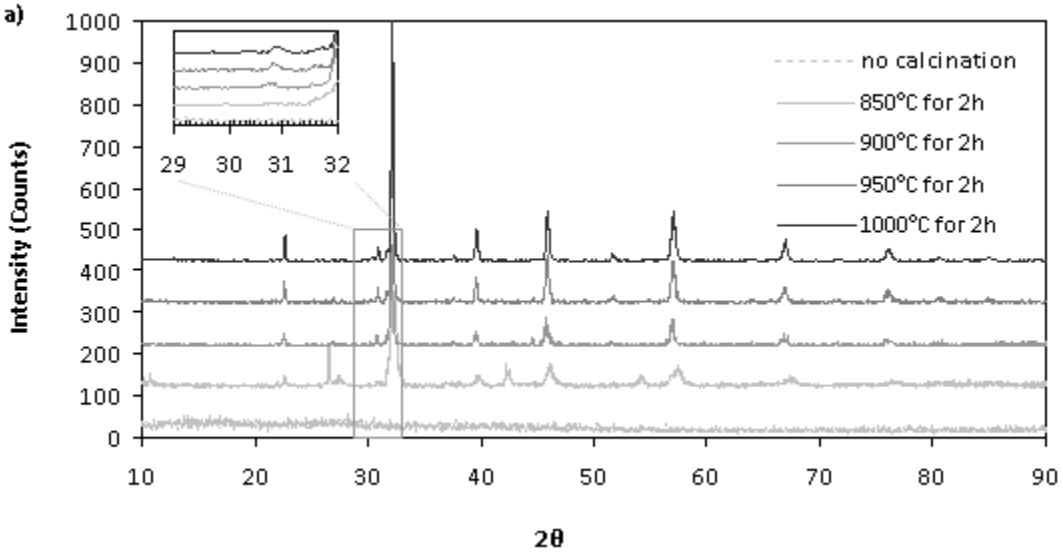

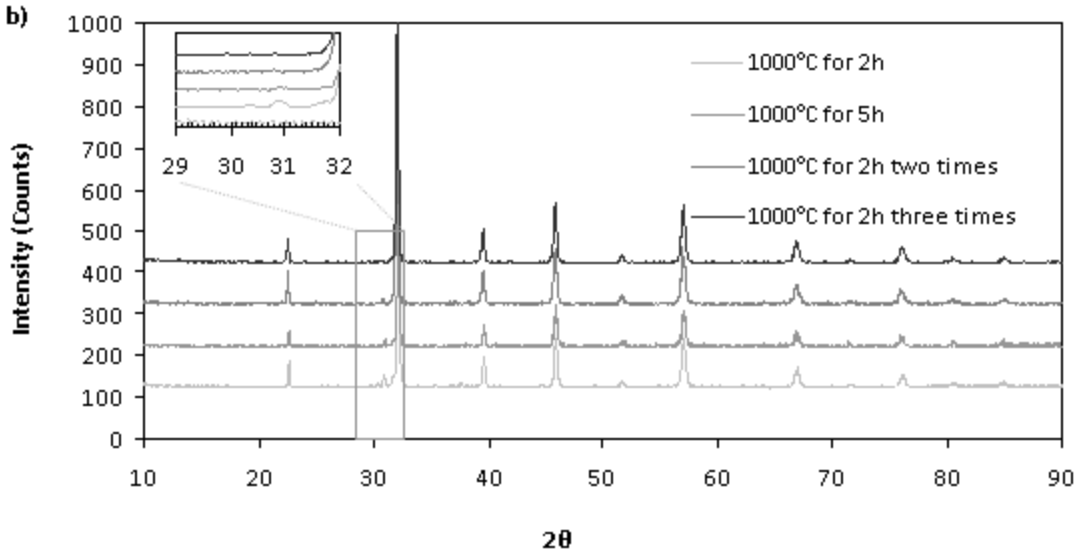


Figure 3.9. XRD spectra for $(Ba_{0.5}Sr_{0.5})_{0.92}Sm_{0.05}Co_{0.8}Fe_{0.2}O_{3-\delta}$ (BSSCF) powder after synthesis by EDTA-citrate, with a) single calcination step for 2h at 850-1000°C; and b) multiple calcinations steps for 2h at 1000°C.

The lattice parameters were calculated from the indexed peaks. The results are shown in Table 3.4. The doping of the A-site with Sm cations causes a reduction in the lattice volume, as the $Ba^{2+}$ and $Sr^{2+}$ cations (ionic radii 1.61Å and 1.44Å, respectively) are replaced by the smaller $Sm^{3+}$ cations (ionic radius 1.24Å).

| | Structure | Lattice Para-meter (Å) | Reported Literature (Å) | Lattice Volume (Å$^3$) |
|---|---|---|---|---|
| $(Ba_{0.5}Sr_{0.5})_{0.97}Co_{0.8}Fe_{0.2}O_{3-\delta}$ calcined 1000°C for 2h | Cubic Perovskite | 3.97 | 3.98 [*ICDD*] [99] 3.99 [*McIntosh*][100] 4.00 [*Li*][101] | 62.8 |
| $Ba_{0.5}Sr_{0.5}Co_{0.8}Fe_{0.2}O_{3-\delta}$ Reference (Praxair) | Cubic Perovskite | 3.97 | | 62.5 |
| $(Ba_{0.5}Sr_{0.5})_{0.92}Sm_{0.05}Co_{0.8}Fe_{0.2}O_{3-\delta}$ calcined once 1000°C for 2h | Cubic Perovskite | 3.94 | 3.98 [*Li*] | 61.1 |
| $(Ba_{0.5}Sr_{0.5})_{0.92}Sm_{0.05}Co_{0.8}Fe_{0.2}O_{3-\delta}$ two times 1000°C for 2h | Cubic Perovskite | 3.95 | | 61.5 |
| $(Ba_{0.5}Sr_{0.5})_{0.92}Sm_{0.05}Co_{0.8}Fe_{0.2}O_{3-\delta}$ three times 1000°C for 2h | Cubic Perovskite | 3.95 | | 61.5 |
| $La_{0.6}Sr_{0.4}Co_{0.2}Fe_{0.8}O_{3-\delta}$ Reference (NexTech) | Rhombo-hedral | 3.91 | 3.88 [*Tai*][102] | 58 |

Table 3.4. Structure, lattice parameter, and lattice volume for $(Ba_{0.5}Sr_{0.5})_{0.97}Co_{0.8}Fe_{0.2}O_{3-\delta}$ (BSSCF), $(Ba_{0.5}Sr_{0.5})_{0.92}Sm_{0.05}Co_{0.8}Fe_{0.2}O_{3-\delta}$, and $La_{0.6}Sr_{0.4}Co_{0.2}Fe_{0.8}O_{3-\delta}$ powders.

The morphology of the powders was determined using secondary electron microscopy (SEM), and BET surface area analysis. Commercially produced LSCF (NexTech) was included as a reference. BET surface area analysis is shown in Table 3.5. SEM micrographs are shown in Figure 3.10. Surface areas for the synthesized powders are low when compared to the commercially produced cathode powder. The micrographs confirm that this is because of the larger particle size of the lab-synthesized BSCF powder.

| | BET surface area (m$^2$/g) |
|---|---|
| $(Ba_{0.5}Sr_{0.5})_{0.97}Co_{0.8}Fe_{0.2}O_{3-\delta}$ (BSCF) | 0.37 |
| $(Ba_{0.5}Sr_{0.5})_{0.92}Sm_{0.05}Co_{0.8}Fe_{0.2}O_{3-\delta}$ (BSSCF) | 0.46 |
| $La_{0.6}Sr_{0.5}Co_{0.2}Fe_{0.8}O_{3-\delta}$ (LSCF) | 6.48 |

Table 3.5. BET surface area for lab synthesized $(Ba_{0.5}Sr_{0.5})_{0.97}Co_{0.8}Fe_{0.2}O_{3-\delta}$ (BSCF) and $(Ba_{0.5}Sr_{0.5})_{0.92}Sm_{0.05}Co_{0.8}Fe_{0.2}O_{3-\delta}$ (BSSCF); and commercially produced $La_{0.6}Sr_{0.4}Co_{0.2}Fe_{0.8}O_{3-\delta}$ (LSCF) powder.

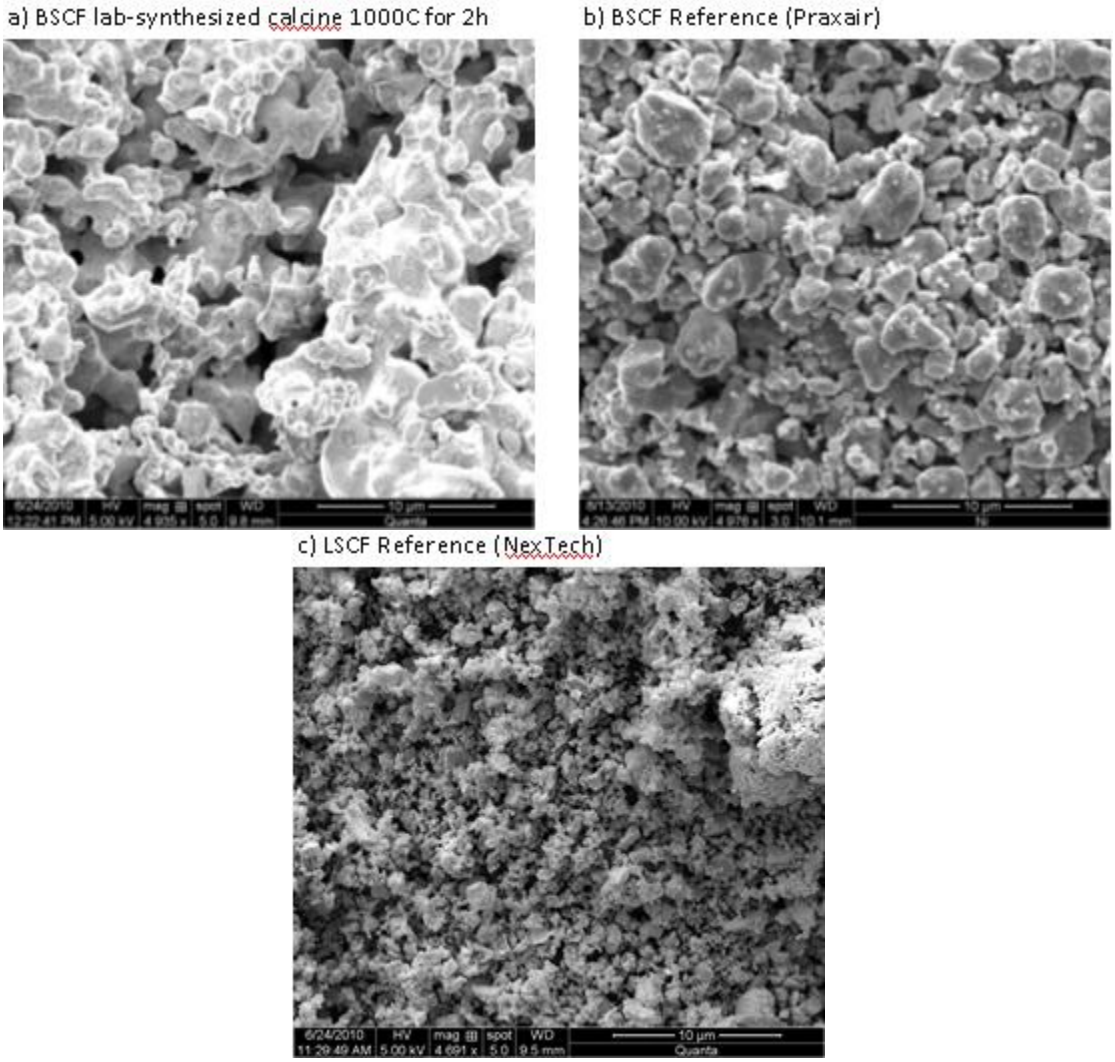


Figure 3.10. SEM micrographs of a) $(Ba_{0.5}Sr_{0.5})_{0.97}Co_{0.8}Fe_{0.2}O_{3-\delta}$ (lab-synthesized), b) $Ba_{0.5}Sr_{0.5}Co_{0.8}Fe_{0.2}O_{3-\delta}$ (Praxair), and c) $La_{0.6}Sr_{0.4}Co_{0.2}Fe_{0.8}O_{3-\delta}$ (Nextech) powder.

*BSCF Secondary Phase Formation*

The SEM micrographs of the BSCF powder show that the powder has small precipitates covering its surface. This may indicate secondary surface phase formation on the BSCF powder. To test this theory, we examined a BSCF powder sample immediately after synthesis, and then re-examined it after 24h, 100h, and 500h left in

stagnant air (inside a covered bottle). The results from this can be seen in Figure 3.11. The powder did not show evidence of any spot formation immediately after synthesis, however after only 24h in air there were small spots on the powder, and after 100h there was clear evidence of the growth of a light colored spots over the surface of the BSCF powder. The SEM taken after 500h does not show a significant increase in the size or density of the light colored spots over the sample examined after 100h. This suggests the growth of a second phase on the surface of the BSCF. We had previously observed the formation of carbonates when we attempted BSCF synthesis using GNP combustion synthesis. Of course, any combustion synthesis process occurring in air involves high temperatures and high ambient levels of $CO_2$ and CO. By using the EDTA-citrate method, we had avoided the creation of carbonates associated with combustion, but this evidence suggests secondary phase formation for BSCF after exposure only to ambient air at room temperature. The BSCF surface shows grooving after it has been calcined at 1000°C. The grooving is the result of grain boundary growth at elevated temperature, and is the result of preferred paths of migration along certain planes in the material at elevated temperatures. Interestingly, the secondary phase seems to nucleate on these grooving sites. This could be related to the geometry of the grooves, as the corners in the surface will have high surface energy associated with them, making them attractive nucleation sites. It may also be related to the preferential migration of ions along these planes, perhaps leading to a deficiency or excess of certain cations along these features.

a) BSCF after synthesis

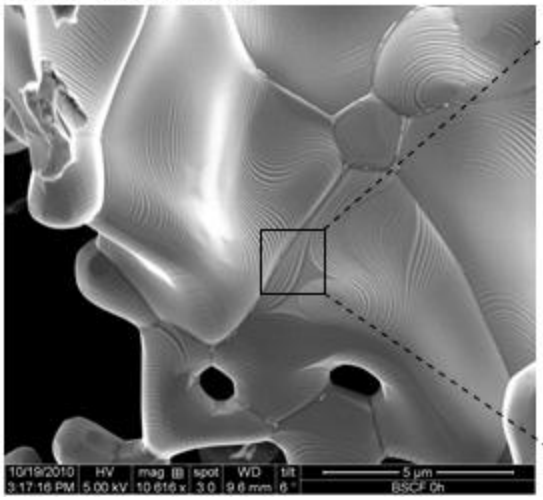


b) BSCF after synthesis (magnified)

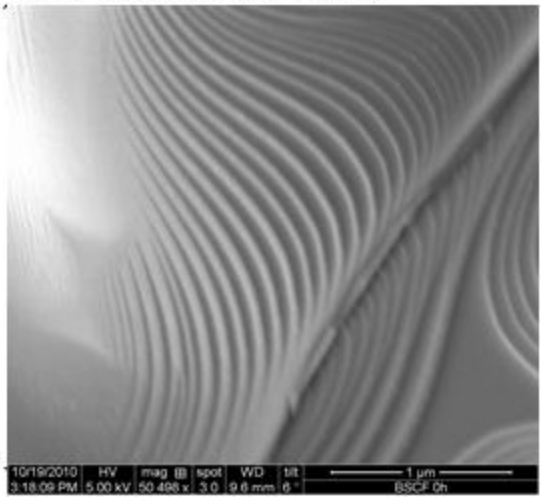


c) BSCF after 24 h in stagnant air

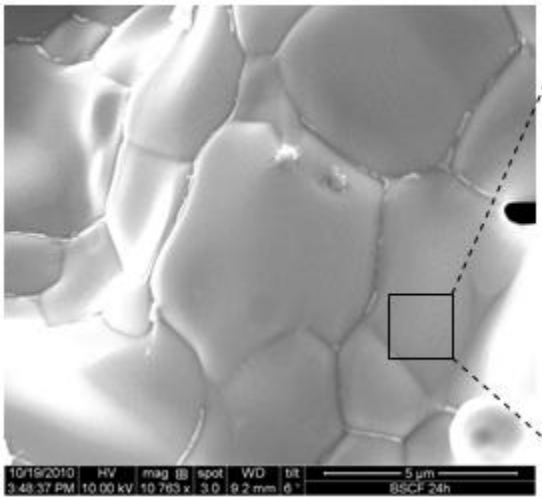


d) BSCF after 24 h in stagnant air (magnified)

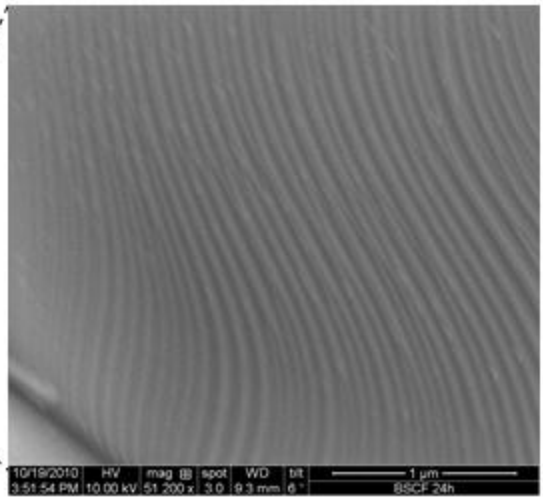


e) BSCF after 100 h in stagnant air

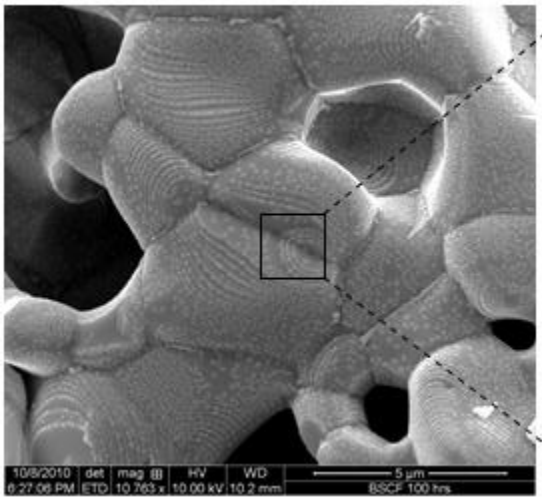


f) BSCF after 100 h in stagnant air (magnified)

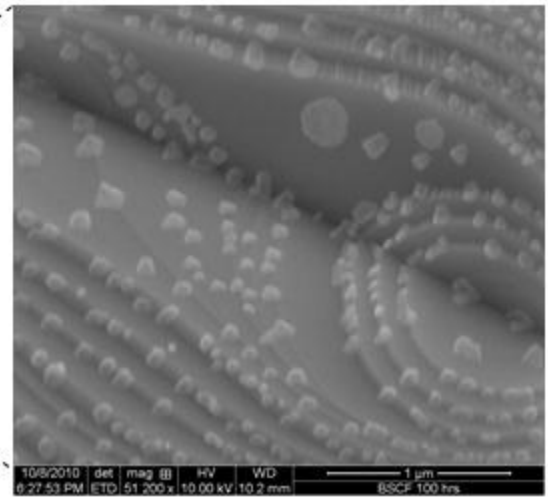

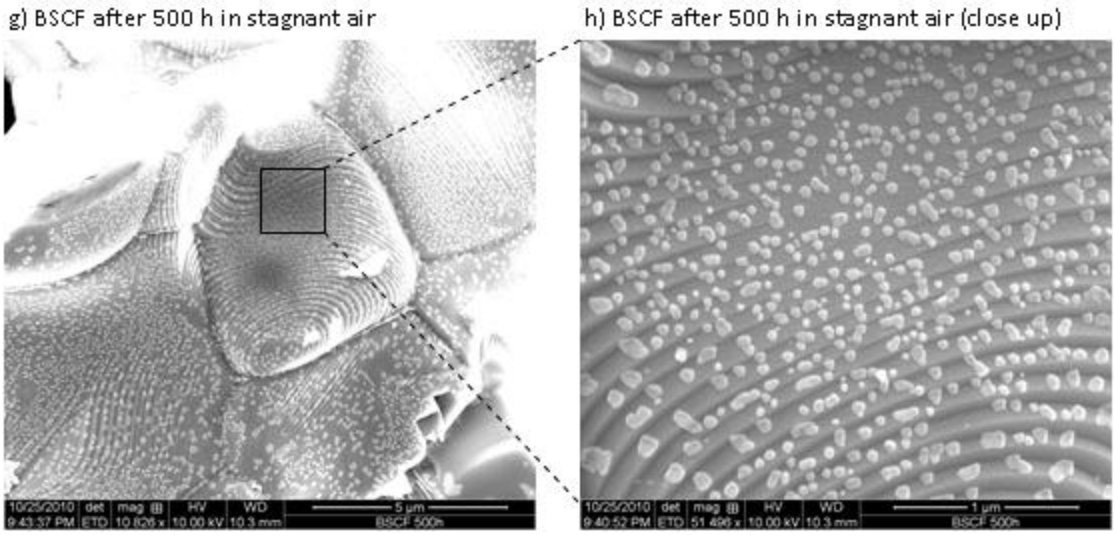


Figure 3.11. SEM micrographs of $(Ba_{0.5}Sr_{0.5})_{0.97}Co_{0.8}Fe_{0.2}O_{3-\delta}$ (BSCF) powder synthesized by EDTA-citrate; a,b) immediately after synthesis; c,d) after 24 hours in stagnant, room temperature air; e,f) after 100 hours; and g,h) after 500 hours.

XRD analysis of the examined powders was unable to detect any peaks corresponding to a secondary phase, as shown in Figure 3.12. Therefore the volume of any secondary phase present is small, below the detection limits of the XRD equipment (<1 vol%). The secondary phase must be present primarily on the surface of the cathode, not in the cathode bulk.

In order to test for phase growth under cell operating conditions, BSCF powder was exposed to elevated temperatures (600°C) for 150h in different atmospheres. Figure 3.13 shows the XRD spectra for BSCF exposed to air, humidified air, and $CO_2$ at 600°C for 150h. The powder exposed to air and humidified air did not have any clear secondary phase peaks. The powder exposed to $CO_2$ showed severe secondary phase formation, with formation of carbonates from the A-site cations ($BaCO_3$ and/or $SrCO_3$), as well as metal oxide phases ($Co_2O_3$) from the B-site cations.

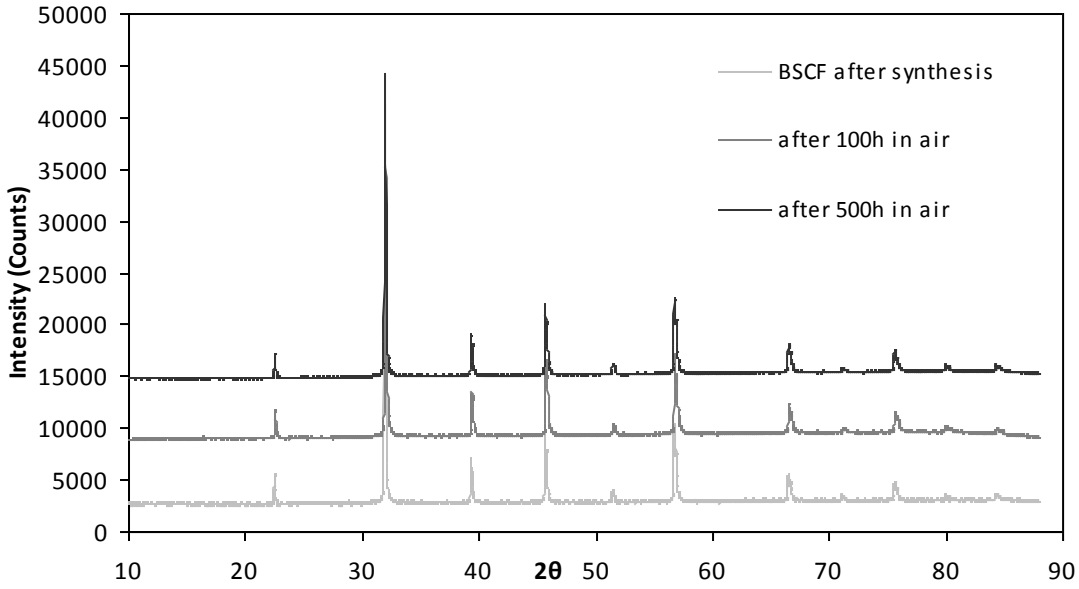


Figure 3.12. XRD spectra of $(Ba_{0.5}Sr_{0.5})_{0.97}Co_{0.8}Fe_{0.2}O_{3-\delta}$ (BSCF) powder immediately after synthesis, and after 100h and 500h in stagnant air at room temperature.

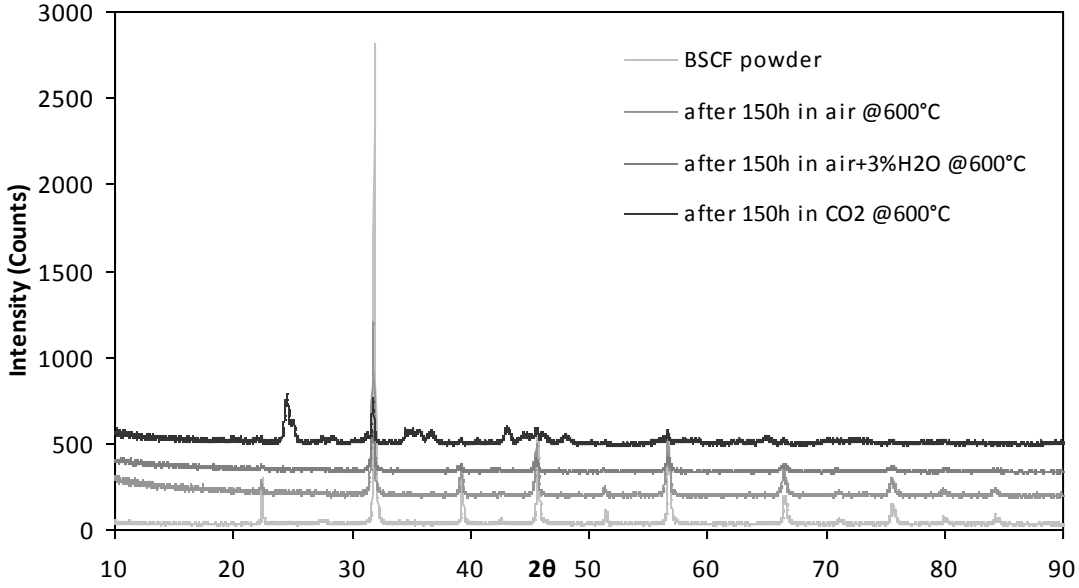


Figure 3.13. XRD spectra of $(Ba_{0.5}Sr_{0.5})_{0.97}Co_{0.8}Fe_{0.2}O_{3-\delta}$ (BSCF) powder after exposure to 600°C for 150h in flowing air, humidified air, and $CO_2$.

We also calculated the energy of formation, ΔG, of barium carbonate and barium hydroxide, and the results are seen in Figure 3.14. The formation of the barium carbonate is energetically favorable over the formation of hydroxides in this system, and the high energy of formation seems to confirm that the secondary surface phase formation would even be possible at room temperature. Since atmospheric air will generally have about 390 ppm $CO_2$, carbonate formation can occur upon exposure to ambient air. This suggests a serious challenge to the use of BSCF, as long term storage of this material may be lead to extensive surface phase formation.

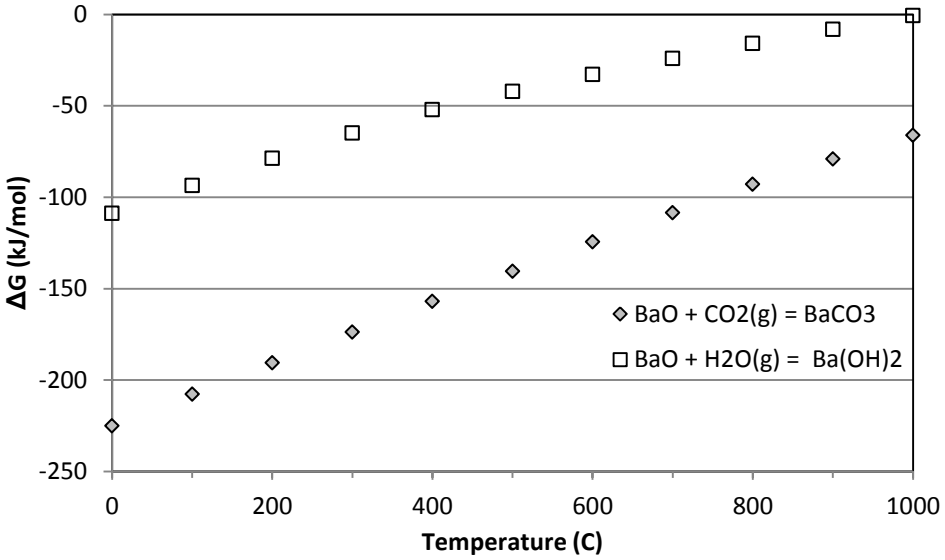


Figure 3.14. Energy of formation of barium carbonate and barium hydroxide.

### 3.4 Electrochemical Characterization of BSCF and LSCF

Thermal expansion data for LSCF, BSCF, and GDC is given in Figure 3.15. BSCF shows a sharp change in TEC around 400°C, on both heating and cooling. Thermal expansion of the material by simple lattice expansion would lead to linear behavior over the entire range, so the BSCF is undergoing some other type of change in

the lattice structure at 400°C.possibly associated with the onset of oxygen vacancy creation in the material, as described in Chapter 1.7. Since oxygen vacancy creation (oxygen loss) causes an expansion of the lattice, it is possible that this could be the cause of the change at 400°C. LSCF also shows a small change in TEC at higher temperatures, but the change is smaller and more gradual than BSCF.

Thermogravimetric analysis was used to measure the oxygen loss profile of LSCF and BSCF, and the results are shown in Figure 3.16. There is clearly a significant loss of oxygen in BSCF powder starting around 350°C, which confirms that the change in TEC is related to the formation of oxygen vacancies. LSCF powder also loses some oxygen at higher temperatures, but again the effect is smaller and more gradual than the BSCF powder.

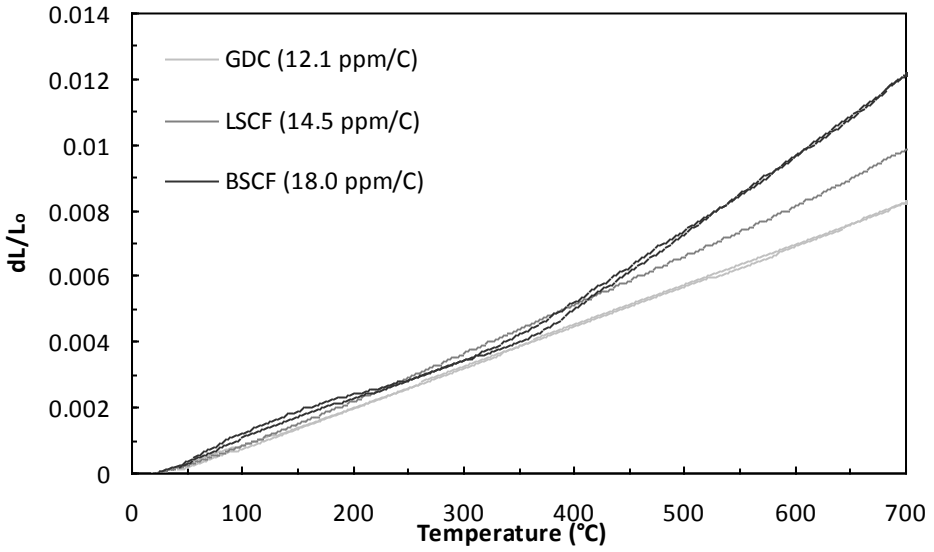


Figure 3.15. Thermal expansion data for BSCF, LSCF, and GDC from room-700°C.

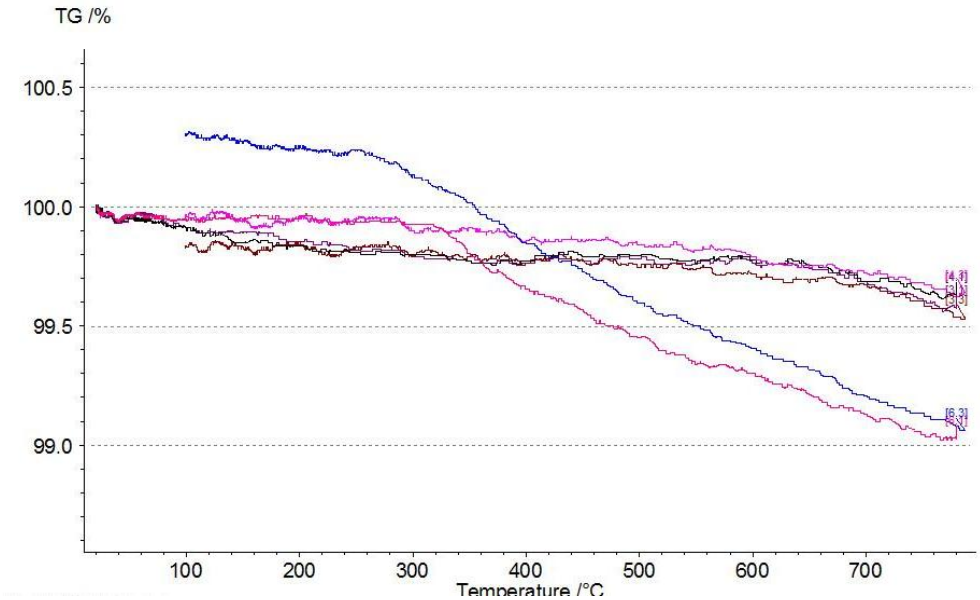


Figure 3.16. Thermogravimetric analysis of LSCF and BSCF from room-800°C.

AC impedance testing was conducted using symmetric cells, in the 500-700°C temperature range and under 1.0-0.01 atm $PO_2$. The resulting data was characterized using an equivalent circuit model, as described in Chapter 2.4. Three different processes were identified, each corresponding with an arc in the impedance spectra. At least two arcs could be identified under all conditions. The smaller of the two had a high peak frequency (~100-10,000 Hz), and the larger arc had midrange peak frequencies (~1-100Hz). A low frequency arc (~0.01-1Hz) could only be identified at higher temperatures and low $PO_2$.

*High Frequency Process*

The high frequency process was modeled as the first RC circuit. The fitted parameters for the low frequency process in the 500-700°C range and 1.0-0.01 atm $PO_2$, are given in Table 3.6, and plotted against temperature and $PO_2$ in Figure 3.17.

| BSCF | $PO_2$ (atm) | 1.0 | 0.2 | 0.04 | 0.01 |
|---|---|---|---|---|---|
| 700°C | $f_{peak}$(Hz) | 16000 | 10000 | 1300 | 850 |
| | $R_3$ ($\Omega cm^2$) | 0.03 | 0.04 | 0.085 | 0.11 |
| | $C_3$ ($Fcm^2$) | 0.0105 | 0.0109 | 0.021 | 0.022 |
| | | | | | |
| 650°C | $f_{peak}$(Hz) | 10000 | 4800 | 1200 | 720 |
| | $R_3$ ($\Omega cm^2$) | 0.053 | 0.065 | 0.15 | 0.22 |
| | $C_3$ ($Fcm^2$) | 0.0083 | 0.0112 | 0.0129 | 0.0125 |
| | | | | | |
| 600°C | $f_{peak}$(Hz) | 3500 | 1800 | 900 | 590 |
| | $R_3$ ($\Omega cm^2$) | 0.1 | 0.14 | 0.25 | 0.36 |
| | $C_3$ ($Fcm^2$) | 0.0091 | 0.0104 | 0.0094 | 0.0088 |
| | | | | | |
| 550°C | $f_{peak}$(Hz) | 1000 | 550 | 300 | 205 |
| | $R_3$ ($\Omega cm^2$) | 0.2 | 0.31 | 0.55 | 0.75 |
| | $C_3$ ($Fcm^2$) | 0.0110 | 0.0108 | 0.0093 | 0.0089 |
| | | | | | |
| 500°C | $f_{peak}$(Hz) | 450 | 225 | 85 | 53 |
| | $R_3$ ($\Omega cm^2$) | 0.48 | 0.8 | 1.35 | 1.9 |
| | $C_3$ ($Fcm^2$) | 0.0080 | 0.0078 | 0.0091 | 0.0090 |

| LSCF | $PO_2$ (atm) | 1.0 | 0.2 | 0.04 | 0.01 |
|---|---|---|---|---|---|
| 700°C | $f_{peak}$(Hz) | 2200 | 1200 | 490 | 350 |
| | $R_3$ ($\Omega cm^2$) | 0.042 | 0.06 | 0.1 | 0.13 |
| | $C_3$ ($Fcm^2$) | 0.030 | 0.032 | 0.036 | 0.035 |
| | | | | | |
| 650°C | $f_{peak}$(Hz) | 1080 | 685 | 380 | 240 |
| | $R_3$ ($\Omega cm^2$) | 0.08 | 0.11 | 0.16 | 0.22 |
| | $C_3$ ($Fcm^2$) | 0.026 | 0.026 | 0.027 | 0.027 |
| | | | | | |
| 600°C | $f_{peak}$(Hz) | 630 | 400 | 225 | 140 |
| | $R_3$ ($\Omega cm^2$) | 0.16 | 0.23 | 0.31 | 0.44 |
| | $C_3$ ($Fcm^2$) | 0.019 | 0.018 | 0.020 | 0.020 |
| | | | | | |
| 550°C | $f_{peak}$(Hz) | 490 | 320 | 170 | 100 |
| | $R_3$ ($\Omega cm^2$) | 0.36 | 0.48 | 0.63 | 0.85 |
| | $C_3$ ($Fcm^2$) | 0.0100 | 0.0102 | 0.0120 | 0.0129 |
| | | | | | |
| 500°C | $f_{peak}$(Hz) | 560 | 113 | 80 | 42 |
| | $R_3$ ($\Omega cm^2$) | 1.1 | 1.4 | 1.6 | 2 |
| | $C_3$ ($Fcm^2$) | 0.0030 | 0.0072 | 0.0080 | 0.0101 |

Table 3.6. Fitted parameters for the high frequency process in the 500-700°C range and 1.0-0.01 atm $PO_2$.

BSCF

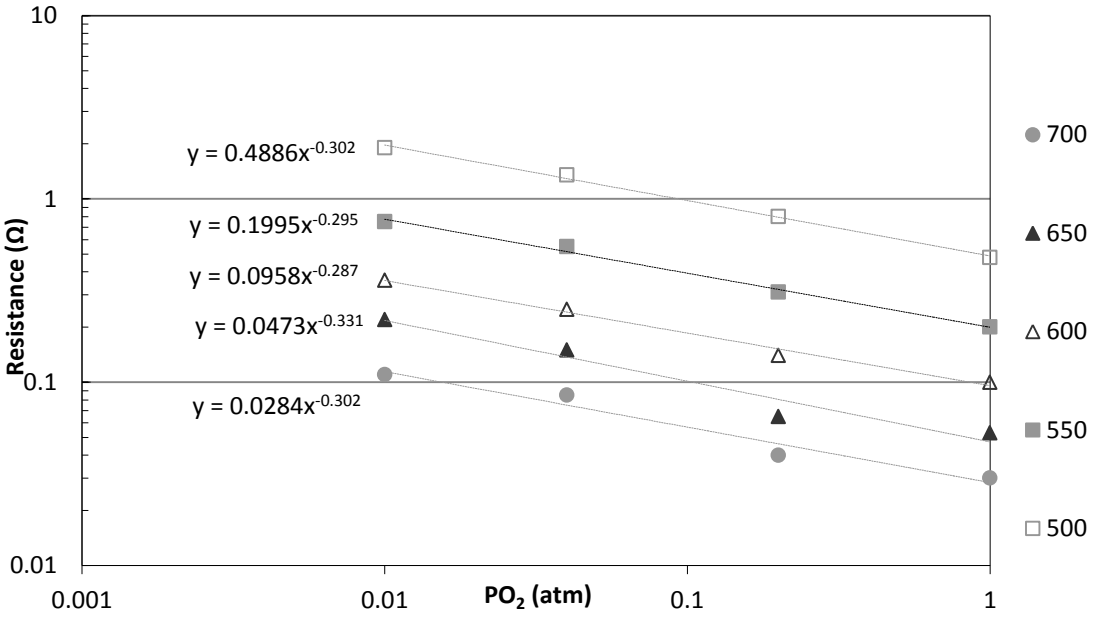
10
1
0.1
0.01
Resistance (Ω)
y = 0.4886x-0.302
y = 0.1995x-0.295
y = 0.0958x-0.287
y = 0.0473x-0.331
y = 0.0284x-0.302
0.001
0.01
0.1
1
PO2 (atm)
700
650
600
550
500

LSCF

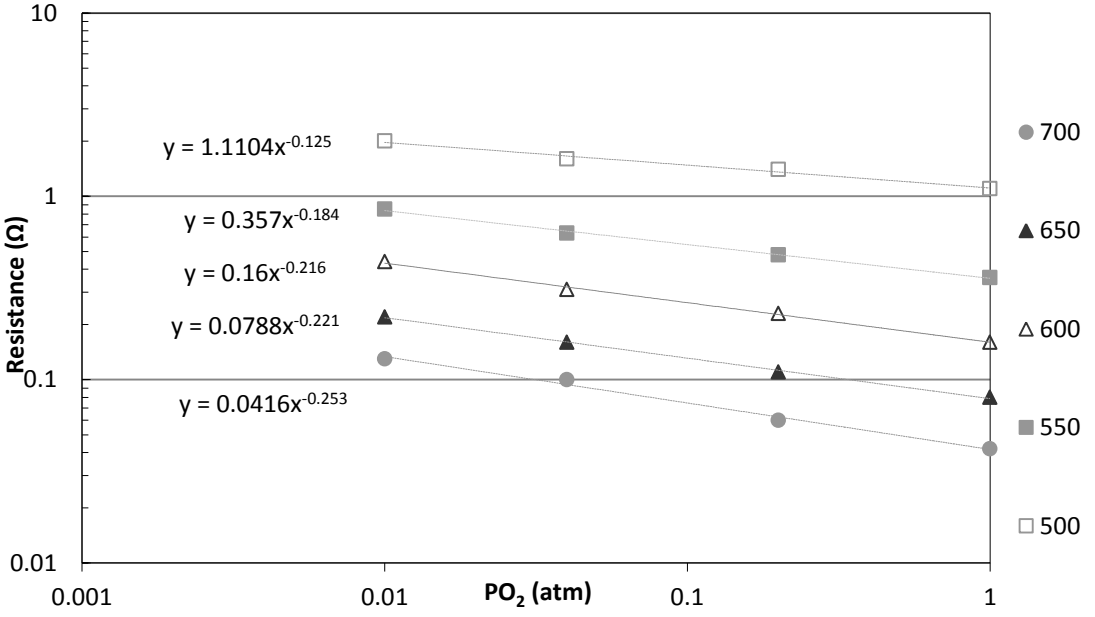
10
1
0.1
0.01
Resistance (Ω)
y = 1.1104x-0.125
y = 0.357x-0.184
y = 0.16x-0.216
y = 0.0788x-0.221
y = 0.0416x-0.253
0.001
0.01
0.1
1
PO2 (atm)
700
650
600
550
500

BSCF

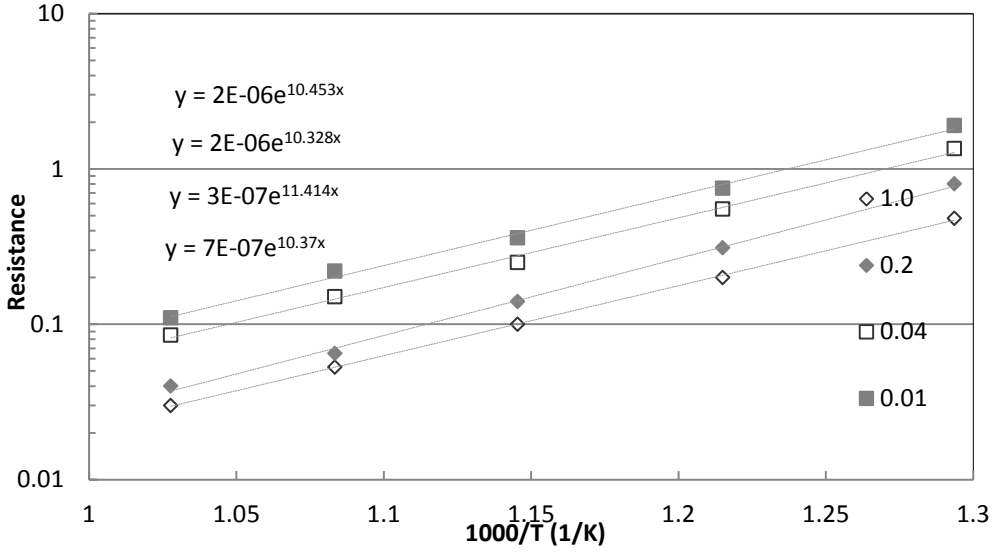
10
1
0.1
0.01
Resistance
y = 2E-06e10.453x
y = 2E-06e10.328x
y = 3E-07e11.414x
y = 7E-07e10.37x
1.0
0.2
0.04
0.01
1
1.05
1.1
1.15
1.2
1.25
1.3
1000/T (1/K)

LSCF

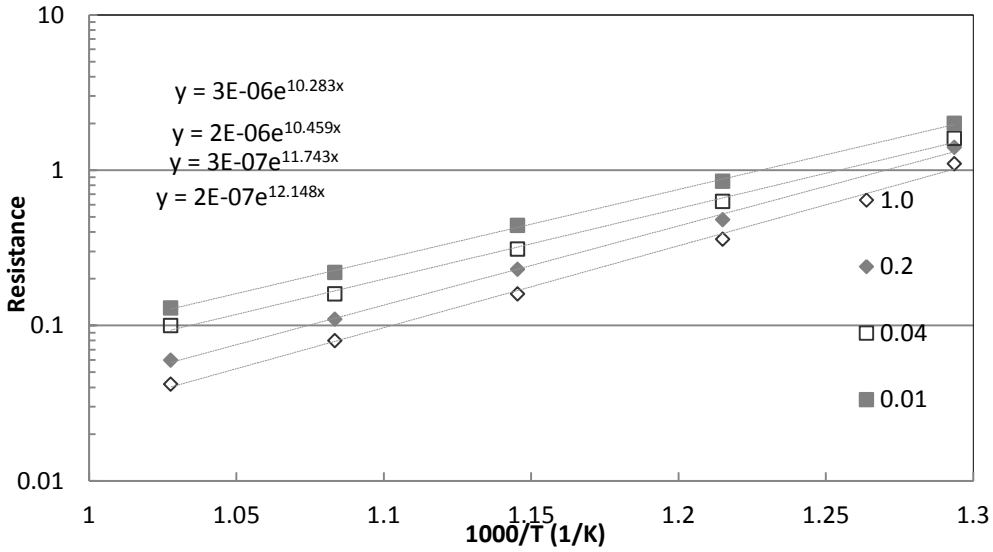
10
1
0.1
0.01
Resistance
y = 3E-06e10.283x
y = 2E-06e10.459x
y = 3E-07e11.743x
y = 2E-07e12.148x
1.0
0.2
0.04
0.01
1
1.05
1.1
1.15
1.2
1.25
1.3
1000/T (1/K)

BSCF

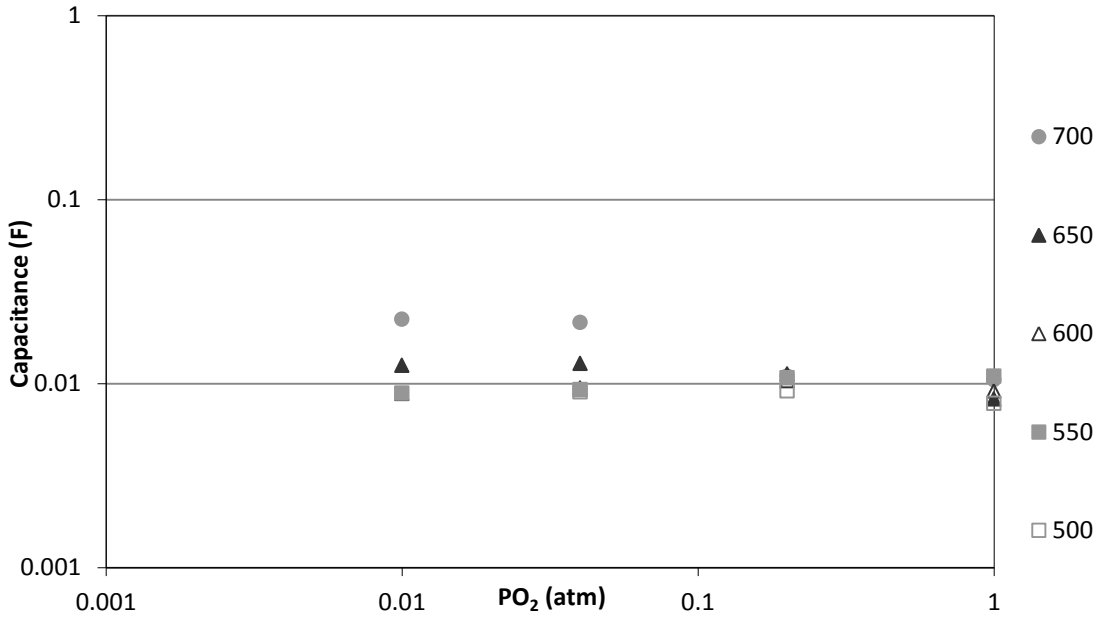


LSCF

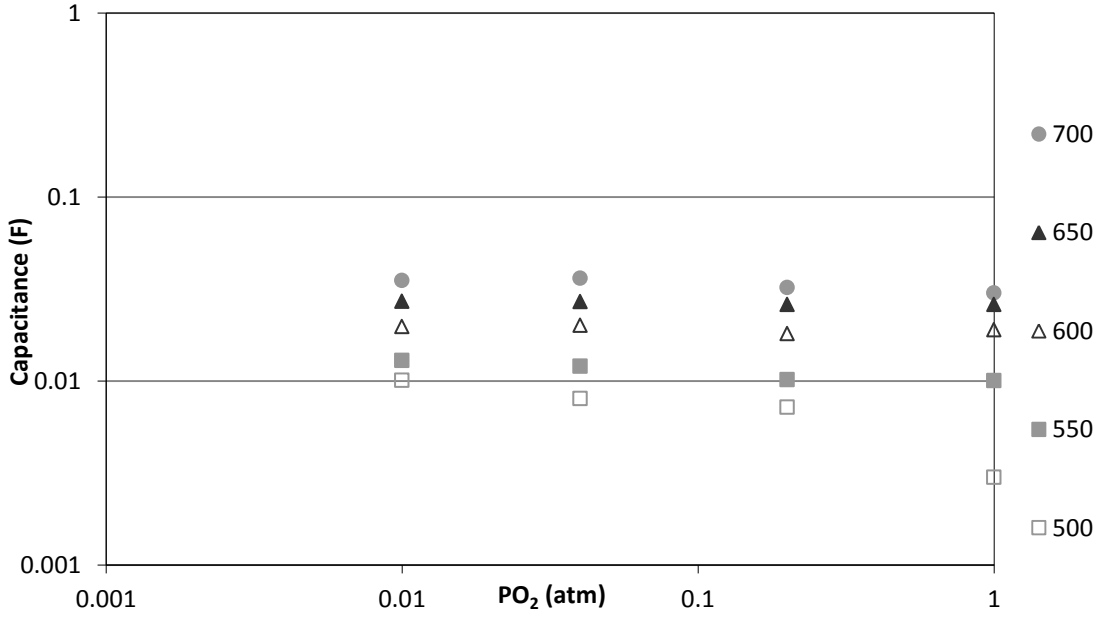


Figure 3.17. Fitted parameters for the high frequency process in the 500-700°C range and 1.0-0.01 atm $PO_2$, plotted against $PO_2$ and 1000/T.

The $PO_2$ dependence for the measured resistance was n~-0.30 for the BSCF cells, across all temperature ranges. For LSCF, the dependence changed from n~0.13 (500°C) to n~0.25 (700°C). The chemical capacitance for BSCF remained fairly constant across different temperatures and $PO_2$, while the fitted capacitance for LSCF increased with increasing temperature. Overall, the magnitude of the high frequency (100-10,000Hz) fitted resistance and capacitance was similar for both LSCF and BSCF.

This process occurs at higher frequencies than the other processes, suggesting a more rapid reaction. Since solid-solid reactions occur more quickly than solid-gas reactions, this process may represent a reaction occurring within the bulk of the cathode, or at the cathode/electrolyte interface. The activation energy for the resistance is $E_a$~86 kJ/mol for both samples.

The BSCF cell showed a similar dependence at all temperatures, and the LSCF cell had a similar dependence only at higher temperatures.

*Middle Frequency Process*

The middle frequency (1-100Hz) process was modeled as the second RC circuit. The fitted parameters for the middle frequency process in the 500-700°C range and 1.0-0.01 atm $PO_2$, are given in Table 3.7, and plotted against temperature and $PO_2$ in Figure 3.18.

| BSCF | $PO_2$ (atm) | 1 | 0.2 | 0.04 | 0.01 |
|---|---|---|---|---|---|
| 700°C | $f_{peak}$(Hz) | 119 | 103 | 40 | 12 |
| | $R_3$ ($\Omega cm^2$) | 0.13 | 0.188 | 0.25 | 0.4 |
| | $C_3$ ($Fcm^2$) | 0.075 | 0.057 | 0.084 | 0.12 |
| | | | | | |
| 650°C | $f_{peak}$(Hz) | 71 | 63 | 20 | 6.2 |
| | $R_3$ ($\Omega cm^2$) | 0.218 | 0.282 | 0.436 | 0.7 |
| | $C_3$ ($Fcm^2$) | 0.064 | 0.054 | 0.078 | 0.110 |
| | | | | | |
| 600°C | $f_{peak}$(Hz) | 35 | 30 | 10.4 | 3.6 |
| | $R_3$ ($\Omega cm^2$) | 0.355 | 0.5 | 0.745 | 1.24 |
| | $C_3$ ($Fcm^2$) | 0.065 | 0.051 | 0.072 | 0.091 |
| | | | | | |
| 550°C | $f_{peak}$(Hz) | 12.6 | 6.8 | 1.75 | 0.57 |
| | $R_3$ ($\Omega cm^2$) | 0.78 | 1.29 | 2.59 | 4.65 |
| | $C_3$ ($Fcm^2$) | 0.060 | 0.056 | 0.072 | 0.088 |
| | | | | | |
| 500°C | $f_{peak}$(Hz) | 2.1 | 0.97 | 0.22 | 0.085 |
| | $R_3$ ($\Omega cm^2$) | 2.85 | 4.85 | 10.1 | 16.8 |
| | $C_3$ ($Fcm^2$) | 0.058 | 0.058 | 0.079 | 0.092 |

| LSCF | $PO_2$ (atm) | 1 | 0.2 | 0.04 | 0.01 |
|---|---|---|---|---|---|
| 700°C | $f_{peak}$(Hz) | 171 | 60 | 17.1 | 6.25 |
| | $R_3$ ($\Omega cm^2$) | 0.235 | 0.28 | 0.325 | 0.38 |
| | $C_3$ ($Fcm^2$) | 0.016 | 0.031 | 0.073 | 0.140 |
| | | | | | |
| 650°C | $f_{peak}$(Hz) | 116 | 41.5 | 13.4 | 4.6 |
| | $R_3$ ($\Omega cm^2$) | 0.54 | 0.65 | 0.76 | 0.85 |
| | $C_3$ ($Fcm^2$) | 0.0095 | 0.018 | 0.038 | 0.080 |
| | | | | | |
| 600°C | $f_{peak}$(Hz) | 62 | 20 | 8 | 3 |
| | $R_3$ ($\Omega cm^2$) | 1.51 | 1.86 | 2.12 | 2.32 |
| | $C_3$ ($Fcm^2$) | 0.0056 | 0.0112 | 0.0205 | 0.041 |
| | | | | | |
| 550°C | $f_{peak}$(Hz) | 30 | 11 | 4.28 | 1.55 |
| | $R_3$ ($\Omega cm^2$) | 4.43 | 5.58 | 6.53 | 7.7 |
| | $C_3$ ($Fcm^2$) | 0.0034 | 0.0060 | 0.011 | 0.021 |
| | | | | | |
| 500°C | $f_{peak}$(Hz) | 13.4 | 4.5 | 1.7 | 0.69 |
| | $R_3$ ($\Omega cm^2$) | 14.4 | 19.8 | 25 | 29.4 |
| | $C_3$ ($Fcm^2$) | 0.0020 | 0.0035 | 0.0060 | 0.0105 |

Table 3.7. Fitted parameters for the middle frequency process in the 500-700°C range and 1.0-0.01 atm $PO_2$.

BSCF

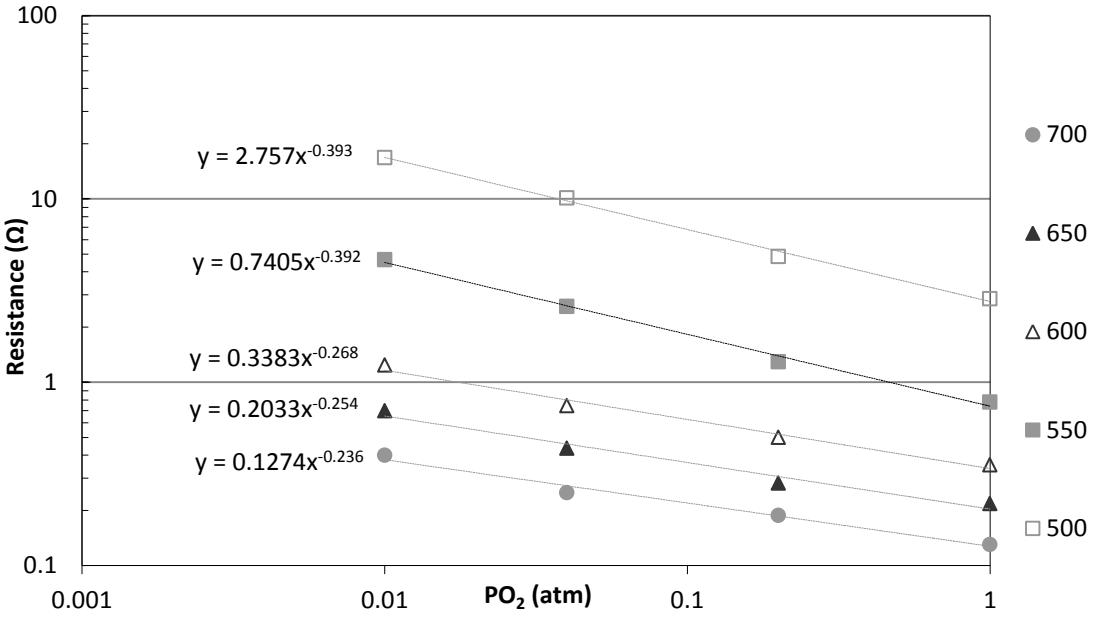
100
10
1
0.1
Resistance (Ω)
y = 2.757x-0.393
y = 0.7405x-0.392
y = 0.3383x-0.268
y = 0.2033x-0.254
y = 0.1274x-0.236
0.001
0.01
0.1
1
PO2 (atm)
700
650
600
550
500

LSCF

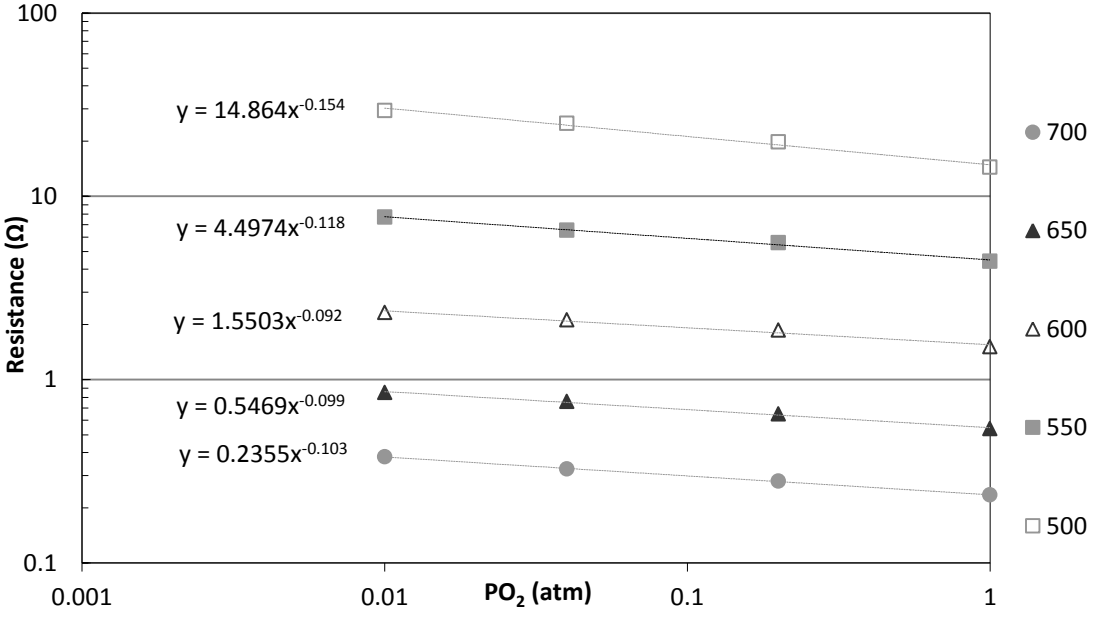
100
10
1
0.1
Resistance (Ω)
y = 14.864x-0.154
y = 4.4974x-0.118
y = 1.5503x-0.092
y = 0.5469x-0.099
y = 0.2355x-0.103
0.001
0.01
0.1
1
PO2 (atm)
700
650
600
550
500

BSCF

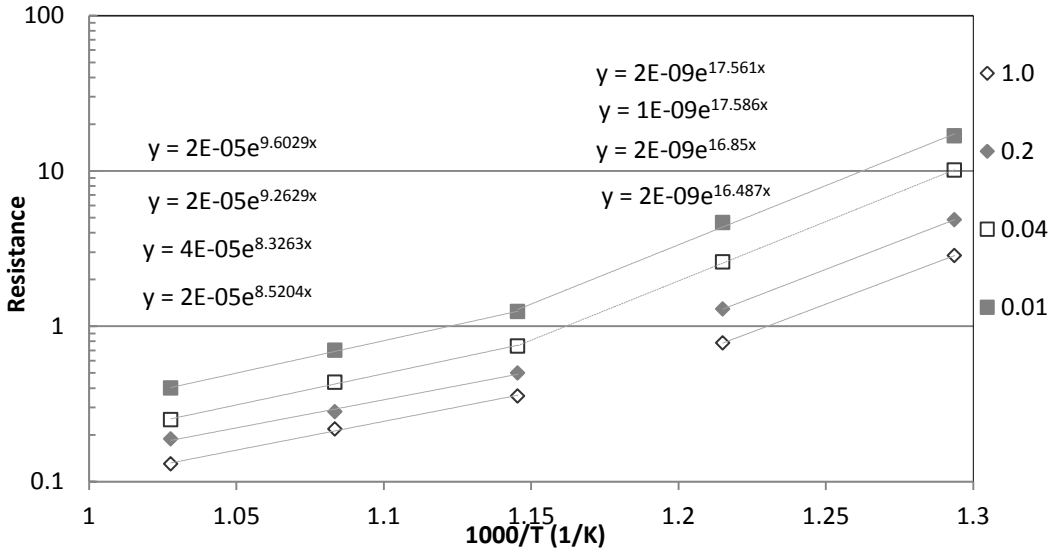
100
10
1
0.1
Resistance
1
1.05
1.1
1.15
1.2
1.25
1.3
1000/T (1/K)
y = 2E-05e9.6029x
y = 2E-05e9.2629x
y = 4E-05e8.3263x
y = 2E-05e8.5204x
y = 2E-09e17.561x
y = 1E-09e17.586x
y = 2E-09e16.85x
y = 2E-09e16.487x
1.0
0.2
0.04
0.01

LSCF

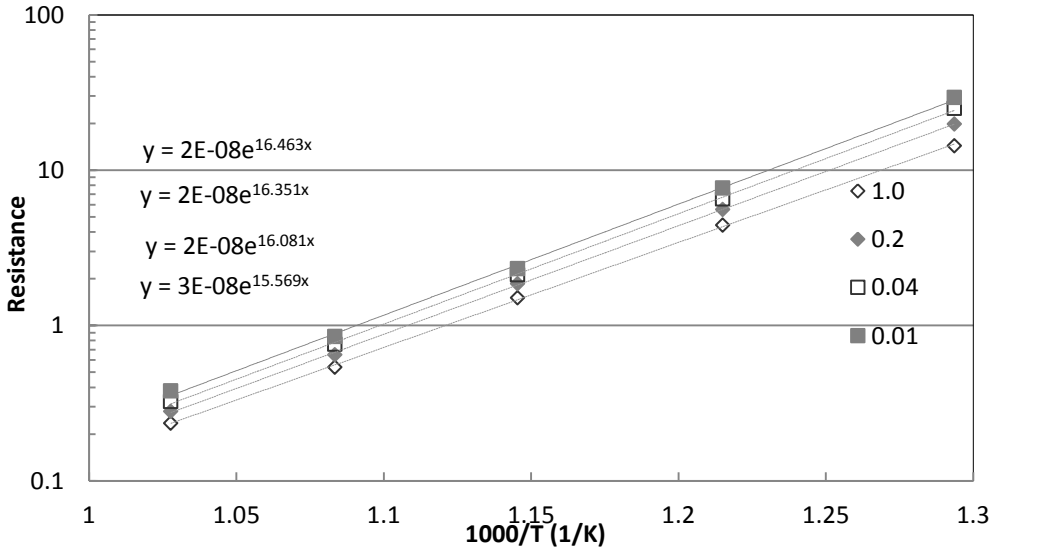
100
10
1
0.1
Resistance
1
1.05
1.1
1.15
1.2
1.25
1.3
1000/T (1/K)
y = 2E-08e16.463x
y = 2E-08e16.351x
y = 2E-08e16.081x
y = 3E-08e15.569x
1.0
0.2
0.04
0.01

BSCF

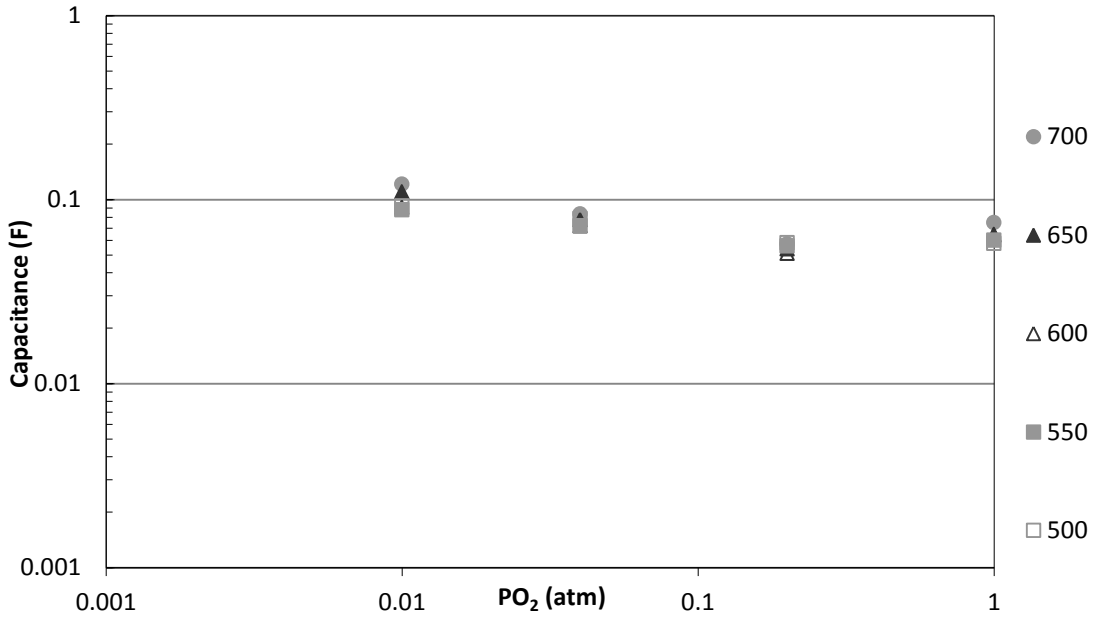


LSCF

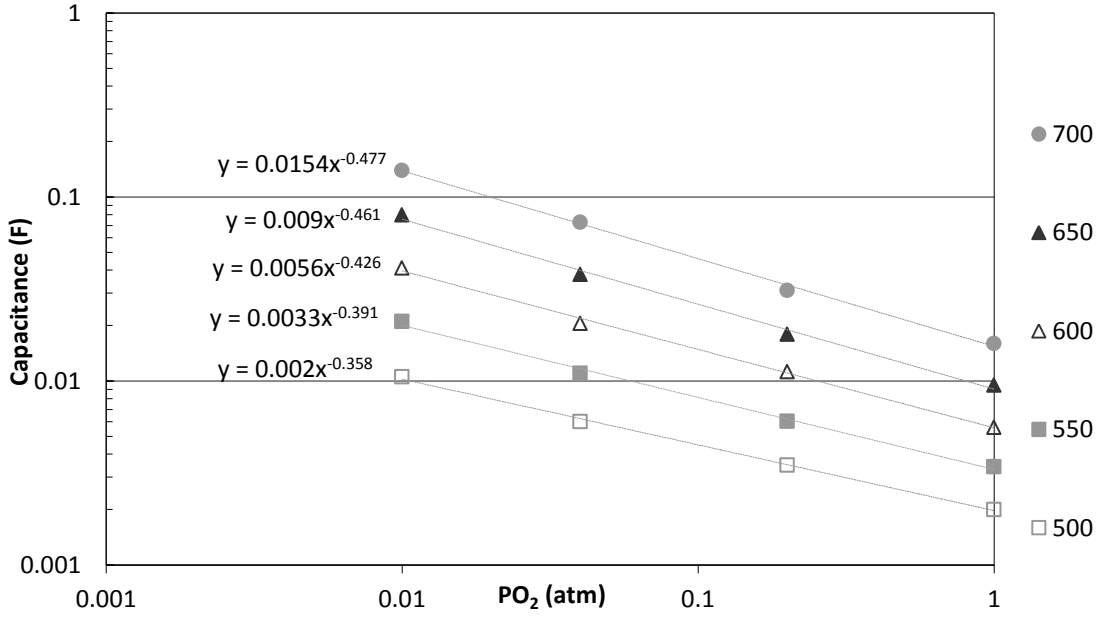


Figure 3.18. Fitted parameters for the middle frequency process in the 500-700°C range and 1.0-0.01 atm $PO_2$, plotted against $PO_2$ and 1000/T.

The $PO_2$ dependence for the middle frequency process for LSCF is fairly constant at n~0.10, and the activation energy is fairly constant at Ea~130-137 kJ/mol. For the BSCF sample, two distinct regimes are visible. Below 600°C, the $PO_2$ dependence is n~0.39, with Ea~137-146 kJ/mol. As discussed in Chapter 2, a PO2 dependence of n=0.5 suggests partial reduction of the oxygen ion, possibly followed by surface diffusion. At 600°C and above, the $PO_2$ dependence is n~0.25, with Ea~70-80 kJ/mol. As discussed in Chapter 1.8, this is consistent with a complete reduction of the oxygen ion and direct incorporation into the bulk of the cathode, followed by bulk diffusion, which would give a dependence of n=0.25. Therefore we can identify a transition of the dominant reaction mechanism of the cathode occurring at 600°C.

*Low Frequency Process*

The low frequency (0.01-1 Hz) process was modeled as the third RC circuit in our equivalent circuit model. The fitted parameters for the low frequency process in the 500-700°C range and 1.0-0.01 atm $PO_2$, are given in Table 3.8. The various fitted parameters are also plotted against temperature and $PO_2$ in Figure 3.19.

| BSCF | $PO_2$ (atm) | 0.2 | 0.04 | 0.01 |
|---|---|---|---|---|
| 700°C | $f_{peak}$(Hz) | 1.4 | 0.28 | 0.0725 |
| | $R_3$ ($\Omega cm^2$) | 0.022 | 0.112 | 0.43 |
| | $C_3$ ($Fcm^2$) | 6.42 | 5.37 | 4.72 |
| | | | | |
| 650°C | $f_{peak}$(Hz) | 2.6 | 0.35 | 0.083 |
| | $R_3$ ($\Omega cm^2$) | 0.02 | 0.09 | 0.4 |
| | $C_3$ ($Fcm^2$) | 4.05 | 5.47 | 4.49 |
| | | | | |
| 600°C | $f_{peak}$(Hz) | | 0.52 | 0.1 |
| | $R_3$ ($\Omega cm^2$) | | 0.055 | 0.25 |
| | $C_3$ ($Fcm^2$) | | 6.26 | 6.08 |

| LSCF | $PO_2$ (atm) | 0.2 | 0.04 | 0.01 |
|---|---|---|---|---|
| 700°C | $f_{peak}$(Hz) | 1.68 | 0.365 | 0.086 |
| | $R_3$ ($\Omega cm^2$) | 0.020 | 0.148 | 0.58 |
| | $C_3$ ($Fcm^2$) | 6.0 | 3.2 | 3.0 |
| | | | | |
| 650°C | $f_{peak}$(Hz) | | 0.477 | 0.115 |
| | $R_3$ ($\Omega cm^2$) | | 0.12 | 0.56 |
| | $C_3$ ($Fcm^2$) | | 3.1 | 2.4 |
| | | | | |
| 600°C | $f_{peak}$(Hz) | | 0.14 | 0.013 |
| | $R_3$ ($\Omega cm^2$) | | 0.38 | 4.5 |
| | $C_3$ ($Fcm^2$) | | 3.0 | 2.1 |

Table 3.8. Fitted parameters for the low frequency process in the 500-700°C range and 1.0-0.01 atm $PO_2$.

BSCF

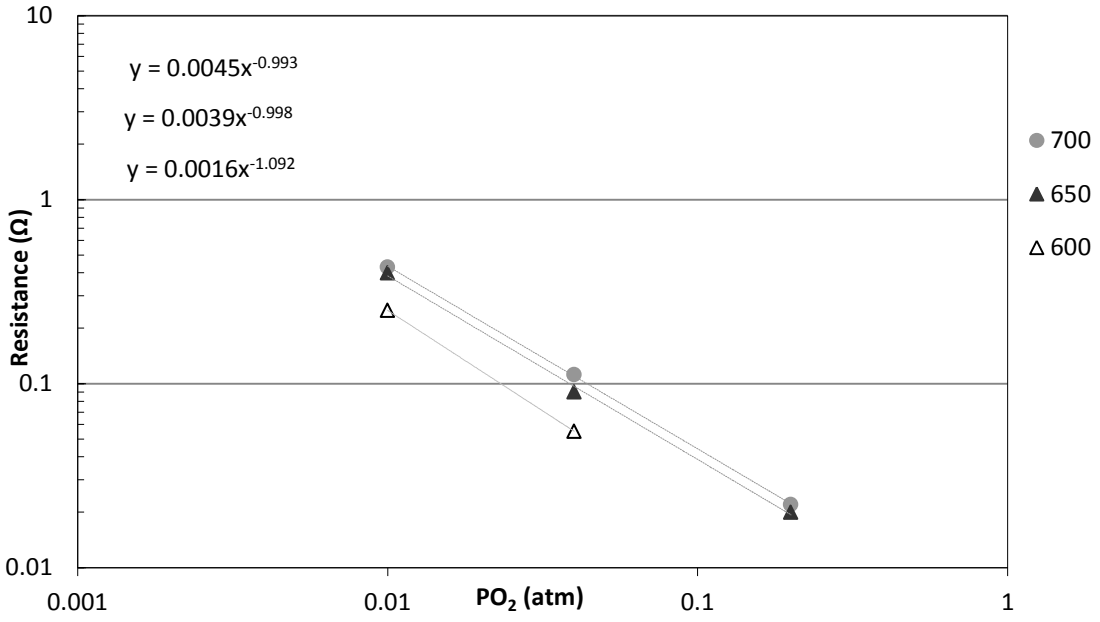
y = 0.0045x-0.993
y = 0.0039x-0.998
y = 0.0016x-1.092
Resistance (Ω)
10
1
0.1
0.01
0.001
0.01
0.1
1
PO2 (atm)
700
650
600

LSCF

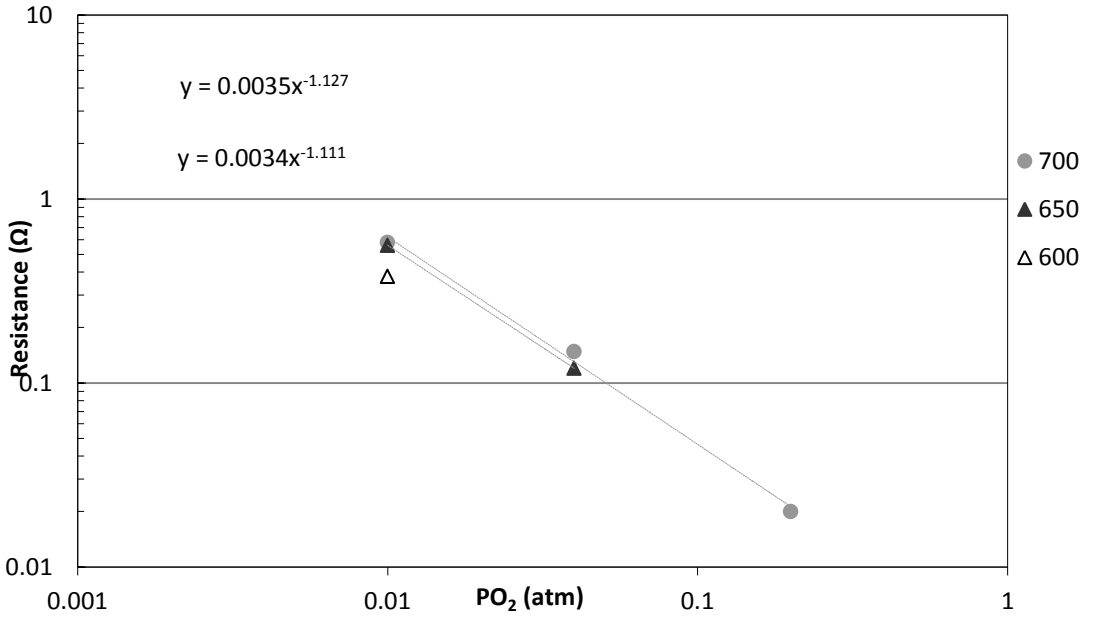
y = 0.0035x-1.127
y = 0.0034x-1.111
Resistance (Ω)
10
1
0.1
0.01
0.001
0.01
0.1
1
PO2 (atm)
700
650
600

BSCF

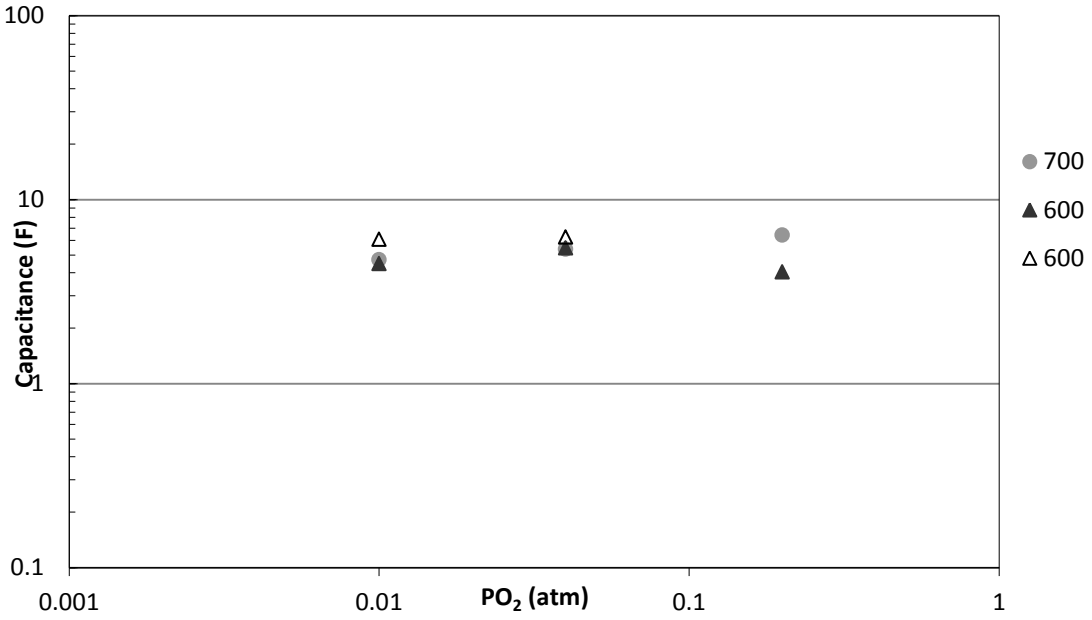


LSCF

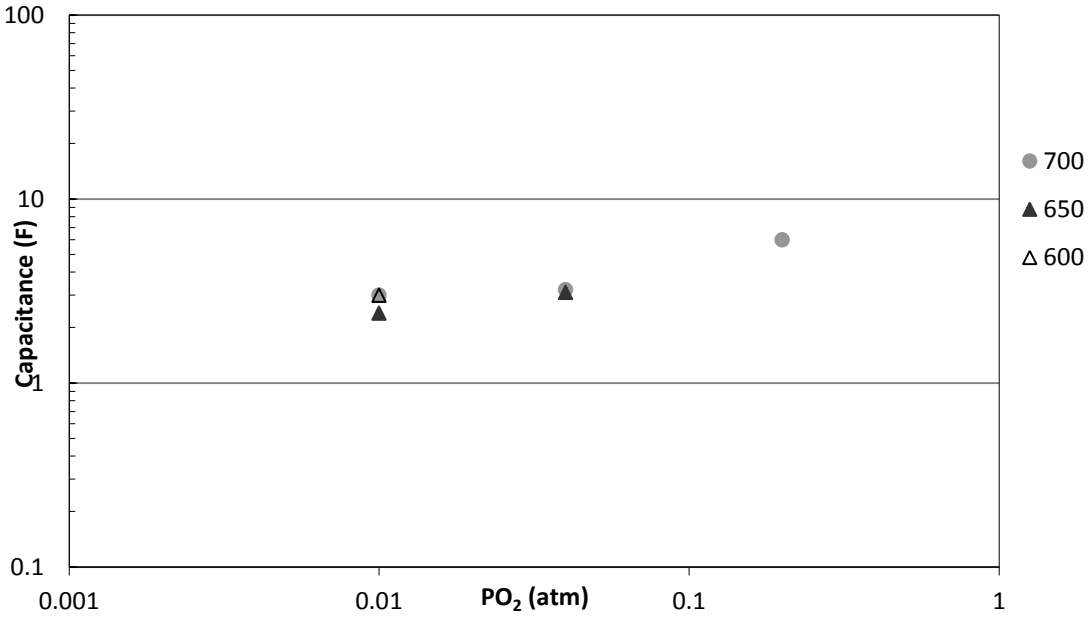


Figure 3.19. Fitted parameters for the low frequency process in the 500-700°C range and 1.0-0.01 atm $PO_2$, plotted against $PO_2$.

The $PO_2$ dependence for the measured resistance was n~1 for both the LSCF and the BSCF cells, with minimal dependence on temperature. A $PO_2^n$ dependence of n=-1 has also been suggested for gas diffusion processes (see Ch. 1.8). The chemical capacitance was very large compared to the other fitted capacitors (4-6F$cm^2$), and showed little variation with $PO_2$ or temperature. The process is dominant at lower frequencies, consistent with longer-time scale fluid effects. The effect of the process is small enough to be neglected in the model at lower temperatures, and higher $PO_2$.

*Interpretation of the Proposed Model for BSCF*

Using the models of $PO_2$ dependence outlined in Chapter 1.8, it is possible to interpret the components of the equivalent circuit model in terms of the processes occurring in the cathode. A table showing the calculated properties from the model is shown in Table 3.9, and the proposed equivalent circuit model is shown in Figure 3.20. Each of the three RC circuits represents a different process.

| | **R ($\Omega$*$cm^2$)** | **$PO_2^n$ dependence of R** | **$E_a$ of R (kJ/mol)** | **Pseudo-capac-itance** | **Proposed Process** |
|---|---|---|---|---|---|
| **High Freq. Process** | 0.03-1.9 | n~0.3 | 85-95 | 0.008-0.022 | *Charge Transfer* |
| **Middle Freq. Process** | 0.13-17 | n~0.4 (below 600°C)<br><br>n~0.25 (600°C and above) | 137-146 (below 600°C)<br><br>70-80 (above 600°C) | 0.06-0.12 | *Surface Exchange*<br><br>Partial reduction and surface diffusion below 600°C; Incorporation and bulk diffusion above 600°C |
| **Low Freq. Process** | 0.02-0.4 (only above 600C) | n~1 | no temperature dependence | 4-6 | *Gas Diffusion* |

Table 3.9. Properties of the three modeled processes for the BSCF cathode, and the proposed steps they represent.

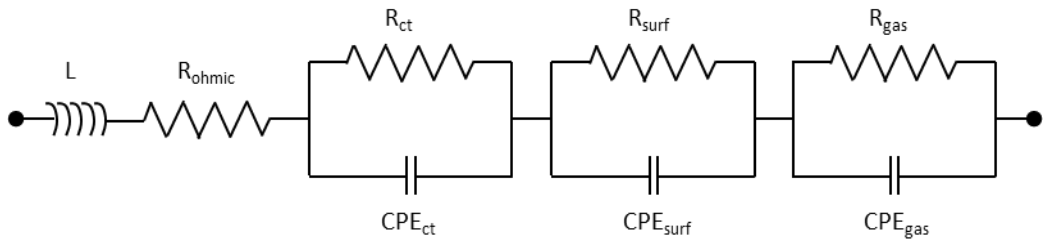


Figure 3.20. Proposed equivalent circuit model for LSCF and BSCF symmetric cells operating in 1.0-0.01 atm $PO_2$, at 500-700°C.

*Charge Transfer Process (High Frequency)*

The charge transfer process occurs first. This process represents the onset of the $O^{2-}$ ionic flow from cathode to electrolyte. The measured resistance is the resistance to this ionic transfer. The charge transfer reaction itself occurs at the cathode-electrolyte interface, but $R_{ct}$ represents all of the resistance associated with the ionic transfer from the cathode to electrolyte. As discussed in the previous section, $R_{ct}$ for BSCF has a $PO_2$ dependence of n=0.30 for all temperatures, which is consistent with a charge transfer process. For LSCF, the partial pressure dependence is only ~0.25 at 700°C, suggesting that the behavior of BSCF is similar to that of LSCF at higher temperatures (700°C and above). Both cells show $E_a$~86kJ/mol, suggesting a shared rate-limiting mechanism.

The capacitance of the charge transfer constant phase element, $CPE_{ct}$ represents the amount of electrical energy needed to activate this ionic flow. The BSCF cell shows a capacitance which is essentially constant with temperature in the measured range. This behavior is different from the LSCF cell, which shows stronger temperature dependence. The difference may be related to the way that BSCF conducts and stores charge. As discussed in Chapter 1, in this temperature range cobaltites can conduct electrical charge

by using a conduction band on the Co cations, whereas ferrites are semi-conducting, moving charge by local changes in valence of the Fe cations. This may cause the capacitance to have strong temperature dependence for compounds with high Fe content (LSCF), and weak temperature dependence for compounds with high Co content (BSCF).

*Surface Exchange Process (Mid Frequency)*

After the charge transfer reaction has come to equilibrium, an ionic flow has been set up from the cathode to the electrolyte. This ionic flow is what drives the next process: the surface exchange process. As $O^{2-}$ ions begin to leave the cathode lattice following the onset of charge transfer, new $O^{2-}$ ions are formed by the reduction of gaseous oxygen at the surface of the cathode. The resistance to this process is embodied by the surface exchange resistance, $R_{surf}$. It represents the resistance encountered during the reduction of gaseous oxygen on the surface of the cathode. For BSCF, the $PO_2$ dependence for $R_{surf}$ processes is n=0.39 below 600°C, and n~0.25 at 600°C and above. As discussed in Chapter 1.8, a $PO_2$ dependence of n=0.25 is consistent with the direct absorption and transfer of the gaseous oxygen into the bulk of the cathode, a process involving two $e^-$. A $PO_2$ dependence of 0.5 is consistent with a partial reduction process involving one $e^-$, suggesting a partial reduction at the surface, followed by surface diffusion. In addition to the transition in $PO_2$ dependence at 600°C, there was also a change in the activation energy of the resistance. Below 600°C, the surface exchange process had an activation energy of $E_a$~136-146 kJ/mol, while above 600°C, $E_a$~70-80 kJ/mol. As discussed in Chapter 1, a lower activation energy is observed for the surface exchange coefficient (k) than for the diffusion coefficient (D*), and the measured values are consistent with the $E_a$

values for diffusion and surface exchange coefficients discussed in Chapter 1. This suggests that the BSCF cathode is limited by diffusion at lower temperatures, and limited by surface exchange processes at lower temperatures. This information serves to explain the significance of the 600°C transition point. Above 600°C, the reaction mechanism involves oxygen reduction and incorporation directly into a vacancy in the cathode, followed by bulk diffusion to the cathode-electrolyte interface. At lower temperatures, bulk diffusion is not energetically favorable, and so the reaction occurs via partial reduction and surface diffusion. There is a transition at 600°C, which represents the point at which ionic diffusion is sufficient for the bulk reaction pathway to become the dominant pathway. The surface reaction pathway will not shut down above 600°C, but the proportion of the ionic flow through this pathway becomes smaller as the bulk pathway becomes increasingly more active.

The capacitance represents the amount of energy needed to activate this ion creation process. The measured capacitance is quite large (0.01-0.1Fcm$^2$), and must represent more than simply electrical energy storage. If charge transfer is a flow of $O^{2-}$ ions occurring in response to the applied voltage, then the oxygen ion creation process may be a response to a buildup of vacancies in the cathode caused by the transfer of the $O^{2-}$ ions. In this way, the cathode essentially can be thought of as a reservoir of potential oxygen ions. As charge transfer proceeds at the cathode-electrolyte interface, $O^{2-}$ ions are first taken from the surrounding lattice sites in the cathode. After a certain point, enough vacancies have been created that it is energetically favorable for gaseous oxygen to reduce and fill the available vacancies, generating the measured current.

*Gas Diffusion Process (Low Frequency)*

After the onset of the surface oxygen reduction reaction, the cell is drawing $O_2$ molecules from the surrounding gas. Initially there is sufficient localized $O_2$ for the reaction, but after the localized gas has been depleted, $O_2$ must diffuse in from farther away. The resistance to this gas diffusion is $R_{gas}$. The capacitance of $CPE_{gas}$ represents the amount of charge transferred (via $O^{2-}$ ions) before enough $O_2$ molecules have been depleted to set up the pressure gradient. As discussed in the previous section, a $PO_2$ dependence of n~1 was found, which is consistent with a gas diffusion process. While gas diffusion does not involve any exchange of electrons, it will affect the measured electrical current when it is the limiting process. The resistance was similar for both the LSCF and BSCF samples, and changed very little with temperature. As a result of the strong $PO_2$ dependence, this resistance becomes more important at lower $PO_2$.

# Chapter 4

# Conclusions

*Synthesis*

- The EDTA-citrate technique was identified for the synthesis of BSCF, and BSCF synthesis procedures were developed for our laboratory.
- Multiple pathways to metal-nitrate characterization were explored. ICP testing proved inconclusive due to the high levels of dilution required to reach the detection limits of the equipment. Heating the metal-nitrates to form oxides was found to be effective for Fe and Co, but not Ba due to reaction with the alumina crucible. EDTA titration was found to be effective for Ba and Sr.
- Glycine nitrate synthesis of BSCF leads to the formation of secondary carbonate phases, due to the high temperature combustion process.
- EDTA-citrate synthesis allows for the synthesis of pure-phase BSCF, as it does not require any high temperature combustion steps. EDTA-citrate is the preferred method for synthesizing BSCF.
- BSSCF synthesis results in secondary SmO phase formation, which can be minimized through repeated grinding and re-calcination steps.
- Exposure to ambient air at room temperature leads to secondary surface phase formation in BSCF powder after as little as 100h. The volume of the phase is small (<1vol%), but the surface phase may block available reaction sites.
- The secondary phase nucleates around the grooving sites in the material.
- The secondary phase formation was attributed to the formation of carbonates upon exposure to $CO_2$ in the ambient air; this suggests serious challenges for the long term storage of BSCF powder.

*Properties*

- Particle size and surface area analysis showed lab synthesized BSCF (and our commercially produced BSCF) has larger particles (1-4μm) than commercial LSCF powder (>1μm); BSCF synthesis by EDTA-citrate may not be optimal for high surface area powders.
- The TEC for BSCF shows a sharp change in slope at ~400°C. A change in weight is also observed for BSCF at 400°C using TGA. Taken together, this suggests that loss of oxygen lattice begins around 400°C. For LSCF, oxygen lattice loss was found to begin around 650-700°C.
- LSCF-GDC composites allow for a reduction in thermal expansion coefficient mismatch for between the cathode and the GDC electrolyte (16.7 ppm/K for LSCF, 15.6 ppm/K for LSCF-GDC 50-50, and 12.6 ppm/K for GDC).

*Electrochemistry*

- LSCF-GDC 70-30 wt.% mixture was found to have the lowest ASR among the LSCF-GDC composites. These findings are supported by the "percolation theory" identified in the literature.
- BSCF demonstrates ~7x reduction in ASR vs. LSCF (0.4 $\Omega cm^2$ vs. 2.95 $\Omega cm^2$ at 600°C), suggesting that BSCF is a strong candidate for use in low temperature SOFC.
- A model was developed to relate the processes observed on the impedance spectra to physical processes occurring in the BSCF cathode.

- The overall reaction mechanism for BSCF and LSCF consists of three different processes occurring in series: charge transfer of oxygen ions at the cathode/electrolyte interface, surface exchange of oxygen, and gas diffusion.
- BSCF undergoes a transition at 600°C in its dominant mechanism. Below 600°C, the gaseous oxygen undergoes partial reduction and surface diffusion. Above 600°C, the oxygen undergoes complete oxygen reduction and incorporation into vacancies in the lattice, followed bulk diffusion to the cathode-electrolyte interface.

# References


1. Williams, M.C. et al. *Solid State Ionics* 177 (2006) 2039-2044
2. Adler, S.B.; Chen, X.Y., Wilson, J.R. *Journal of Catalysis* 245 (2007) 91-109
3. De Souza, R.A., Kilner, J.A. *Solid State Ionics* 106 (1998) 175-187
4. De Souza, R.A., Kilner, J.A. *Solid State Ionics* 106 (1998) 175-187
5. Benson, Chater, Kilner *Proceedings of the Third International Symposium on Ionic and Mixed Conducting Ceramics* Vol 97-24 (1997) 596-607
6. De Souza, R.A. Kilner, J.A. *Solid State Ionics* 106 (1998) 175-187
7. Benson, Chater, Kilner, Proceedings of the Third International Symposium on Ionic and Mixed Conducting Ceramics Vol 97-24 (1997) 596-607
8. Cheetham, A.K., Day, P. Solid State Chemistry: Techniques, Clarendon Press, Oxford (1987)
9. De Souza, R.A. Kilner, J.A. *Solid State Ionics* 106 (1998) 175-187
10. Benson, Chater, Kilner, Proceedings of the Third International Symposium on Ionic and Mixed Conducting Ceramics Vol 97-24 (1997) 596-607
11. Adler, S. B.; Lane, J. A.; Steele, B. C. H. *J. Electrochem. Soc.*143 (1996) 3554
12. Adler, S. B.; Lane, J. A.; Steele, B. C. H. *J. Electrochem. Soc.* (1996), *143*, 3554
13. Adams, J.W., Nakamura, H.H., Ingel, R.P., Rice, R.W. *J. American Ceramic Society* 68 (1985) C-228
14. Kharton, V.V., Figueiredo, F.M., Navarro, L. et al. *J Materials Science* 36 (2001) 1105-1117
15. Singh, P., Minh, N.Q., *Int. J. Applied Ceramic Technology* 1 (2004) 5-15
16. V.M. Goldschmidt, Skr. Nor. Videnk-Akad., Kl. 1: Mat.-Naturvidensk. Kl. No. 8 (1926)
17. Khattak, C.P., Wang, F.F.Y. in: Gschneider, K.A., Eyring, L. (Eds.), Handbook of the Physics and Chemistry of Rare Earths, North-Holland Publisher, Amsterdam (1979) p. 525.
18. Goodenough, J.B., Longo, J.M. in: Hellwege, K.H., Helwege A.M. (Eds.), Landolt-Bronstein New Series, vol. 4, part A, Springer-Verlag, Berlin (1970) p. 126
19. Goodenough, J.B. in: Rao, C.N.R. (Ed.), Solid State Chemistry, Marcel Dekker, New York (1974) p. 215
20. Voorhoeve, R.J.H. et al. *Science* 195 (1977) 827-833
21. N.Q. Minh, Ceramic fuel cells, *J. Am. Ceram. Soc.* 76 (1993), pp. 563–588
22. Button, D.D., Archer, D.H. American Ceramic Society, Washington, Meeting (1966)
23. Tedmon, C.S., Spacil, H.S., Mitoff, S.P. *J. Electrochem Soc* 116 (1969) 1170-1175
24. Van Doorn, R.H.E., Burggraaf, A.J. *Solid State Ionics* 128 (2000) 65-78
25. Petrov, A.N. et al. *Solid State Ionics* 80 (1995) 189-199
26. Raccah, P.M., Goodenough, J.B. *J. Applied Physics* 39 (1968) 1209
27. Raccah, P.M., Goodenough, J.B. *Physics Review* 155 (1967) 932
28. Maric, R. et al. *J. Electrochem Soc* 146 (1999) 2006-2010
29. Misuzaki, J., Mima, Y., Yamauchi, S., Fueki, K. *J. Solid State Chemistry* 80 (1989) 102-111
30. Petrov, A.N. et al. *Solid State Ionics* 80 (1995) 189-199

31. Minh, N.Q., Takahashi, T. *Science and Technology of Ceramic Fuel Cells* Elsevier Science, Amsterdam, The Netherlands (1995)
32. Mizusaki, J., Tabuchi, J., Matsuura, T., Yamauchi, S., Fueki, K. *J. Electrochemical Society* 136 (1989) 2082-2088
33. Goodenough, J.B. *Mater. Res. Bull.* 6 (1971) 967
34. Senaris-Rodriguez, M.A., Goodenough, J.B. *J Solid State Chemistry* 118 (1995) 323-336
35. Teraoka, Y., Zhang, H.M., Okamoto, K., Yamazoe, N. *Materials Research Bulletin* 23 (1998) 51-57
36. Ullman, H. et al. *Solid State Ionics* 138 (2000) 79-90
37. Adler, S.B. *Solid State Ionics* 111 (1998) 125-134
38. Adler, S.B. *Solid State Ionics* 111 (1998) 125-134
39. Wang, S., Verma, A., Yang, Y.L., Jacobson, A.J., Abeles, B. *Solid State Ionics* 140 (2001) 125-133
40. De Souza, R.A., Kilner, J.A. *Solid State Ionics* 106 (1998) 175
41. Wang, S., Verma, A., Yang, Y.L., Jacobson, A.J., Abeles, B. *Solid State Ionics* 140 (2001) 125-133
42. Yokokawa, H., Sakai, N., Kawada, T., Dokiya, M. in *Proceedings of the Second International Symposium on Solid Oxide Fuel Cells, Athens, Greece, July 1991*, Grosz, F., Zegers, P. Singhal, S.C., Yamamoto, O. (eds.), Commission of the European Communities, Luxembourg (1991) p.663
43. Yokokawa, H., Sakai, N., Kawada, T., Dokiya, M. in *Science and Technology of Zirconia V,* Badwal, S.P.S., Bannister, M.J., Hannink (eds.), Technomic Publishing Company, Lancaster, PA, (1993)
44. Adams, J.W., Nakamura, H.H., Ingel, R.P., Rice, R.W. *J. American Ceramic Society* 68 (1985) C-228
45. Kharton, V.V., Figueiredo, F.M., Navarro, L. et al. *J Materials Science* 36 (2001) 1105-1117
46. Ullman, H. et al. *Solid State Ionics* 138 (2000) 79-90
47. Simner, S.P., Shelton, J.P., Anderson, M.D., Stevenson, J.W. *Solid State Ionics* 161 (2003) 11-18
48. Dann, S.E., Currie, D.B., Weller, M.T., Thomas, M.F., Al-Rawwas, A.D. *J Solid State Chemistry* 109 (1994) 134-144
49. Waernhus, I., Vullum, P.E., Holmestad, R., Grande, T., Wiik, K. *Solid State Ionics* 176 (2005) 2783-2790
50. Bucher, E., Sitte, W. *J. Electroceramics* 13 (2004) 779-784
51. Mizusaki, J., Yoshihiro, M., Yamauchi, S., Fukei, K. *J Solid State Chemistry* 58 (1985) 257-266
52. Patrakeev, M.V. et al. *J Solid State Chemistry* 178 (2005) 921-927
53. Patrakeev, M.V. et al. *J Solid State Chemistry* 172 (2003) 219-231
54. Adler, S.B. *Chemical Reviews* 104 (2004) 4791-4843
55. Ullman, H. et al. *Solid State Ionics* 138 (2000) 79-90
56. Yoo, J., Verma, A., Wang, S., Jacobson, A.J. *J. ECS* 152 (2005)
57. Yoo, J., Verma, A., Wang, S., Jacobson, A.J. *J. ECS* 152 (2005)

58. Fossdal, A., Menon, M., Waernhus, I., Wiik, K., Einarsrud, M.A., Grande, T. *J American Ceramic Society* 87 (2004) 1952-1958
59. Simner, S.P., Shelton, J.P., Anderson, M.D., Stevenson, J.W. *Solid State Ionics* 161 (2003) 11-18
60. Dusastre, V., Kilner, J.A. *Solid State Ionics* 126 (1999) 163-174
61. Perry Murray, E., Sever, M.J., Barnett, S.A. *Solid State Ionics* 148 (2002) 27-34
62. Leng, Y., Chan, S.H., Liu, Q. *International Journal of Hydrogen Energy* 33 (2008) 3808-3817
63. Steele, B.C.H. *Solid State Ionics* 86-88 (1996) 1223-1234
64. Teraoka, Y., Zhang, H.M.,Furukawa, S.,Yamazoe, N. *Chemistry Letters* 14 (1985) 1743
65. Qui, L., Lee, T.H., Liu, L.M., Yang, Y.L, Jacobson, A.J. *Solid State Ionics* 76 (1995) 321
66. Pei, S. et al. Catal. Lett. 30 (1995) 201
67. Kruidhof, H., Bouwmeester, H.J.M., Van Doorn, R.H.E., Burggraaf, A.J. *Solid State Ionics* 63-65 (1993) 816
68. Shao, Z.P., Xiong, G.X., Tong, J.H., Dong, H., Yang, W.S. *Sep. Purif. Tech*. 25 (2001) 419
69. Shao, Z.P., Yang, W.S., Cong, Y., Dong, H., Tong, J.H., Xiong, G.X. *J. Membr. Sci*. 172 (2000) 177
70. Shao, Z.P., Xiong, G.X., Dong, H., Yang, W.S., Lin, L.W. *Sep. Purif. Tech*. 25 (2001) 97
71. Shao, Z.P., Dong, H., Xiong, G.X., Cong, Y., Yang, W.S. *J. Membr. Sci*. 183 (2001) 181
72. Shao, Z.P., Haile, S.M., Nature 431 (2004) 170
73. Zhou, W., Ran, R., Shao, Z.P. *J Power Sources* 192 (2009) 231-246
74. McIntosh, S. et al. *Solid State Ionics* 177 (2006) 1737-1742
75. Chen, Z., Ran, R., Zhou, W., Shao, Z.P., Liu, S. *Electrochimica Acta* 52 (2007) 7343-7351
76. McIntosh, S. et al. *Chem Mater* 18 (2006) 2187-2193
77. Chen, Z., Ran, R., Zhou, W., Shao, Z.P., Liu, S. *Electrochimica Acta* 52 (2007) 7343-7351
78. Bucher, E. et al. *Solid State Ionics* 179 (2008) 1032-1035
79. Bucher, E. et al. *Solid State Ionics* 179 (2008) 1032-1035
80. Bucher, E. et al. *Solid State Ionics* 179 (2008) 1032-1035
81. McIntosh, S. et al. *Chem Mater* 18 (2006) 2187-2193
82. Zhou, W. et al. *J Power Sources* 182 (2008) 24-31
83. Wei, B et al. *J European Ceramic Society* 26 (2006) 2827-2832
84. Lim, Y.H. et al. *J Power Sources* 171 (2007) 79-85
85. Wei, B. *Electrochem. Lett.* 8 (2005) A428-A431
86. Arnold, M., Wang, H., Feldhoff, A. *J Membrane Science* 293 (2007) 44-51
87. Yan, A. et al. *Applied Catalysis B: Environmental* 76 (2007) 320-327
88. Yan, A. et al. *Applied Catalysis B: Environmental* 66 (2006) 64-71
89. Yan, A. et al. *J Power Sources* 185 (2008) 76-84
90. Ge, L. et al. *J Membrane Science* 306 (2007) 318-328

91. Jensen, et al. J Electrochem Soc *154* (2007) B1325-B1330
92.. Takeda, Y. et al. *ECS* 134 (1987) 2656
93. Chick, L.A., et al., *Materials Letters* 10 (1990) 6-12
94. Ried et al. *J. Electrochem Soc.* 155 (2008) B1029-B1035
95. Dusastre, V., Kilner, J.A. *Solid State Ionics* 126 (1999) 163-174
96. Kharton, V.V. et al. *J. Material Science* 36 (2001) 1105-1117
97. Ullman, H. et al. *Solid State Ionics* 138 (2000) 79-90
98. Fu, C.Y. et al. *Matierals Chemistry and Physics* 91 (2005) 28-35
99. International Center for Diffraction Data; card 00-055-0563 (retrieved Dec. 2009)
100. McIntosh, S. et al. *Chem. Mater.* 18 (2006) 2187-2193
101. Li, S. et al. *Solid State Ionics* 178 (2007) 417-422
102. Tai, L.W. et al. *Solid State Ionics* 76 (1995) 273-283